ABSTRACT

Title of Document: THERMAL AND THERMOMECHANICAL BEHAVIOR OF MULTI-MATERIAL MOLDED MODULES WITH EMBEDDED ELECTRONIC COMPONENTS FOR BIOLOGICALLY-INSPIRED AND MULTI-FUNCTIONAL STRUCTURES

Lawrence S. Gyger, Jr.
Master of Science, 2006

Directed By: Associate Professor Hugh Bruck
Department of Mechanical Engineering

Recently, there has been considerable interest in creating biologically-inspired structures, such as robots, and multi-functional structures, such as morphing aircraft fins, for use in environments that are considered hazardous for electronic systems. Cases in point are serpentine robots for use in search and rescue reconnaissance missions, and morphing chevrons for jet engines. These biologically-inspired and multi-functional structures require embedding sensitive electronic components in order to provide multi-functionality, such as actuation and sensing, while providing the thermal and mechanical protection these components need during operation in extreme environments. To this end, a multi-stage molding process has been implemented to affordably mass-produce multi-material modules with embedded electronic components for biologically-inspired and multi-functional structures.

However, in designing and manufacturing modules using this process, it is necessary to consider two issues: (a) the heat generated during operation the electronic components can be appropriately managed to prevent thermal failure of the components, and (b) the thermomechanical response of the module to the multi-material molding process and the operation of the embedded electronic components will not lead to mechanical failure of the module. To gain insight into the thermal and thermomechanical behavior of these modules, experiments were designed and conducted to determine three critical design characteristics of the modules: (a) *the steady-state thermal conductivity across the multi-material interface in a module*, (b) *the transient thermal response at the core of the multi-material module at elevated temperatures*, and (c) *the thermomechanical strains that develop around the embedded electronic components in the multi-material module during in-mold processing and operation of the components*. Based on these experiments, analytical and numerical models are developed for predicting the thermal and thermomechanical behavior of multi-material modules with embedded components that provide a foundation for designing these modules for biologically-inspired and multi-functional structures. A prototype serpentine robot designed with multi-functional modular structures is presented, and complementary thermal and mechanical testing of a new prototype multi-material module with an embedded component for this biologically-inspired structure designed for thermal and impact resistance is also presented.

THERMAL AND THERMOMECHANICAL BEHAVIOR OF MULTI-MATERIAL MOLDED MODULES WITH EMBEDDED ELECTRONIC COMPONENTS FOR BIOLOGICALLY-INSPIRED AND MULTI-FUNCTIONAL STRUCTURES

By

Lawrence S. Gyger, Jr.

Thesis submitted to the Faculty of the Graduate School of the
University of Maryland, College Park, in partial fulfillment
of the requirements for the degree of
Master of Science
2006

Advisory Committee:
Associate Professor Hugh Bruck, Chair
Associate Professor Satyandra Gupta
Professor Abhijit Dasgupta

Dedication

This thesis is dedicated to Drena, the most special person in my life. When I left the university as a sophomore in 1998, she was the only one who believed that I would return. When I did return in 2001, she provided me with the motivation to constantly do my best work throughout the rest of my undergraduate education. Only because of her tenacious patience and selflessness was I able to continue my education and pursue a Master's degree. I owe all of my achievements to her. I am forever grateful and hope that one day she makes a good return on her investment.

Table of Contents

List of Tables

List of Figures

Chapter 1: Introduction

1.1 Motivation for Biological Inspiration and Multi-Functionality

Nature has a way of creating materials and organizing them into structures that are of interest to many areas of academic research extending beyond biology and including other sciences such as chemistry, physics, and engineering. These materials and structures have been optimized over millions of years resulting in objects that have combinations of properties and functionality that are not yet reproducible by modern methods. It is very desirable to model things after nature since natural objects can be found in the harshest of climates and most adverse environments. Using concepts found in nature, new designs can be developed leading to products that have applications in environments once thought to be impossible.

From an engineering perspective, a natural object such as a tree, a cat, or a bird can be viewed as an engineered product that can basically be broken down into two broad categories: *structure* and *material*, both of which are essential to each other. The materials govern the characteristics such as how heavy it is or how susceptible to injury it may be. The term structure applies to the macroscopic organization of parts which comprise subsystems or complete systems and controls how the materials interact with one another which may ultimately affect agility, speed, or even life expectancy.

1.1.1 Biologically-Inspired and Multi-Functional Structures

The assembly of the parts that make up the subsystems and the collection of subsystems that comprise the entire natural object are an area of interest for many reasons. Some natural objects are large and other objects are small, but the size of the structure of a particular animal does not necessarily have an influence on its speed. The smallest animal is not the fastest or slowest, and neither is the largest animal. The fastest mammal is the cheetah, whose size is somewhere in the middle. Having the right combination of skeletal structure and muscle structure are the largest contributors to the speed of an animal. Another example of how nature optimizes structures for particular applications is the ant. The average ant has such an optimized structure that it is able to carry up to five times its body weight, and it has been claimed that there is a species that can carry over twenty times its own weight. These structural subtleties found in nature can lead to new designs that are much more efficient, lightweight, or responsive than traditional designs. They can also lead to structures that are "multi-functional", i.e. capable of performing many functions such as harvesting energy from the environment, supporting mechanical and thermal loads from the environment, transporting fluids, etc. For example, the trunk of a tree is designed to transport nutrients in solution throughout a tree while concurrently serving as the mechanical support for distributing mass during the growth of the tree that increases the surface area of the tree both vertically and horizontally needed for gathering solar energy used in the chemical process known as photosynthesis to drive the production of new organic matter required for the growth.

1.1.2 Biologically-Inspired and Multi-Functional Materials

Researchers are extremely interested in understanding natural materials in order to take advantage of the natural selection process in optimizing the performance of synthetic materials and their geometries. The use of the term “geometry” differs from the term “structure” in the way that it is on a smaller scale and only includes how the materials make up a particular part of an object, whereas the structure implies how the parts are organized into systems or subsystems. Most natural materials are characterized by their hierarchical arrangement in which there are levels of architectural organization controlled on many different length scales including molecular, nanoscopic, microscopic, and macroscopic. The material combinations can be quite complex, some extremely difficult to characterize. The particular geometry in which the levels are arranged is also of prime significance to the performance of the material and the part it constitutes. The optimum combination of constituent materials in conjunction with the geometry enables the materials to perform more than one function at a time. One example of this multi-functionalism can be found in natural bone. In a relative sense, bone is hard, primarily made up of collagen and calcium phosphate. However, bones contain pores that allow for ductility in addition to aiding in fluid flow, while reducing the overall mass. Using ideas from nature, new biologically-inspired and multi-functional materials can be designed for optimum performance in a variety of applications. Because of the complex microstructure of biological-inspired and multi-functional materials, it can be difficult to differentiate a material system from a structural system, and in some cases the two terms will be used interchangeably.

1.2 Background

1.2.1 Serpentine Robots

In recent years, the robotics community has shown considerable interest in biologically-inspired design leading toward the use of robotic structures in applications that were once thought too harsh for electronic systems. One application of particular interest is for search and rescue reconnaissance missions. Most of the robots produced up until now are much too large to fit in tight spaces and they are not able to traverse the rough, unsteady terrain that may be encountered on such missions. However, it has been realized that there are creatures in nature that are extremely versatile and are able to handle a variety of terrains as well as fit into tight quarters, such as snakes. Snakes are able to travel on many types of terrain including sand and loose rocks, they can climb trees, and some of them can even swim.

Since this realization, robotics engineers have given much attention to the serpentine configuration. The mobility and adaptability of this type of configuration give serpentine robots advantages over wheeled and legged robots. In addition, because of the modular nature of many of the current serpentine robot designs, they are more robust to mechanical failure; if one module becomes damaged, it is still possible to for the remaining modules to remain functional. However, when placed in extreme conditions such as those for search and rescue reconnaissance missions, even modularity cannot keep the robots from failing because of the susceptibility of the electronic components to the environment.

Many current designs of serpentine robots consist of metal frames that support the motors, circuit boards, and other electronic components that are open to the outside environment. There are numerous reasons why this is unacceptable. Fires are one of the extreme environments that the robot is to be used. These scenarios may involve falling debris, high temperatures, and even water from sprinklers or fire hoses. If the fragile electronic components are at all exposed to any of these conditions, they will certainly be destroyed. The high conductivity of the metal frames, usually aluminum, allows the heat to travel quickly through the frame and melt or burn up the electronic components. In addition, mass is a primary concern for robot efficiency and metal frames are not the optimal choice when the magnitude of the average mechanical load is considered. With these factors in mind, it is clear that the there is a need to design serpentine robots for better electronics protection in addition to using more suitable materials for supporting the structure that keep mass to a minimum while sustaining the necessary mechanical strength.

1.2.2 Multi-Material Molding

Just as the overall structure of this breed of robots is biologically-inspired, it is thought that the material system that makes up the structure also be biologically-inspired, taking advantage of the multi-functional aspects of material systems found in nature. The material system should be able to protect electronic components from extreme temperatures, in addition to protecting them from impact, while providing structure for the robot modules and remaining as lightweight as possible. The structure itself could also provide the necessary friction to aid in mobility.

A multi-material, often called heterogeneous, polymer system is recommended for this application because of the low density, low thermal conductivity, and high impact strength achievable. By combining the properties of different materials into a multi-material composite, it is possible to obtain performance levels that could otherwise not be attained using homogenous materials.

The benefits of a multi-material system can be augmented by selecting a manufacturing process that allows for much freedom in the geometries that can be produced, such as a multi-stage molding (MSM) process. By using MSM technology, which encompasses processes such as multi-material molding (MMM), and more specifically multi-material injection molding (MMIM), the temperature sensitive electronic components can be embedded in the multi-material polymer system, which not only allows for complex geometries to be produced, but also allows for all assembly to take place in mold without secondary operations. Using this type of technology, affordable, mass producible, multi-functional structures become much more of a reality.

1.3 Research Issues

In order to design an appropriate multi-material system with embedded electronic components for serpentine robots, as well as other biologically-inspired and multi-functional structures with embedded low power electronic components, it must be known how the processing of the multi-material system affects the thermal and thermomechanical behavior of the structure to predict how the structure will perform. Since MMM is a relatively new technology, there is no published data on the effects of this process on thermal and thermomechanical properties and the performance of the system. This information is crucial in designs utilizing embedded electronic components because of the intrinsic thermal loads caused by the electronic components, as well as for structures whose main application may involve external thermal loads. Some materials used in a multi-material system may display good chemical bonding because of similar molecular arrangement, leading to a mixture of materials at the interface. This interface may have an effect on the overall ability of the multi-material system to conduct heat, as is the case in other types of interfaces when subjected to thermal loading. Alternatively, the thermal performance of a multi-material system with constituent materials that show poor bonding may also be affected by the MMM process.

1.4 Objective

The objective of this research is to characterize the effects of the MMM process on the thermal and thermomechanical behavior of multi-material systems and to develop appropriate models for designing biologically-inspired and multi-functional structures with embedded electronic components fabricated by MMM processes.

1.4.1 Scope of Research

The research is focused on characterization and development of thermal and thermomechanical models applicable to multi-material modules with embedded electronic components for use in rugged applications, specifically serpentine robots. Chapter 2 discusses the current state of the art of the four main aspects of this research: serpentine robots, MMM, embedded electronics, and multi-functional structures with electronic components. Characterization of the steady-state thermal conductivity of MMIM interfaces is discussed in Chapter 3. The results of the characterization effort are then used to develop an applicable rule of mixtures model for multi-material polymer systems taking into consideration the effects of adhesion on the overall conductivity. Also included in Chapter 3 is a characterization of the transient thermal response of spherical homogeneous and heterogeneous modules that is further developed by a rigorous modeling effort that includes homogenized analytical models, a fitting formula, and finite element models, all applicable to different situations depending upon the available data.

In Chapter 4 the thermomechanical behavior of multi-material systems is analyzed. The thermomechanical discussion is broken up into four main parts. The first part discusses the characterization of the thermomechanical behavior of MMIM systems during processing both with and without embedded electronic components by investigating the shrinkage during in-mold cooling. The second section of the chapter discusses a thermomechanical finite element model that has been developed to predict the displacement fields that evolve in multi-material modules with embedded electronic components during processing. Then the analysis turns to the operational stage of the life cycle of homogeneous and heterogeneous structures, focusing on the thermomechanical effects caused by the internal heat generation of the electronic components during use. The final section discusses a two-part thermomechanical finite element model capable of reproducing the thermomechanical displacement fields observed by during the internal heat generation experiments.

Chapter 5 serves as a proof of concept chapter for the thesis. There are two main parts of the chapter, which are further divided into smaller sections. The first main part discusses the design and development of a prototype serpentine robot fabricated by MMM. The second part of the chapter discusses the fabrication of a prototype MMIM module with embedded low power electronics. The robustness of such structures is presented by performing three loading experiments, thermal, compressive, and impact. This chapter serves as a solid foundation for showing the ruggedness of possible future designs of biologically-inspired robots with embedded electronic components fabricated by MMIM processes.

1.4.2 Contributions of Research

The contributions of this research provide a basis for designing heterogeneous polymer structures for use in rugged applications, especially those involving thermal loading. The steady-state thermal conductivity characterization results in a correction term applicable to the standard rule of mixtures model that can account for the increased thermal resistance of the interface in multi-material structures, allowing engineers to be able to tailor thermal conductivity based on the adhesion of the material system. Three different models are presented regarding the transient thermal response of multi-material systems, all of which are useful in a different regard. It is shown that the thermal response of a heterogeneous structure subjected to a sudden increase in ambient temperature can be accurately predicted by a homogenized form of the analytical solution, where all that is needed are the appropriate material parameters. Another contribution is a formula in the form of a general exponential equation which provides excellent correlation with experimental results for multi-material spherical structures below the melting temperature. A finite element model is also developed to predict the response of multi-material systems subjected to convective boundary conditions. The important part of this contribution is the ability for the model to correlate extremely well with experimental results while still having the unique ability of accounting for changes in phase of the multi-material system at ambient temperatures above the melting temperature.

In addition, another contribution is made by modeling the thermomechanical response of multi-material modules and the shrinkage of the polymers in-mold while cooling. The thermomechanical finite element model is validated by characterizing the thermomechanical behavior of multi-material modules by analyzing the resulting displacement and strain fields using in-situ experimental methods. The effect of internal heat generating electronics is also characterized and an appropriate thermomechanical finite element model developed so that designers can predict the performance of embedded electronics in homogeneous and heterogeneous structures. The final contributions are in the form of a prototype serpentine robot that was fabricated using MMM to demonstrate the ability to produce modular, scalable, autonomous robots at an affordable cost in addition to a prototype MMIM structure with fully embedded electronic components to validate the survivability of such structures in harsh environments.

Chapter 2: Related Work

The work presented in this thesis encompasses several broad research categories, each of which requires a discussion apart from the others. In this regard, the discussions are not exhaustive and comprehensive of all aspects of each of the topics, but only seek to define the work that has been completed that pertains to the research in this thesis.

2.1 Serpentine Robots

Of the three topics, the design and analysis of serpentine robots has been the most widely investigated. One of the first serpentine robots was developed by Hirose and is discussed in [Hiro93]. The main purpose of its development was to aid in understanding how real snakes move. It is powered and controlled by external sources, making use of a serpentine gait and wheels on an aluminum frame to move in the horizontal plane. Hirose continued to build off the first design and developed other serpentine robots that were remote controlled with on-board power supply, including a modular design that is capable of moving in both the horizontal and vertical plane [Mori01] as well as a waterproof version that does not yet have published details.

The first case of a serpentine robot without wheels was presented by Dowling [Dowl97], making use of an aluminum frame with a fabric covering to provide the required friction to propel the robot forward using the serpentine gait. The servo motors were controlled using a centralized control and a bus that ran the length of the robot, and power was supplied externally. Since the development of the Hirose and Dowling robots, many other serpentine robots have been developed such as in [Wors96, Nils98, Ma01, Taki01, Gran05, Tane05]; however, the bulk of the research is focused on gait design and analysis as well as novel control architectures for path planning, which are out of the scope of this thesis.

One recent serpentine robot design that has some significance with the research discussed in this thesis has been presented in [Cresp05], as it pertains to a robot that makes use of molding technology. The goals of the work were to have a waterproof robot that has a modular architecture, a central pattern generator for developing the appropriate control signals, and the ability to be controlled remotely, in addition to the buoyancy, friction, and actuation requirements necessary to produce motion both in and out of water. However, as presented, the robot used wheels to provide the appropriate friction on land, and had not been tested in the water. In addition it should be noted that although a molding process was used to fabricate the parts, only the batteries were actually embedded in the polymer. Assembly operations on all of the remaining parts were required, and the waterproofing characteristic was to be achieved using rubber seals between the parts.

2.2 Multi-Stage, Multi-Material Molding

Several molding techniques exist that enable the manufacture of multi-material objects, such as multi-component molding, multi-shot molding, and overmolding. Multi-component molding, also known as sandwich or co-injection molding, involves sequential injection of different materials, allowing one material to encapsulate another using the same mold cavity and two or more injection locations in the mold. Multi-shot molding also consists of sequential injection of different materials but uses a multi-cavity mold and some sort of rotating mold, rotating tool, sliding core, or other motion to switch between the different material injection points. Overmolding uses different materials and different molds for each material, one part is made and then inserted into another mold and a different material is injected to form a multi-material object. Each of these processes is reviewed in detail in [Good02]. Both multi-shot molding and overmolding fall under the category of MSM, which encompasses thermoset processing techniques such as room temperature casting in addition to thermoplastic injection molding.

Presently, there is very limited literature in the area of MMM other than the research that has been conducted at the University of Maryland (UMD). UMD’s work involves the automated design of multi-stage molds, such as in [Kuma02, Li04a, Li04b], and manufacturing analyses for MMM objects [Li03]. There have been even fewer works in the characterization and analysis of objects fabricated by MMM processes. One investigation has shown that introducing geometric complexity into the design of multi-material structures can lead to enhanced interfacial strength

[Bruc04], however there have been no investigations into the effect of the MSM process on the thermal performance of the heterogeneous structures that are produced.

Prediction of shrinkage is a very important step in ensuring defect free molded products. This problem is an active area of research and continues to receive attention from the research community. Computational and experimental investigations have been performed to develop models to predict shrinkage as a function of processing conditions. Existing efforts have explored how injection pressure, packing pressure, holding pressure, melt temperature, and mold temperature affect the shrinkage [Bush96, Jans96, Jans98, Pont04, Liao04, Kram05]. Different thermoplastic materials exhibit different shrinkage characteristics. Models also have been developed that describe how material properties, such as crystallinity and viscosity affect shrinkage [Han97]. Shrinkage has been found to be highly anisotropic and shrinkage in the thickness direction is found to be significantly different than the flow direction [Tito96, Kwon05, Dela00]. Recent investigations have explored how the mold deformation affects the shrinkage [Dela00]. It has been realized that higher packing pressures lead to mold deflections which significantly lower the observed values of shrinkage. Products with different geometries exhibit different shrinkage characteristics due to different constraints imposed by the mold pieces on the shrinking parts. Investigations have been conducted to explore how certain classes of highly specialized geometric shapes shrink during the injection molding cycle [Liao04].

MSM involves the presence of prefabricated components inside the mold. In many situations prefabricated components are plastic pieces that have been molded in an earlier stage. When the solid plastic piece present inside the mold is subjected to the injection pressure it undergoes deformation. This deformation is orders of magnitude greater than the deformation experienced by tool steel mold pieces. In addition, many operations perform subsequent stages while the first stage is still cooling to promote adhesion. Such deformation of pre-molded or just processed components is expected to change shrinkage characteristics significantly. However, existing shrinkage prediction models do not account for presence of highly deformable mold pieces in shrinkage prediction models. Nor do the current models account for the embedding of electronic components which is discussed in more detail in the following section.

2.3 Embedded Electronic Components

Embedding of electronics has become a topic under consideration for many different applications such as under-the-hood automotive modules, portable electronic devices (e.g., MP3 players, PDAs), and laptop computers. Credit for developing many objects containing embedded electronics goes to Carnegie Mellon University (CMU), including the first case of embedded electronics which was a handheld game [Beck92]. Throughout the 1990's and into the early part of the 21st century, CMU has developed several generations of wearable computers. These wearable computers are intended for military applications requiring storage of digital navigational maps, vehicle maintenance instructions and manuals, and field operational instructions. The first instance of embedded electronics in the wearable computers was in the VuMan-

SDM reported in [Weis97]. The VuMan-SDM, along with later generations of the VuMan wearable computer such as the VuMan3R [Egan96, Egan00] shown in Figure 1, and the Frogman, a waterproof version of the VuMan designed for the Navy [Cham99], all make use of a technology known as shape deposition manufacturing (SDM) to embed the electronic components.

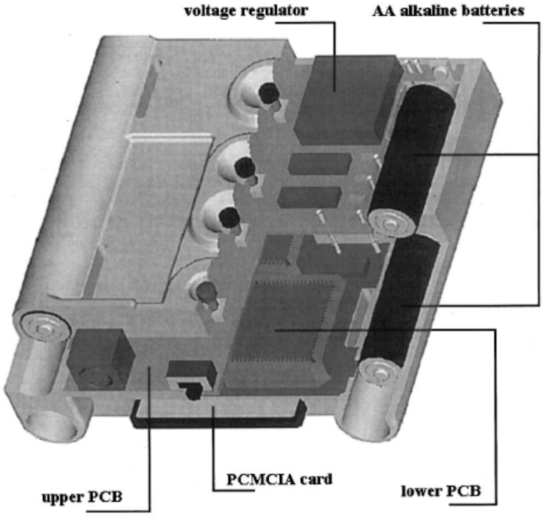

Figure 1 - Carnegie Mellon University's VuMan3R wearable computer [Egan96, Egan00]

SDM is a process that produces three-dimensional shapes by a combination of additive layering steps and material removal using a computer numerically controlled milling machine. As reported by [Weis97], the VuMan-SDM was fabricated using three layers of a polyurethane resin, with each layer taking over an hour for curing and machining. After machining the first layer, a printed circuit board was placed on top of the structure and then another layer was deposited. A similar process was completed after machining the second layer.

Around the same time that CMU was embedding circuit boards in polyurethane resin for wearable computers using SDM, Stanford University was fabricating biologically-inspired robots with embedded components using SDM [Cham99]. A whole family of biologically-inspired robots containing embedded electronic components have been produced at Stanford, from large to small, all using the same platform as the original cockroach-inspired robot reported by [Cham99], but their focus is not on embedded electronics as much as it is on embedded pneumatic actuators and the SDM process itself.

One of the problems that arise from embedding electronic components is conducting away the heat that all electronic components generate during sustained operation. If the materials in which the electronic components are embedded are low thermal conductivity polymers, the associated rise in temperature can lead to component failure due to thermal stress and accelerated aging. Thus, most of the focus for later versions of the VuMan wearable computer design has been on developing, characterizing, and modeling thermal management solutions. Using an active cooling method is not much of an option due to the additional power consumption of the cooling system. The use of a large surface area heat spreader in contact with the main heat generating elements on the inside as well as the ambient air on the outside has been shown by numerical simulations to be one effective way of handling the thermal issues of embedded electronics for the wearable computers [Egan96, Egan00].

CMU’s wearable computers and Stanford’s hexapedal robots both make use of a thermosetting casting resin to embed the electronic and non-electronic components; however other processes such as injection molding, which makes use of thermoplastic polymers, have been investigated. [Teh00a, Teh00b] tested five different polymers and conducted a detailed analysis of the failure mechanisms of embedded electronics using a single material injection molding process. Process parameters such as base material, filler, melt and mold temperatures, injection and holding pressures, part and printed circuit board thickness, and injection location were all compared using a Design of Experiments approach. Failure was considered to be by one of three mechanisms, solder defect, printed circuit board deflection, or entire module deflection. Appropriate analysis techniques, such as X-ray radiographs and cross-sectioning, were used. The results of the statistical analysis showed that best result is achieved for the conditions of low melt temperature, high mold temperature, and low injection pressure [Teh00a, Teh00b].

Aside from the solder defect failure mechanism, which was speculated to be caused by thermal shock, the deflection failure mechanisms were thought to be caused by polymer shrinkage and mismatch of thermal expansion coefficients between the circuit board and the polymer.

Thermal issues involved with embedding electronics have been investigated by [Sarv04]. Three finite element models, a one-dimensional, a two-dimensional, and a three dimensional model, were developed to determine the steady-state temperature profile for a ceramic resistor on an FR-4 substrate fully embedded in a rectangular geometry comprised of polybutylene terephthalate for given power inputs and ambient boundary conditions. The results of the models indicated that the three-dimensional model reached the highest temperature at the top of the resistor, followed by the two-dimensional model, and the one-dimensional model had the lowest steady state temperature. The three-dimensional model predicted a temperature increase of approximately 130ºC for a resistor dissipating 1 Watt of power. A transient finite element simulation was also run to determine the effect of three resistors on a circuit board with and without the polymer encapsulation. The transient test results indicated that the polymer initially had a lower temperature at the top of the center resistor, but eventually resulted in a higher steady-temperature as expected. A thermomechanical model was also developed using the temperature results from the transient simulation, and the maximum displacement was reported to be no more than 13 micrometers, however the specific details were not reported. An experiment was devised to validate the steady-state results, the final results are shown in Figure 2 [Sarv04].

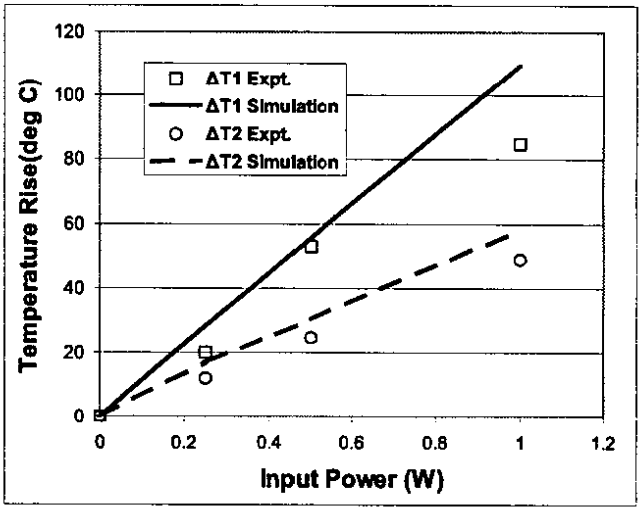

Figure 2 - Results of [Sarv04] experiments and models

To address the thermal issues that are inherent in embedding electronics in low conductivity polymers there have been investigations into adding filler particles to increase the overall thermal conductivity. Nylon filled with carbon black, synthetic graphite, and carbon fiber has been shown to have a positive effect on the thermal conductivity of injection molded parts [Heis04]. However, caution must be exercised that the polymer is not electrically conductive near the electronic components or a short may result.

The work concerning embedded electronics is still in its beginning stages. CMU and Stanford have made contributions to this area by showing that it is possible to use the SDM process to embed electronic components in polymers, while [Teh00a, Teh00b] have contributed insight as to which conditions work well for using injection molding as the embedding process. The work by [Sarv04] is the only report of thermal and thermomechanical models for predicting the response of heat dissipating embedded electronics, and the only experiment that was run to validate the models was a single steady-state experiment that resulted in as much as 20 percent discrepancy from the model, using only a single layer of polymer material.

2.4 Multi-Functional Structures with Electronic Components

There are many current approaches to developing multi-functional structures with electronic components in applications such as aerospace vehicles [NRC04]. Most of these concepts employ conventional sensors, such as strain sensors, thermal sensors, and optical sensors as independent components in the structures. More advanced sensing concepts involve the embedding of materials, such as distributed optical fibers with integrated Bragg gratings that can interact with the structure to detect strains and temperatures for health monitoring in “Smart Structures” [Udd95]. More advanced actuation concepts have also been developed using similar concepts where active materials, such as Shape Memory Alloys (SMAs), piezoelectric materials, and electroactive polymers, interact with the structure in which they are embedded. Each of these concepts has limitations on frequency response, power requirements, deformation response, and does not take into account the effects of integrating multiple components. For example, only SMA wires are considered in embedded actuator models [Lago93, deBl98, Bruc02, Bruc04]. There has also been some design-related work involved with embedding power systems, such as batteries, into a wing structure [Thom04]. What now needs to be developed is an affordable and scalable approach for integrating power sources, actuators, and sensors into a single platform for deployment in a morphing structure for aerospace applications, as can be found in natural systems such as plants and animals.

Chapter 3: Thermal Behavior of Multi-Material Molded Modules

3.1 Introduction

The main concern when embedding electronic components into a module is whether or not the process will damage the components. If it were possible to embed electronic components in polymers with optimal properties, it would not be necessary to use a MMIM process, requiring several stages. Unfortunately, strength and processing temperature share a direct relationship. High strength polymers require high processing temperatures, which could severely damage sensitive electronic components. However, it is possible to inject a polymer with a low processing temperature around the electronics to act as a heat shield so that a second, higher processing temperature polymer with higher strength can be injected.

In order to design a system using any sort of MMM, whether for embedding electronics or for some other application, it is necessary to have appropriate models that can predict the effects of the multi-stage injection molding (MSIM) process on the resultant material system in addition to predicting the response of the material system when subjected to elevated temperatures. This chapter discusses the development of two models regarding the thermal performance of multi-material systems fabricated by MSIM processes. The first part of the chapter focuses on the development of a model for predicting the steady-state thermal conductivity across the multi-material interface in a module. In the latter part of the chapter, the transient thermal behavior at the core of a multi-material module is characterized when exposed to high ambient temperatures and models are developed to predict the response of MMIM modules when subjected to such conditions.

3.2 Material Selection, Molds, and Processing Conditions

In order for the model to be applicable to many different applications, the materials and processing conditions have to be chosen to account for different circumstances that one may encounter when using a MSIM process. The sample material selection process is discussed in Section 3.2.1, the fabrication of the molds is addressed in Section 3.2.2, and then the processing conditions for each material are discussed in Section 3.2.3.

3.2.1 Material Selection

Since the main application of this research is embedding electronic components in a module for use in a serpentine robot, the materials were selected in accordance with the desired design objectives in addition to being relevant to other applications. The polymers selected for analysis were chosen with several factors in mind. Cost was the main factor in choosing materials. As with the rest of the design, the material making up the modules must be inexpensive to keep the overall robot cost affordable. This limits the possible materials to pure polymers with no reinforcement particles because the added particles greatly influence the cost. However, since multiple materials will be used and the module will be solid, the lack of particles does not necessarily mean the final product will lack in strength.

The processing temperature was the next consideration for the material selection process. As discussed in Section 3.1, a low processing temperature polymer is desired to act as a heat shield for embedded electronics applications. Many non-industrial electronic components, such as the Microchip PIC12F629 and the National Semiconductor LM340 Series positive voltage regulator, have absolute maximum ratings with maximum storage temperature of 150ºC. As long as the processing temperature of the first polymer shot is 150ºC or less, the electronic components should not be damaged. Solder, such as Kester 44 rosin-core solder, typically melts at a temperature near 190ºC; solder joints will not be affected by low processing temperatures.

After searching several plastics databases, it was evident that there is essentially only one general purpose thermoplastic that is applicable in many situations while still satisfying the cost and processing temperature constraints, low density polyethylene (LDPE). LDPE has a crystalline structure and is known for being robust to the point of being almost unbreakable, while remaining flexible and maintaining good resistance to water and most organic solvents. The specific grade of polyethylene in use for this research is Dow LDPE 722. The manufacturer reported properties are shown in Table 1.

Table 1 - Dow LDPE 722 properties

Property	Nominal Value Unit	Test Method
Specific Gravity	0.918	ASTM D792
Melt Mass-Flow Rate	8 g/10 min	ASTM D1238
Tensile Modulus	140 MPa	ASTM D638
Tensile Strength @ Yield	8.89 MPa	ASTM D638
Tensile Strength, Ultimate	11 MPa	ASTM D638
Tensile Elongation @ Break	130%	ASTM D638
Flexural Modulus	226 MPa	ASTM D790
Notched Izod Impact (73 ºF)	4.1 J/cm	ASTM D256
Vicat Softening Point	90 ºC	ASTM D1525
Melting Point	105 ºC	DSC

Once the low processing temperature material was selected, the temperature constraint was modified for the candidate materials for the second shot. Even though the first layer is to protect the electronic components from the higher temperature second shot, if the first layer is not thick enough or the process temperature of the second material is too high, the electronics could still be damaged. It may be the case that increasing the thickness of the first layer results in a design that is too heavy and therefore it may be better to find a material with a combination of having good performance along with not having too high of a processing temperature.

Two general purpose candidate materials were found that have desirable mechanical properties, as well as reasonable process temperatures that would not require an extremely thick first layer, polystyrene (PS) and acrylonitrile butadiene styrene (ABS). The specific grade of polystyrene used in this research is General Polymers Hival® 5308 I/E. The properties are listed in Table 2. PS has an amorphous structure with good mechanical properties overall and it is able to be processed at temperatures around 200ºC, only slightly higher than the maximum temperature for the electronic components.

Table 2 - General Polymers Hival® 5308 I/E properties

Property	Nominal Value Unit	Test Method
Specific Gravity	1.04	ASTM D792
Melt Mass-Flow Rate	9 g/10 min	ASTM D1238
Tensile Strength @ Yield	23 MPa	ASTM D638
Flexural Modulus	2000 MPa	ASTM D790
Notched Izod Impact (73 ºF)	0.96 J/cm	ASTM D256

ABS has an amorphous structure, like that of PS; however it has a higher strength and stiffness. In lieu of this it requires higher processing temperatures, around 250ºC, which may require thicker first layers for protecting the electronics. The specific grade of ABS used in this research is General Polymers Hival® HG6; the properties are shown in Table 3.

Table 3 - General Polymers Hival® HG6 properties

Property	Nominal Value Unit	Test Method
Specific Gravity	1.04	ASTM D1505
Melt Mass-Flow Rate	4.40 g/10 min	ASTM D1238
Tensile Strength @ Yield	45 MPa	ASTM D638
Flexural Modulus	2300 MPa	ASTM D790
Notched Izod Impact (73 ºF)	3.00 J/cm	ASTM D256

Using each of the three materials above, samples are fabricated using an injection molding process. There are two types of samples fabricated; those using single stage injection molding and those using MSIM. The single stage molded samples can only contain a single material. The MSIM samples can contain one or more materials, depending on the number of materials desired. For this work, the number of materials for the MSM samples is two, since that is all that is necessary to characterize the thermal characteristics of the interface. Table 4 shows all of the possible combinations of materials and shows how many samples need to be fabricated and tested. The naming convention used is as follows, where x is a number used for identification:

- Material x – one thin layer, one material (single stage)
- Material 1x – one thick layer, one material (single stage)
- Material 2x – two thin layers, single material (multi-stage)
- Material/Material x – two thin layers, two materials (multi-stage)

Table 4 - Thermal testing samples

Sample	**1st Stage Material**	**2nd Stage Material**
LDPE x	LDPE	N/A
PS x	PS	N/A
ABS x	ABS	N/A
LDPE 1x	LDPE	N/A
PS 1x	PS	N/A
ABS 1x	ABS	N/A
LDPE 2x	LDPE	LDPE
PS 2x	PS	PS
ABS 2x	ABS	ABS
LDPE/PS x	LDPE	PS
LDPE/ABS x	LDPE	ABS
PS/ABS x	PS	ABS

3.2.2 Molds

The thermal conductivity tester in use, discussed in Section 3.3.1, requires that the samples be circular in cross-section, with a diameter less than or equal to 25 millimeters. The height of the required sample is 30 millimeters; however an insert with known conductivity can be installed so that thin samples may be used. Since injection molded parts are usually thin-walled, it was decided that a layer thickness of 2 millimeters is appropriate for this study.

A multiple piece mold was designed allowing the use of the same mold cavity for all specimens, reducing the variability that may occur if multiple molds were used. A computer-aided design (CAD) solid model of the mold cavity is shown in Figure 3.

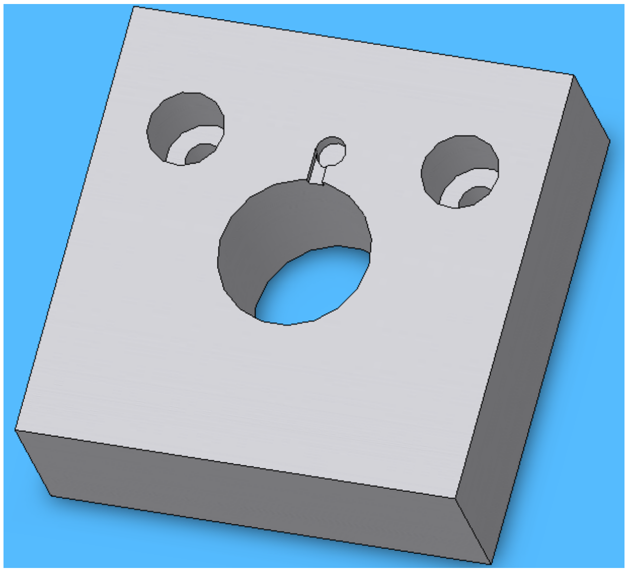

Figure 3 - CAD model of mold cavity

Aluminum was chosen for the mold material not only because of its machinability but also because of its high thermal conductivity which allows heat to be dissipated quickly after injection, resulting in uniform shapes with better dimensional stability and repeatability than less conductive mold materials.

The mold was fabricated out of 1 inch thick aluminum sheet. The sheet was cut to approximately 75 millimeters square. Each of the faces was planed using a fly-cutter to ensure a tight seal when placed in the injection molding machine. A 25 millimeter cavity was machined manually on a mill by starting with small end mills and progressing up to a boring tool. The smaller holes to the right and left of the central hole are for mounting the mold to the injection molding machine. They are 1/4” in diameter, and were also machined manually using a mill to ensure a good fit. The small circular hole above the large central hole acts as a cold material trap, which is to aid in the flow of the molten polymer when injected. The gravity-aided gate is semi-circular in cross-section and was filed down after machining to promote good flow.

Cylindrical aluminum cores were machined on a lathe to ensure a tight fit in the cavity. When in place, the cores allow disks to be molded having thickness equal to the cavity depth minus the core thickness. Two cores were used in the processing of the samples, one having thickness of 23.32 millimeters for the single layer samples, and one having thickness 21.14 millimeters for the two layer samples.

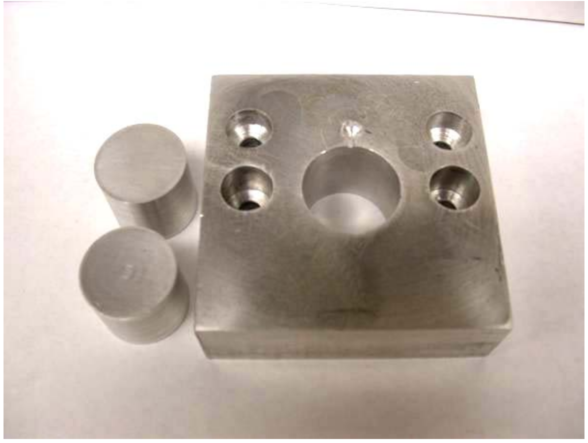

Figure 4 - Mold and inserts for disk samples

3.2.3 Processing

All of the polymers were processed in an as-received condition. The injection molder in use is the Cincinnati Milacron Babyplast 6/10, depicted in Figure 5. The Babyplast 6/10 is a small-scale molder intended for prototype development, small production runs, and laboratory testing, making it ideal for this research. The Babyplast 6/10 has a 16 millimeter piston that is able to travel up to 60 millimeters, allowing mold cavity volumes up to 12 cubic centimeters.

Figure 5 - Babyplast 6/10 injection molder

The steps involved in fabricating injection molded parts using the Babyplast 6/10 are very similar to the steps in fabricating a part in a large-scale production factory, except that some of the features are manual rather than automated. First the machine is turned on and the safety guards must be checked. The hydraulic pump that delivers the necessary pressure to the actuators can then be turned on along with the cooling water. The cooling water can be used not only for cooling the hydraulic oil, but also for cooling the mold platens.

The machine contains heaters in three locations, the plastification chamber, the injection chamber, and the nozzle. All of the heaters are turned on together at this point, since it takes several minutes for the appropriate temperatures to be reached. Adjusting the temperature settings is the next step, ensuring that the three areas containing the heaters are set at temperatures higher than the melting temperature of the polymer to be used.

While the machine is still heating up, the mold is installed. For the particular setup in use, this only requires holding the mold in position on the left platen, and securing it to the platen with two 1/4” x 20 x 1.5” screws. Once the mold is properly installed, the mold closed position is set using the manual functions.

The final preparation steps involve setting the values of the parameters for the part. These settings are injection time, cooling time, decompression distance, load material, and sprue break time. The injection pressure is the pressure that the molten polymer is subjected to in order to fill the mold. After the specified amount of injection time has passed, the injector piston backs up the amount specified by the decompression distance. This acts like a brake for the polymer flow and its purpose is to minimize the amount of polymer that exits the nozzle after the part starts cooling. The load material parameter is the distance, in millimeters, that the piston is to travel while injecting polymer into the mold. This distance is can be calculated by taking the mold volume added to the sprue volume and dividing by the piston area as shown in Equation (1).

$$LM = \frac{V_{mold} + V_{sprue}}{A_{piston}} = \frac{V_{mold} + V_{sprue}}{64\pi} \qquad \textbf{(1)}$$

The sprue break time is the amount of time that is to pass after the injection time before the carriage that moves the entire injection assembly away from the platen to break the sprue. The quality of the part may be affected if the sprue break time is set either too long or too short.

In order to keep samples as similar as possible, the injection pressure, mold pressure, decompression distance, and sprue break time were all held constant, their values listed in Table 5. The mold pressure is the amount of clamping force per unit area that keeps the mold in between the platens during injection and cooling. Other processing parameters are dependent upon the material used as well as the size of the specimen to be processed.

Table 5 - Processing parameters

Parameter	**Injection Pressure**	**Mold Pressure**	**Decompression Distance**	**Sprue Break Time**
Value	7.0 MPa	12.7 MPa	1.0 mm	0.1 sec

The processing parameters that are dependent on the material are as follows: the processing temperatures such as plastification temperature, injection chamber temperature, and nozzle temperature; material load; injection time; and cooling time. These parameters were modified on a trial and error basis until acceptable part quality was reached. An acceptable part has uniform circular shape, uniform thickness, smooth surface, does not have any flash, and does not have any traces of flow lines.

Every time the polymer material in the injection molder is switched, the machine must be purged of any material that may be residing in the plastification chamber, injection piston, or nozzle. In order to minimize the number of times the polymer granules needs to be switched and machine purged, the lowest melting temperature polymer should be the first to be processed. This is because for MMIM the material with the higher melting temperature should be injected second for better adhesion and bonding to the first, lower melting temperature polymer. In this case, the polyethylene is the first material processed.

The processing parameters in use for the single layer LDPE samples are listed in Table 6.

Table 6 - LDPE processing parameters

Parameter	Value
Plastification Temperature	150 ºC
Injection Chamber Temperature	150 ºC
Nozzle Temperature	150 ºC
Injection pressure	7.0 MPa
Mold cooling water	ON
Injection time	1.0 sec
Cooling time	4.0 sec
Decompression distance	1.0 mm
Load material	12.0 mm
Sprue break time	0.1 sec

These parameters produce high quality parts that do not require any secondary operations such as sanding or polishing before testing. Since the process is so repeatable, there is a high degree of dimensional stability because the parts all experience the same amount of shrinkage. The final dimensions of all of the LDPE single layer disks are very consistent, with thickness of 1.99 millimeters and diameter of 24.5 millimeters.

In order to produce the larger samples using the smaller core, several of the processing parameters must be changed. More time is necessary to inject all of the polymer to properly fill the larger cavity, so the injection time should be set at 5.0 seconds. In addition, the cooling time must be increased to 30.0 seconds and the load material needs to be increased to 18.0 millimeters. These changes produce parts that are also quite uniform, with thickness of 4.10 millimeters and diameter of 24.5 millimeters.

Once all of the LDPE samples are produced, the molding machine is purged several times to ensure there is no residual LDPE in the plastification or injection chambers. The plastification chamber, injection chamber, and nozzle temperatures are then increased and polystyrene, the next higher melting temperature polymer, is then placed in the hopper. Once the heaters have reached the desired temperatures, the machine is purged several more times until it can be certain that only PS is in the plastification and injection chambers. The processing parameters for the single layer PS samples are listed in Table 7.

Table 7 - PS processing parameters

Parameter	Value
Plastification Temperature	200 ºC
Injection Chamber Temperature	200 ºC
Nozzle Temperature	200 ºC
Injection pressure	7.0 MPa
Mold cooling water	ON
Injection time	1.0 sec
Cooling time	6.0 sec
Decompression distance	1.0 mm
Load material	11.5 mm
Sprue break time	0.1 sec

As is the case for the LDPE, these parameters produce high quality parts that do not require any secondary operations such as sanding or polishing before testing. The final dimensions of all of the PS single layer disks are very consistent, with thickness of 2.01 millimeters and diameter of 24.9 millimeters. For processing the larger parts, using the smaller core, the only parameter that needs to be increased is the load material, from 11.5 millimeters to 17.0 millimeters.

Once all of the PS samples are produced, the molding machine is purged several times again. The plastification chamber, injection chamber, and nozzle temperatures are then increased and ABS, the highest melting temperature polymer, is then placed in the hopper. Once the heaters have reached the desired temperatures, the machine is purged several more times until it can be certain that only ABS is in the plastification and injection chambers. The processing parameters for the single layer ABS samples are listed in Table 8.

Table 8 - ABS processing parameters

Parameter	Value
Plastification Temperature	240 ºC
Injection Chamber Temperature	240 ºC
Nozzle Temperature	250 ºC
Injection pressure	7.0 MPa
Mold cooling water	ON
Injection time	1.0 sec
Cooling time	6.0 sec
Decompression distance	1.0 mm
Load material	11.5 mm
Sprue break time	0.1 sec

The final dimensions of the single layer ABS parts using the parameters in Table 8 are 2.00 millimeters for the thickness of the disk and 24.8 millimeters for the diameter. In order to process the larger samples, the only parameter that needs adjusting is the load material value. The larger sample requires a value of 17.0 millimeters.

For the cases where MSM is used, an extra step is implemented in order to mimic a larger scale process conducted on industrial machines. As mentioned in Section 2.2, the second stage is usually injected immediately after the first stage, without allowing the part to cool down all of the way, promoting adhesion. In order to replicate this, the parts produced in the first stage were put into an oven prior to placing in the mold and having the second stage applied. The temperature of the oven and the amount of time in the oven was varied on a trial and error basis, and it was determined that 100ºC for 5 minutes promoted better and more uniform adhesion, while not causing additional shrinkage or warpage of the first stage samples.

3.3 Steady-State Thermal Conductivity Testing of Multi-Material Injection Molded Systems

This section addresses the design question, “What effect will the MMM process have on the thermal conductivity of resultant material system?” In order to design a multi-functional module for a particular application, it is necessary to know whether the MMM process promotes conduction or causes increased thermal resistance for a particular material combination. In addition, the effect of the process on the thermal conductivity must be quantified so that the steady-state behavior can be accurately modeled for the analysis of a multi-functional design prior to fabrication. The following sections discuss the steady-state thermal conductivity determination and characterization of single and multi-material systems, as well as the development of a model to account for the multi-material interfacial effects on the overall thermal conductivity.

3.3.1 Thermal Conductivity Testing Equipment and Procedure

The thermal conductivity of the multi-material systems is the only thermal property necessary to predict the steady-state performance and quantify the effects of the interface for layered configurations and modules fabricated by MSM. The particular thermal conductivity meter in use for this research is the P.A. Hilton, Ltd. H111A Linear Heat Conduction Heat Transfer Service Unit, shown in Figure 6. This unit uses a method similar to the thermal conductivity industry standard ASTM E1530 [ASTM99], where a sample is placed in between two flat surfaces, one hot and one cold, and the heat input along with the temperature difference is recorded at steady-state.

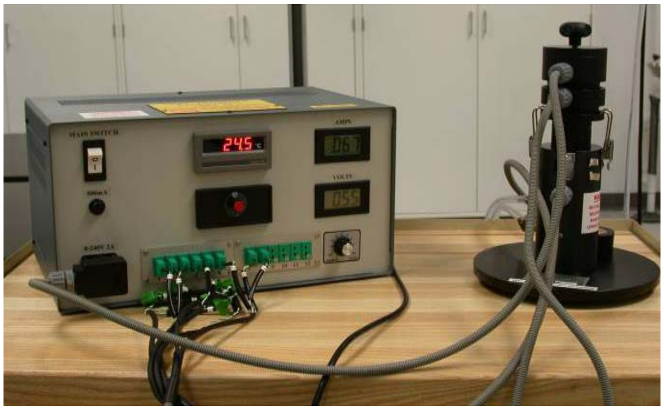

Figure 6 - P.A. Hilton H111A

For the tester in use, current is sent to a cartridge heater embedded in the piece of brass at the top of the unit as shown in Figure 7. The tester unit is connected to a fresh water faucet via polyvinyl chloride tubing to dissipate the heat away from the bottom brass piece using forced convective cooling. The brass pieces are surrounded by insulation, theoretically allowing the heat to only travel from the top to the bottom. This creates a one-dimensional temperature gradient in the vertical direction. The temperature can be measured by six thermocouples, three embedded in each of the brass pieces 15 millimeters apart at locations 7.5, 22.5, and 37.5 millimeters from the sample interfaces.

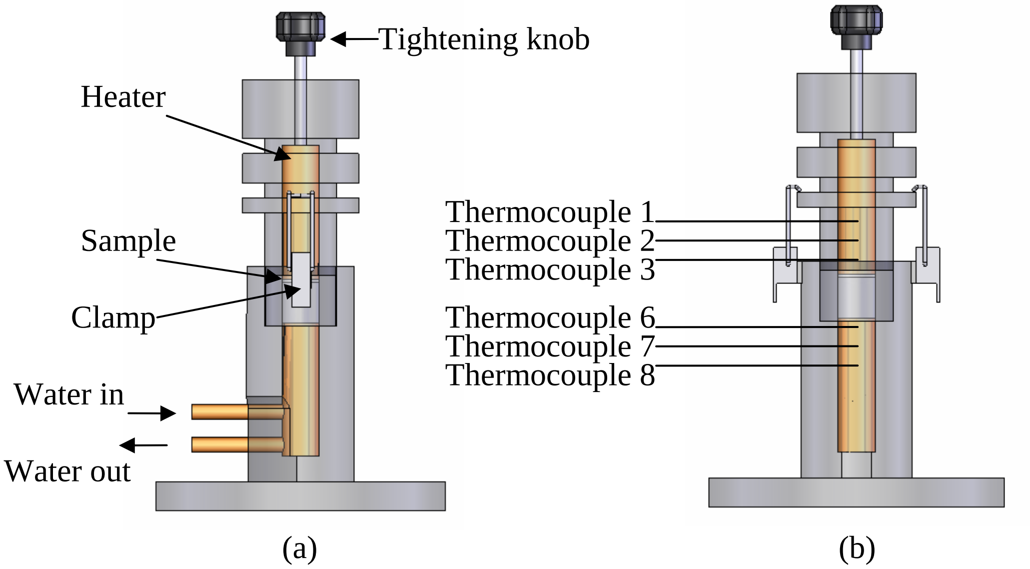

Figure 7 - Thermal conductivity tester transparent views: (a) side view, (b) front view

The tester was originally intended to measure samples 25 millimeters in diameter with one of two approximate thicknesses; either un-insulated 1.5 ± 1.5 or pre-insulated 30 ± 1.5 millimeters. This is governed by the locations of the protruding lips onto which the clamps hold. The tightening knob turns a long screw that pushes down onto the top brass piece while holding back against the threads in the top assembly which is secured by the clamps.

In order to make this setup more convenient for testing many polymer samples of various thicknesses, additional steps had to be taken. Since it was known prior to testing that conductivities of the polymers are low, insulation would have to be used. Fiberglass pipe insulation, 1/2 inch wall thickness and 1 inch inner diameter, with a thermal conductivity on the order of 0.03 W/m-K was used to help retain as much heat as possible. Using insulation requires the use of 30 millimeter samples, which is not desirable because of the large temperature difference this would require which could result in melting or other complex temperature dependent behavior. Instead, aluminum inserts were used in series with the polymer samples so that thin samples could be used. An exploded view of the tester setup is shown in Figure 8. High thermal conductivity silicone based thermal paste was used on interfaces between the polymer specimen, aluminum insert, and brass tester faces to reduce the amount of contact resistance and obtain more reproducible results.

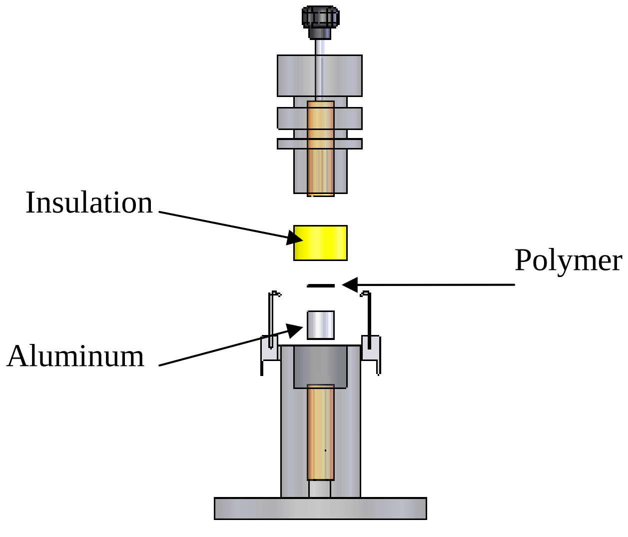

Figure 8 - Conductivity tester transparent exploded view

3.3.2 Calculations

The general equation governing heat transfer is the heat diffusion equation, shown in Cartesian coordinates as Equation (2), where ρ is the material density, c_p is the specific heat of the material, k is the thermal conductivity, and T is the temperature field.

$$\rho c_p \frac{\partial T}{\partial t} = \dot{q} + \frac{\partial}{\partial x}\left(k\frac{\partial T}{\partial x}\right) + \frac{\partial}{\partial y}\left(k\frac{\partial T}{\partial y}\right) + \frac{\partial}{\partial z}\left(k\frac{\partial T}{\partial z}\right) \tag{2}$$

For the one-dimensional, steady-state conduction case for which the thermal conductivity tester was designed, the second order, non-homogeneous partial differential equation reduces to a second order, homogeneous ordinary differential equation, given by (3).

$$\frac{d}{dx}\left(k\frac{dT}{dx}\right) = 0 \tag{3}$$

If the thermal conductivity is assumed to be constant through the material, then the general solution to Equation (3) can be obtained by integrating two times to obtain a linear temperature field given by Equation by Equation (4) where C_1 and C_2 are determined from the boundary conditions.

$$T(x) = C_1 x + C_2 \tag{4}$$

For the case of the thermal conductivity meter, the boundary conditions for the solution are the temperatures at the top of the sample $x = 0$ and $x = L$, where L is the thickness of the sample being tested. However, there are no thermocouples located on the faces to give theses temperatures, instead the required temperatures are obtained by extrapolation since the temperatures are known at six other locations and the heat conduction through the brass is expected to be a linear function of distance.

Since the closest thermocouple, is 7.5 millimeters from the face, and the thermocouples are 15 millimeters apart, Equation (5) and Equation (6) give the temperatures at the hot (top) face and the cold (bottom) face respectively. The subscripts indicate from which thermocouple in Figure 7 the temperatures are obtained.

$$\frac{T_3 - T_{hot}}{7.5mm} = \frac{T_2 - T_3}{15mm} \rightarrow T_{hot} = T_3 - \frac{T_2 - T_3}{2} \tag{5}$$

$$\frac{T_{cold} - T_6}{7.5mm} = \frac{T_6 - T_7}{15mm} \rightarrow T_{cold} = T_6 + \frac{T_6 - T_7}{2} \tag{6}$$

Assuming that there is negligible contact resistance and the temperatures at the top and bottom of the sample are the same as the temperatures on the hot and cold faces, then the boundary conditions can be applied and the constants can be found. Solving Equation (4) with the temperatures of the faces gives the equation of the temperature field, shown in Equation (7).

$$T(x) = (T_{cold} - T_{hot})\frac{x}{L} + T_{hot} \tag{7}$$

The constitutive equation for conduction through a homogeneous medium is Fourier's law, given by Equation (8) in one-dimensional form, which relates the conduction heat transfer rate q , to the temperature distribution, the thermal conductivity, and the area, *A*, which is in the direction normal to the heat transfer.

$$q = -kA\frac{dT}{dx} \tag{8}$$

Taking the derivative of the temperature field, the result is the one-dimensional, steady-state conduction equation. Substituting the Joule heating relation for the heat flux, where V is voltage and I is the current input to the heater, gives an equation suitable for determining the thermal conductivity using the described setup.

$$q = VI \Rightarrow VI = \frac{kA}{L}\left(T_{hot} - T_{cold}\right) \tag{9}$$

Although this equation may be sufficient to test specimens with relatively high thermal conductivities, such as metals, there are other issues that arise for testing of low conductivity polymers. Perhaps the more obvious issue is that the polymer specimens require the use of the aluminum inserts as described in the previous section. The thermal resistance of the aluminum insert must also be accounted for when calculating the thermal conductivity of the sample between the hot and cold brass faces.

The thermal resistance for a one dimensional series thermal system analysis can be treated in the same manner as the electrical resistance for a series electrical circuit, the equivalent resistance is just the sum of the individual resistances. The thermal resistance for conduction, R_{cond} of a given component of the system is given by

$$R_{cond} = \frac{L}{kA} \tag{10}$$

For the test setup, the specimen is in series with an aluminum piece so which makes the total thermal resistance, R_{tot}, the sum of the thermal resistances for the polymer sample (subscript p) and insert (subscript i).

$$R_{tot} = \frac{L_p}{k_p A_p} + \frac{L_i}{k_i A_i} \tag{11}$$

By defining the thermal resistance similar to the electrical resistance, the ratio of the potential to the corresponding rate, the parameters in Equation (11) can be related to the temperatures on the hot and cold faces as well as the heat flux rate.

$$R_{tot} = \frac{\Delta T}{q} \Rightarrow \frac{L_p}{k_p A_p} + \frac{L_i}{k_i A_i} = \frac{T_{hot} - T_{cold}}{q} \tag{12}$$

Since the aluminum inserts were machined on a lathe the exact specification, 25.00 millimeters, and the polymer samples experienced a small amount of radial shrinkage making them slightly under 25 millimeters, the area is assumed to be constrained by the size of the polymer specimen and for all of the calculations A_i was set to equal A_p. Taking this into consideration and solving for k_p:

$$k_p = \frac{q k_i L_p}{\left(T_{hot} - T_{cold}\right) A_p k_i - q L_i} \tag{13}$$

After testing several samples and obtaining thermal conductivity data on the order of approximately 200% higher than the conductivities that were expected, it was determined that a significant amount of heat was escaping through the upper portion of the tester, resulting in a very large amount of error. Since Fourier's law and the subsequent derivation only accounts for the heat rate into the sample, an extra term should be applied to account for the rate of the heat flow leaving the tester without passing through the sample.

$$q = VI - q_{loss} \tag{14}$$

If the one-dimensional version of the Fourier's law is modified to include a rate of energy storage term for the upper brass part of the specimen, then Equation (8) and Equation (14) become:

$$\rho c_p V \frac{dT}{dt} + kA\frac{dT}{dx} = VI - q_{loss} \tag{15}$$

If there is no sample in place, then the second term in Equation (15) is zero, and all that is left are the heat rate terms and the rate of energy storage for the brass piece. If the rate of change of temperature for the brass piece is zero, meaning it reaches steady-state, then the left hand side of Equation (15) is zero and $VI = q_{loss}$.

Using this fact in order to account for the error, the tester was run at different input power settings using a 24.0 millimeter diameter and 26.0 millimeter thick piece of extruded polystyrene foam insulation as the sample, which has an advertised thermal conductivity on the same order as air, approximately 0.03 W/m-K, a much larger thermal resistance than the polymer samples of interest. Once the tester reached equilibrium, the voltage, current, and temperatures of all of the thermocouples were recorded. The most important temperature for this test was T_1, the temperature at the top most thermocouple since it is the highest temperature and could be used as a point of reference for the future tests. The results of these tests are shown in Figure 9.

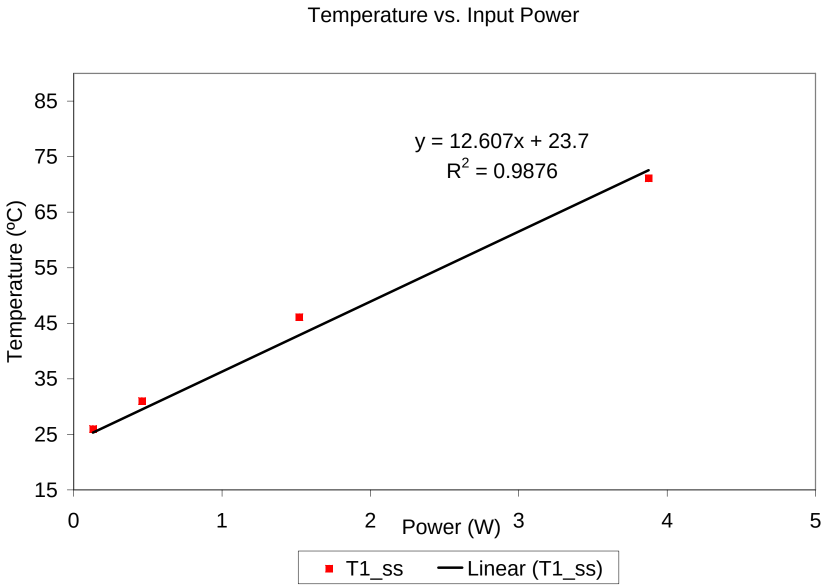

Figure 9 - Plot of T1 vs. Heat Rate for insulation

The equation in Figure 9 shows the temperature of the top thermocouple (*y*) with respect to the amount of heat input (*x*), where the fit was forced to intercept the *y*-axis at the initial temperature, 23.7°C, since this corresponds to zero heat input. As Equation (14) implies, this rate of heat input is equal to the rate of heat output at steady-state, meaning that if the equation is solved for x in terms of y, the rate of heat loss can be found at any given temperature. The resulting rate of heat loss expression is shown as Equation (16).

$$q_{loss} = \frac{T_1 - 23.7}{12.607} \text{ (W)} \tag{16}$$

Once the heat loss could be accounted for, the results obtained for the thermal conductivity values were much more closely matched with the expected thermal conductivities for the single stage, single material samples. The results of the thermal conductivity tests are discussed in the following section.

3.3.3 Thermal Testing Results

Each material combination shown in Table 4 was tested two times, with all tests being run at a steady-state temperature of $T_1 = 57 \pm 2\ {}^{\circ}C$, where steady-state was determined to be when the temperature fluctuated less than 0.05ºC/min, which is beyond the 0.1ºC/min called for by the industry standard [ASTM99]. In the second round of testing, different specimens made at the same time as the specimens from the first round of testing were used. The averaged results for the pure single shot samples are shown in Table 9.

Table 9 - Thermal conductivity values

Material	**Measured thermal conductivity (W/m-K)**
LDPE	0.39
ABS	0.18
PS	0.19

Theoretical values for multi-material systems can be calculated using a rule of mixtures model for series thermal resistance, as is shown in Equation (17), where V_i is the volume fraction of the i^{th} component.

$$\frac{1}{k_{sys}} = \sum_{i=1}^{n} \frac{V_i}{k_i} \tag{17}$$

However, for the one-dimensional case with constant cross-sectional area, Equation (17) can be reduced to only consider the lengths of the components as is given by Equation (18), where L_i is the length fraction of the i^{th} component.

$$\frac{1}{k_{sys}} = \sum_{i}^{n} \frac{L_i}{k_i} \tag{18}$$

Using this equation, theoretical values for each of the multi-material systems were obtained for each round of tests, the results of which along with average measured bulk thermal conductivities and the resultant levels of adhesion are shown in Table 10.

Table 10 - Results of thermal conductivity tests

Specimen	Measured Conductivity (W/m-K)	Predicted Conductivity (W/m-K)	Adhesion	Change in Conductivity (%)
LDPE x	0.39	n/a	n/a	n/a
LDPE 1x	0.32	n/a	n/a	n/a
LDPE 2x	0.33	0.39	good	-15
LDPE x, LDPE x	0.33	0.39	none	-15
ABS x	0.18	n/a	n/a	n/a
ABS 1x	0.18	n/a	n/a	n/a
ABS 2x	0.18	0.18	good	0
ABS x, ABS x	0.15	0.18	none	-17
PS x	0.19	n/a	n/a	n/a
PS 1x	0.14	n/a	n/a	n/a
PS 2x	0.17	0.19	good	-11
PS x, PS x	0.15	0.19	none	-21
PE/PS x	0.24	0.25	poor	-4
PE x, PS x	0.23	0.26	none	-12
PE/ABS x	0.22	0.24	poor	-8
PE x, ABS x	0.20	0.25	none	-20
PS/ABS x	0.17	0.18	good	-6
PS x, ABS x	0.18	0.18	none	0

It can be seen from this data that, in most cases, there is an effect of the interface that causes an added thermal resistance, resulting in lower conductivity values. As a means of quantifying the difference in thermal conductivity cause by the addition of an interface, an interface correction term can be applied to the rule of mixtures model as shown by Equation (19).

$$\frac{1}{k_{sys}} = \sum_{i=1}^{n} \frac{V_i}{k_i} + \left(\frac{V}{k}\right)_{\text{interface}} \qquad \textbf{(19)}$$

Using this equation, the interface correction term can be found for each of the multi-stage cases tested, as shown in Table 11.

Table 11 - Thermal conductivity results with correction terms

Specimen	**Measured Conductivity (W/m-K)**	**Predicted Conductivity (W/m-K)**	**Adhesion**	$\left(\frac{V}{k}\right)_{\text{interface}}$ **(W/m-K)$^{-1}$**
LDPE 2x	0.33	0.39	good	0.47
LDPE x, LDPE x	0.33	0.39	none	0.47
ABS 2x	0.18	0.18	good	0.00
ABS x, ABS x	0.15	0.18	none	1.11
PS 2x	0.17	0.19	good	0.62
PS x, PS x	0.15	0.19	none	1.40
PE/PS x	0.24	0.25	poor	0.17
PE x, PS x	0.23	0.26	none	0.50
PE/ABS x	0.22	0.24	poor	0.38
PE x, ABS x	0.20	0.25	none	1.00
PS/ABS x	0.17	0.18	good	0.33
PS x, ABS x	0.18	0.18	none	0.00

This data indicates that in some cases the interface correction term is high, meaning there is a large effect on thermal conductivity caused by the multi-material configuration, and in other cases the correction term is low or even zero, indicating that there is little or no effect thermal performance of the system. In the case of two layers of LDPE, the same result is achieved when the module is fabricated using MSM or when the module is fabricated by discrete layers and molded at different times. In the case of a PS and ABS system, the results show that it is more beneficial to use MMM than discrete layer fabrication if the system is chosen for its insulating performance. However, the same is not true for a LDPE and ABS system or an ABS layered configuration. Conversely, these layered systems are more conductive when MMM is used than in the case of discrete layered fabrication.

All of these observations lead to the conclusion that no major generalizations can be made about the effect of the MSM process on the performance of a multi-material system since the thermal behavior of the system is highly dependent on the constituent materials and their interactions with each other. In lieu of this fact, there are generalizations that can be made regarding the average values of the correction terms regarding the adhesion levels. Table 12 shows the mean value of the correction terms for each of the levels of adhesion.

Table 12 - Mean correction term values for each adhesion level

Adhesion Level	**Mean** $\left(\frac{V}{k}\right)_{\text{interface}}$ **(W/m-K)$^{-1}$**
Good	0.47
Poor	0.27
None	0.90

The data indicates that having poor adhesion results in the lowest interface correction term, followed by good adhesion and then no adhesion. Since the thermal conductivity of the material system varies with the inverse of the correction term, this shows that if the desired thermal performance is conducting heat, then using MSM, with either good adhesion or poor adhesion, is a much better choice than using a discretely layered fabrication method because the effects of the interface are not as detrimental to the thermal conductivity.

3.4 Transient Thermal Testing of Multi-Material Injection Molded Modules

Although a steady-state analysis can be helpful in predicting the temperature gradients caused by the embedded electronics dissipating heat in a controlled environment, a transient analysis must be completed in order to understand the complex behavior of the polymers when the conditions are suddenly changed. If the design of a MMIM module with embedded electronic components is to be used for a structure such as a serpentine robot in actual search and rescue environments, there may be conditions, such as nearby fires, which could potentially harm the embedded electronics. If the robot is equipped with an ambient temperature sensor and appropriate models have been developed that have been shown to provide accurate predictions of the transient thermal response, then the appropriate measures can be taken to ensure the embedded electronic components are not damaged from thermal loading.

The following sections describe the fabrication of the multi-material specimens and the test conditions they were subjected to in order to determine the transient thermal response at the core of heterogeneous injection molded modules when subjected to a sudden increase in ambient temperature.

3.4.1 Specimen Fabrication and Experimental Setup

A sphere was the geometry for the transient thermal response experiments because it is the only three-dimensional structure that is symmetric about any plane through its cross-section, which makes the complicated three-dimensional, transient heat transfer problem more manageable by reducing it down to a one-dimensional problem. It was decided that the sphere should be as large as possible, given the constraints of the available injection molder, so as to represent the size of a module for a future serpentine robot. Using Equation (1) and leaving some margin for error, it was calculated that one solid hemisphere with a 12.5 millimeter radius and one hollow hemisphere with the same inner radius and a 17.5 millimeter outer radius could be molded using the Babyplast 6/10.

In all, there were five mold halves that were manufactured to the above specifications in order to fabricate the spherical module. The molds were first modeled in the CAD software SolidWorks, and then exported to Pro/Engineer where the Pro/Manufacturing kernel was used to develop the appropriate machine code for a three-axis computer numerically controlled (CNC) Benchman XT mill made by Light Machines. The molds were made out of polyurethane tooling board purchased from Freeman Supply Company. The molds were designed in a manner to allow for a thermocouple to be embedded in the center of the spheres. The thermocouple was an as-received Omega type K thermocouple, with each thermocouple wire having diameter 0.032 inches, and insulated with fiberglass. Two spheres were fabricated both with embedded thermocouples, one containing only the Dow LDPE 722 and the other containing the LDPE as the inner sphere material and the General Polymers Hival® HG6 ABS as the outer sphere material. The multi-material sphere and the respective molds for each stage of the molding process are shown in the following figures.


(a) (b)

Figure 10 - (a) LDPE hemisphere with embedded thermocouple and first stage mold, (b) LDPE sphere with embedded thermocouple and second stage mold

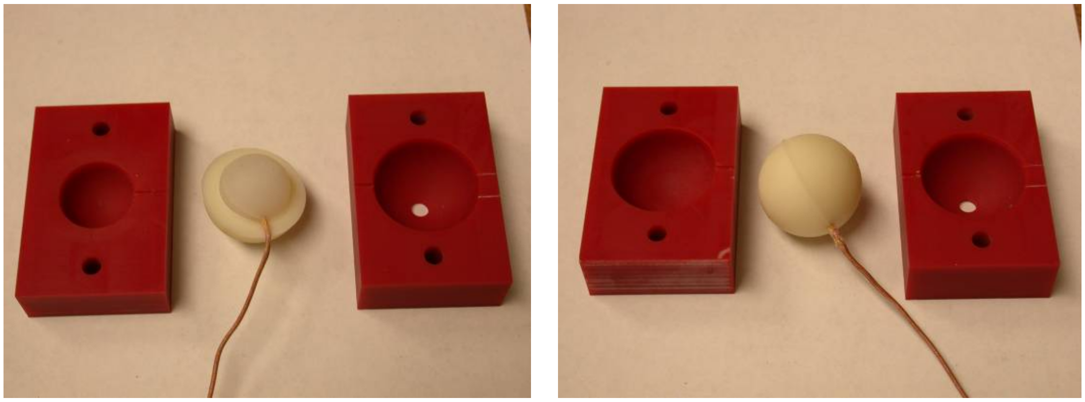
(a) (b)

Figure 11 - (a) ABS hemisphere over LDPE sphere and third stage mold, (b) final multi-material sphere and fourth stage mold

It must be noted that these are not perfect spheres. The molds themselves are approximations of spheres when machined, and when the parts are processed there is some shrinkage that may have some directional preference. Several measurements were taken at different locations and orientations and the average value was taken.

The homogeneous LDPE sphere average final diameter after shrinkage was 34.7 millimeters, while the heterogeneous sphere had an average inner diameter of 24.6 millimeters and an average outer diameter of 35.1 millimeters.

The transient thermal experiments were designed as follows. The spheres, initially at equilibrium at room temperature, approximately 23ºC, were placed in an oven at an elevated temperature and temperature at the center of the sphere as well as the ambient temperature inside the oven was recorded every thirty seconds for approximately three hours by the Omega HH506R digital thermometer connected to a computer via serial cable. The cases tested are shown in Table 13. The experimental temperatures were chosen to be halfway between the melting temperature of the LDPE and room temperature, just below the melting temperature, and half the difference between room temperature and the melting temperature above the melting temperature, approximately 60ºC, 100ºC and 135ºC respectively. The first of these temperatures is also very close to the temperature at which the thermal conductivity measurements were made for comparison purposes.

Table 13 - Materials and ambient temperatures for transient thermal experiments

Layer 1 Material	Layer 2 Material	Ambient Temperature (ºC)
LDPE	LDPE	60
LDPE	LDPE	100
LDPE	LDPE	135
LDPE	ABS	60
LDPE	ABS	100
LDPE	ABS	135

3.4.2 Transient Thermal Experiment Results

The results of the thermal tests are shown in Figure 12, where the results have been normalized using Equations (20) and because of small discrepancies in the initial and ambient temperatures during the tests.

$\theta^* \equiv$ normalized temperature
$T_\infty \equiv$ ambient temperature
$T_i \equiv$ initial temperature

$$\theta^* = \frac{T - T_\infty}{T_i - T_\infty} \qquad \textbf{(20)}$$

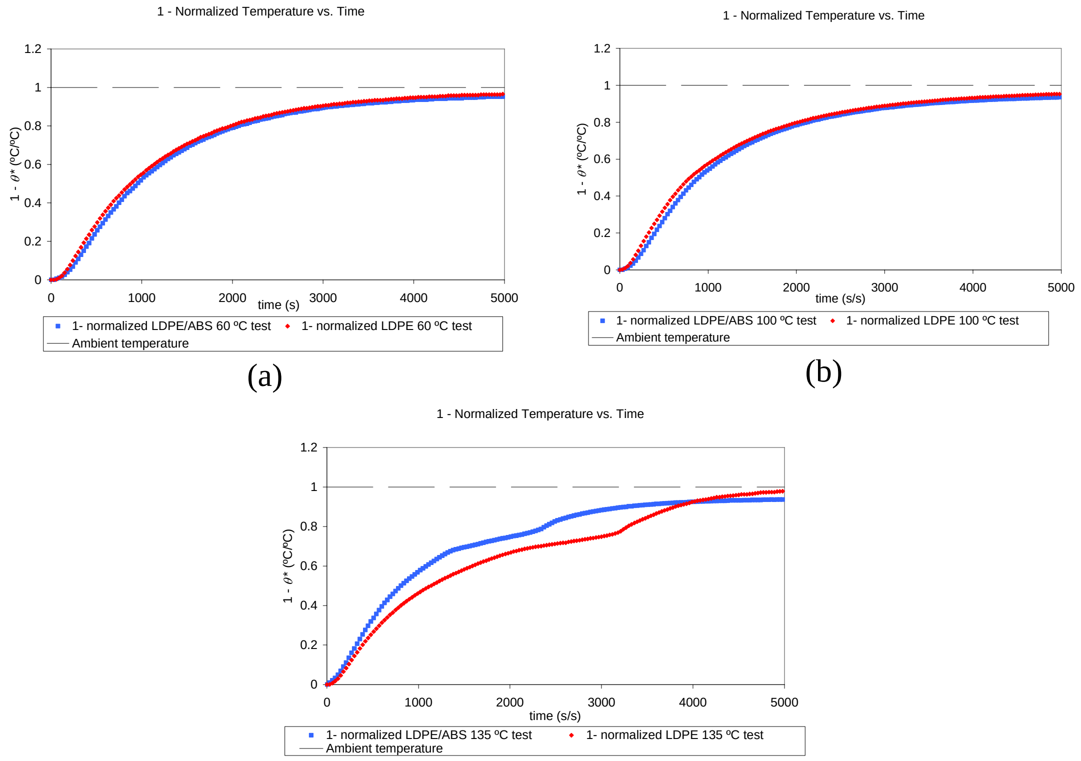

(a)

(b)

(c)

Figure 12 - Normalized transient thermal test data: (a) 60ºC, (b) 100ºC, (c) 135ºC

The 60ºC and 100ºC tests produce almost identical results, however, the 135ºC test shows much different behavior experienced by the LDPE module than the LDPE/ABS module. Both graphs share the same feature at $\theta^* \approx 0.77$, which is the point at which the LDPE at the center of the spheres completely changes phase, however, it takes a much longer time for the center of the LDPE module to complete the phase change than the center of the LDPE/ABS module. It can also be noticed that for the 135ºC test the LDPE has a slower response from the beginning of the test, whereas the opposite is true for the 60ºC and 100ºC tests. This can be attributed to the fact that the outer parts of the sphere begin changing phase immediately when placed into the 135ºC environment. Due to the latent heat of fusion, all of the energy gets absorbed in the phase change and does not increase in temperature until the phase change is complete. According to [Daws05], the thermal conductivity also drops for many polymers by approximately twenty to thirty percent upon changing phase, which may also be the case for this LDPE.

3.4.3 Transient Conduction in the Sphere - Analytical Solution

Due to the symmetry of the problem, the heat equation for the sphere can be reduced to one dimension as shown as Equation (21), where *r* is the radial direction variable.

$$\frac{1}{r^2}\frac{\partial}{\partial r}\left(\frac{k}{r^2}\frac{\partial T}{\partial r}\right) = \rho c_p \frac{\partial T}{\partial t} \tag{21}$$

For the case of convective boundary conditions, as is the case for these experiments, an analytical solution can be obtained of the form:

$$\theta^* = \sum_{n=1}^{\infty} C_n \exp\left(-\frac{\zeta_n^2 kt}{\rho c_p r_o^2} \right) \frac{1}{\zeta_n r^*} \sin\left(\zeta_n r^*\right) \tag{22}$$

where

$$C_n = \frac{4\left[\sin(\zeta_n) - \zeta_n \cos(\zeta_n)\right]}{2\zeta_n - \sin(2\zeta_n)} \tag{23}$$

and the discrete values of ζ_n are the positive roots of the Equation (24), tabulated by [Schn55]

$$1 - \zeta_n \cot \zeta_n = Bi \tag{24}$$

$$Bi = \frac{hr_o}{k} \tag{25}$$

with *h* being the convection coefficient for the surrounding atmosphere [Incr02].

These equations assume that the sphere is homogenous throughout and has constant properties at all temperatures. An approximation must be used for this solution since it is an infinite series. However, enough terms can be taken that the series converges to the correct solution. A MATLAB code, originally developed by Prof. Gerry Recktenwald [Reck06], was modified to calculate the analytical solution by solving Equations (22)-(24) with the appropriate initial conditions until the value of the convection coefficient *h* with the best correlation to the data was obtained. In order to determine the best correlation, Pearson's coefficient was calculated at increasing integer values of the convection coefficient. The best correlation was achieved with a Pearson's coefficient of 0.9999 for the 60ºC test and 0.9985 for the 100ºC test both with a convection coefficient of 12 W/m^2-K. The analytical solution with a convection coefficient of h=12 W/m^2-K and n = 300 is plotted against the data from the transient thermal experiments in Figure 13. The value of the thermal conductivity used corresponds to the value measured using the setup described in Section 3.2. The density was calculated by taking an average of the mass of the samples fabricated for the thermal conductivity measurements to the nearest 0.001 gram and dividing it by the calculated cylindrical volume. The specific heat value used in the calculation was c_p = 2200 J/kg-K, obtained from the literature.

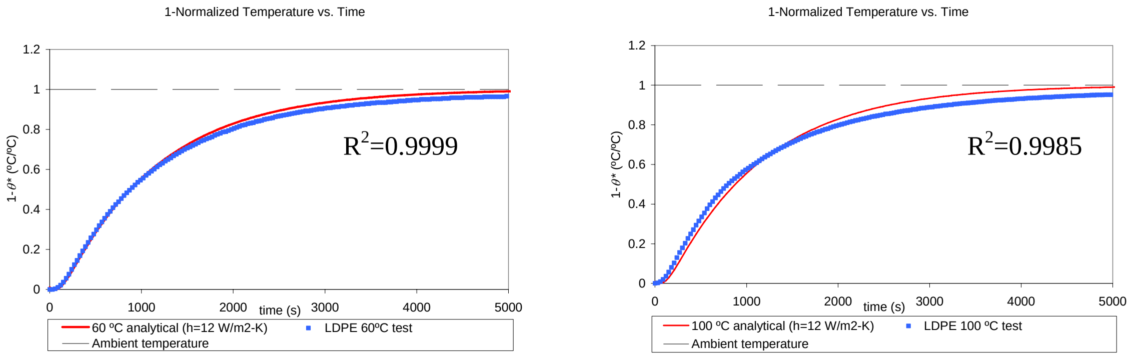

(a) (b)

Figure 13 - Analytical solution plotted against test data: (a) 60ºC case, (b) 100ºC case

Since the test at the 135ºC temperature experienced such complex behavior, the analytical solution does not pertain and is therefore left out for the case of phase changes.

3.5 Models for Transient Thermal Experiments

There are several different models that can be developed to predict the thermal response of a multi-material module when subjected to transient thermal loading including variations of the homogeneous analytical solution, a data fitting formula, and finite element models. Investigations of each of these types of models are completed in the following sections.

3.5.1 Variations of the Homogeneous Analytical Solution

The rule of mixtures (ROM) is a homogenization method that can be employed to model the physical and thermal properties of multi-material modules so that the analytical solution described in Section 3.4.3 can be used to predict the transient response when subjected to convective boundary conditions. The standard form was previously discussed in Section 3.3.3, which accounts for the volume fraction of each of the constituent materials. Using this method, the resulting parameters for the LDPE/ABS spherical structure are shown in Table 14.

Table 14 - Thermal and physical property values for ROM

Component Material	Volume (mm^3)	Volume Fraction	Density (kg/m^3)	Thermal Conductivity (W/m-K)	Specific Heat (J/kg-K)
LDPE	7795	0.344	890	0.39	2200
ABS	14848	0.656	990	0.18	2000
LDPE/ABS	22643	1	960	0.25	2100

Using these homogenized values, the same convection coefficient and number of terms in the series as was the case for the homogeneous LDPE sphere, h=12 W/m^2-K and n = 300, the analytical solution was used to model the response of the LDPE/ABS sphere. The resulting plot of the analytical solution and experimental data is shown in Figure 14. The value of Pearson's coefficient is 0.9985 for the 60ºC case, and 0.9967 for the 100ºC case, with all points considered from t = 0 to t = 10020 seconds.

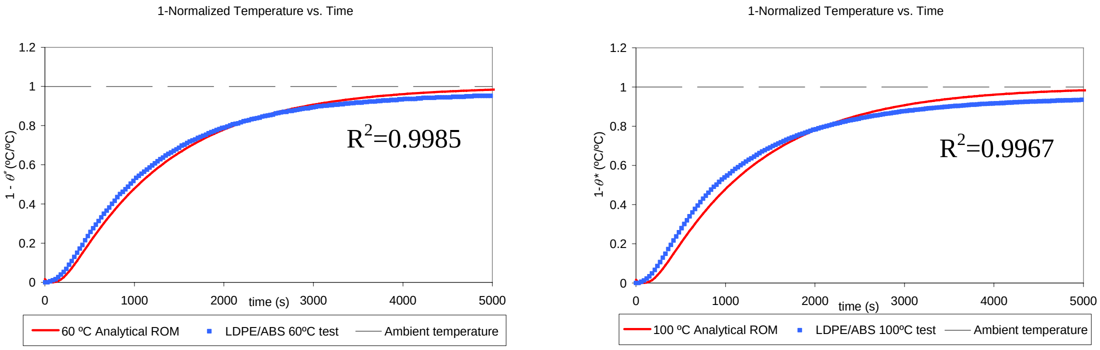

(a) (b)

Figure 14 - Analytical solution with ROM and test data: (a) 60°C case, (b) 100°C case

While the correlation of the standard ROM model and the test data for the LDPE/ABS sphere is sufficient for predicting the thermal response and could possibly be extended to other multi-material systems, the symmetry of the spherical structure allows another variation of the analytical solution by using the radius or thickness fraction rather than the volume fraction. The representative equation for this type of rule of mixtures homogenization, from here on referred to as radial ROM, is given by Equation (26), where x_i is the parameter under investigation and r_f is the radius fraction, giving the overall property for the composite X_c. Using this relation, the input parameters for the analytical solution shown in Table 15 can be calculated.

$$X_c = \sum_{i=0}^{n} r_f x_i \tag{26}$$

Table 15 - Thermal and physical property values for radial ROM

Component Material	Radius (mm)	Radius Fraction	Density (kg/m^3)	Thermal Conductivity (W/m-K)	Specific Heat (J/kg-K)
LDPE	12.3	0.701	890	0.39	2200
ABS	(17.55-12.3)=5.25	0.299	990	0.18	2000
LDPE/ABS	17.55	1	920	0.33	2100

Using a one dimensional radial ROM methodology, rather than the standard volumetric ROM, results in a decreased density, increased thermal conductivity, and the same specific heat for the model. The analytical solution with these homogenized values as the input parameters are plotted along with the experimental data are plotted in. A value of Pearson's coefficient of 0.9999 was calculated for the 60ºC case and a value of 0.9995 was calculated for the 100ºC case.

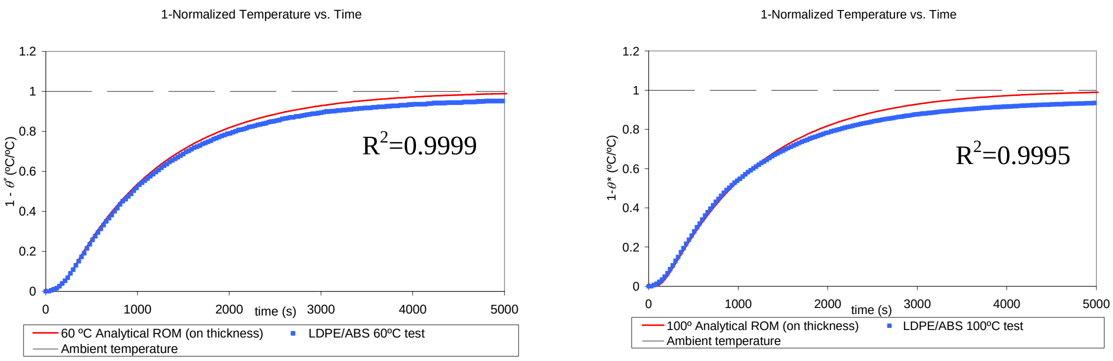

(a) (b)

Figure 15 - Analytical solution with radial ROM and test data: (a) 60ºC case and (b) 100ºC case

Clearly the radial ROM model shows better correlation with the experimental data than the standard ROM model using volume fractions. This is because the decreased density input parameter along with the constant specific heat term lower the energy storage capacity but this is offset by the increased thermal conductivity resulting in a faster response to the elevated environment temperature at the center of the multi-material module.

Unfortunately, although the ROM models have been shown to be able to accurately represent the transient thermal response of the multi-material module, there are shortcomings. As can be seen from all of the plots, the final temperature of the experimental data is less than the final temperature obtained from the homogenized models with the analytical solution even though the initial response is captured quite well. In addition, these models cannot address the complex behavior of the systems observed during the 135ºC test because the analytical solution must contain constant, non-temperature dependent properties. In order to address these issues, other models were developed which are explained in the following sections.

3.5.2 Exponential Fit Formula

In order to overcome the problems associated with using the ROM models and the analytical solution, an exponential formula was developed. The equation uses a general exponential format, similar to the analytical solution to the transient, one-dimensional conduction heat equation, but uses only three terms rather than an infinite series. The exponential fit equation is shown as Equation (27).

$$T(t) = T_i \exp(-c_2 t) + \left[T_i \exp(-c_1 t) + T_f\left(1 - \exp(-c_1 t)\right)\right]\left(1 - \exp(-c_2 t)\right) \qquad \textbf{(27)}$$

The T_i and T_f terms represent the initial and final temperatures of the data set. The c_1 and c_2 terms are constants that represent the thermal and physical parameters of the outer and inner layers of the multi-material structure respectively.

Using the Curve Fitting Toolbox in MATLAB 7.0, the homogeneous LDPE data can be imported and the constants can be determined using a nonlinear least squares method and the trust region algorithm developed in [Bran99]. The constants for the 60ºC case and 100ºC case were calculated, but for the 135ºC case the constants were assumed to have the same values as for the 100ºC case. This is because the phase change experienced by the polymer violates the general trend of the exponential fit formula. The values of the constants used for the exponential fit are shown in Table 16 and the resulting plots are shown in Figure 16.

Table 16 - Exponential fitting parameters

	60ºC case	**100ºC case**	**135ºC case**
c_1	0.000878	0.000787	0.000787
c_2	0.00357	0.00693	0.00693

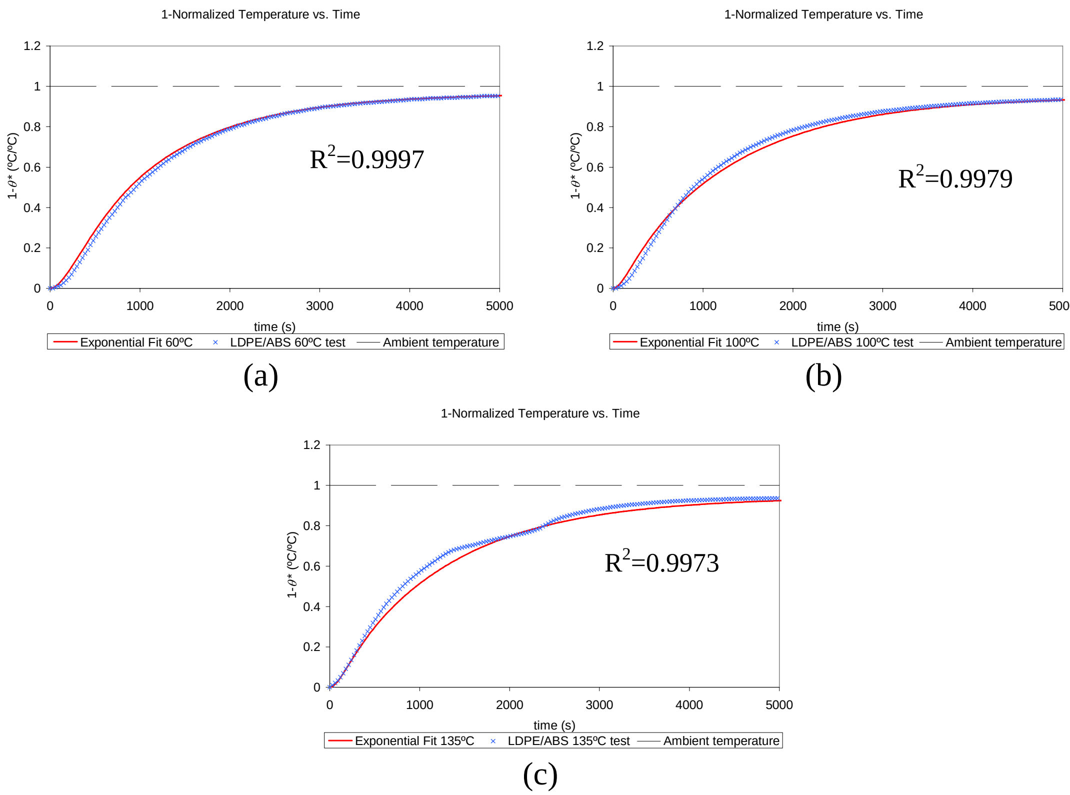

(a) (b) (c)

Figure 16 - Exponential fit and test data: (a) 60ºC case, (b) 100ºC case, and (c) 135ºC

It can be seen from the values that if the constant c_1 represents the properties of the outer ABS layer of the module, it is less affected by the test conditions than the constant c_2 representing the LDPE inner part of the module. This is quite logical since the ABS has a higher melting temperature and is expected not to be as affected by temperatures that are not too much higher than its maximum service temperature of approximately 100-110ºC. The decrease from the first test to the second test is less than 11 percent for the constant c_1. Alternatively, the constant c_2 experiences a large increase in value from the first test temperature to the next; approximately 94 percent difference. This shows that these particular test conditions have a much larger impact on the LDPE than the ABS, which makes an even better case for using multi-material systems in the design of modules with embedded electronic components.

Although the exponential fit developed in this section is an excellent formula to use for determining the thermal response at a single point of a multi-material spherical module when subjected to elevated temperatures, it can only be extended to other multi-material configurations if the material behavior data is known ahead of time. As was the case here, the experimental data is required as an input in order to determine the fitting constants. In addition, although the exponential formula may be applicable to other geometries whose thermal behavior is dominated by a single direction, such as long cylindrical geometries or plane walls, this severely limits the number of potential applications for MMIM modules. As a means of addressing the transient heat conduction problem in higher dimensions for multi-material modules, a finite element model was developed and is discussed in the following section.

3.5.3 Finite Element Model

A finite element model was designed using the computer-aided design software package I-DEAS 11. I-DEAS is divided into different modules and each module contains tasks. In order to develop the finite element model, a solid model of the spherical geometry must first be designed using the Master Modeler task in the Solid Modeling module. In I-DEAS, this seemingly simple task requires a trick in order to avoid errors when meshing. Basically, a sphere must be created from some other solid geometry, such as a block using fillets, in order for it to be meshed without errors. The larger sphere is modeled first, with the same diameter as the outer diameter of the LDPE/ABS sphere in the experiments. In order to make it simpler to assign different material properties to the model, a spherical hole, with diameter equal to the LDPE sphere diameter in the experiments, must first be cut out of the center of the sphere. The same size sphere is then added back into the larger sphere, but when joined, the partition option with tangent surface chaining must be chosen to create surfaces between the inner spherical geometry and the outer layer so that the two volumes are distinguishable from each other.

Once the spheres have been modeled, the Meshing task is selected. Since it was decided to model the module as three-dimensional, in spite of the obvious symmetry that was exploited for the previous models, the elements were also chosen to be three-dimensional. Ten node, solid parabolic tetrahedral elements were selected, as they are the best choice for approximating the curved geometry. The element length selected for the analysis was the default length for this size geometry, 2.7077 millimeters, resulting in 1766 elements in the LDPE portion of the model and 5758 elements in the ABS portion of the model when the maximum area plane meshing was used with automatic mesh checking turned on. A node was placed at the center of the sphere to ensure have comparable results as what was obtained with the embedded thermocouple. The LDPE and ABS elements were assigned the same properties as were shown for LDPE and ABS in Table 15. Figure 17 shows different model views of the meshed module, where the blue elements have the LDPE properties and the green elements have the ABS properties.

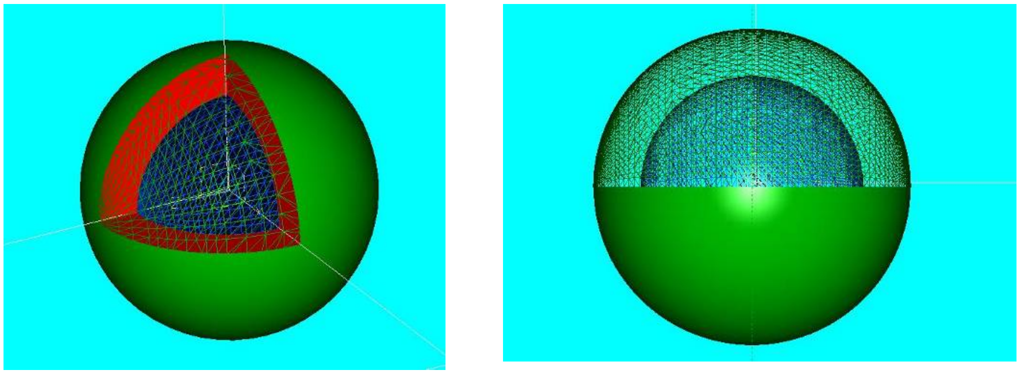

Figure 17 - Views of meshed spherical structure

The TMG Thermal Analysis software package that is incorporated into I-DEAS 11 was used for the transient heat transfer simulations. The initial simulation incorporated the same conditions as were observed for the experiments. The model had free convective boundary conditions, where the solver used the empirical relation for the sphere found in [Incr02] to determine the convection coefficient based upon the temperature at the outer surface. The ambient and initial temperature values were entered corresponding to the experiments. The solving method selected was the backward finite difference technique with the auto-calculation of the time steps so as not to exceed a temperature change of more than one degree. Figure 18 shows the results of the simulations at the three test temperatures.

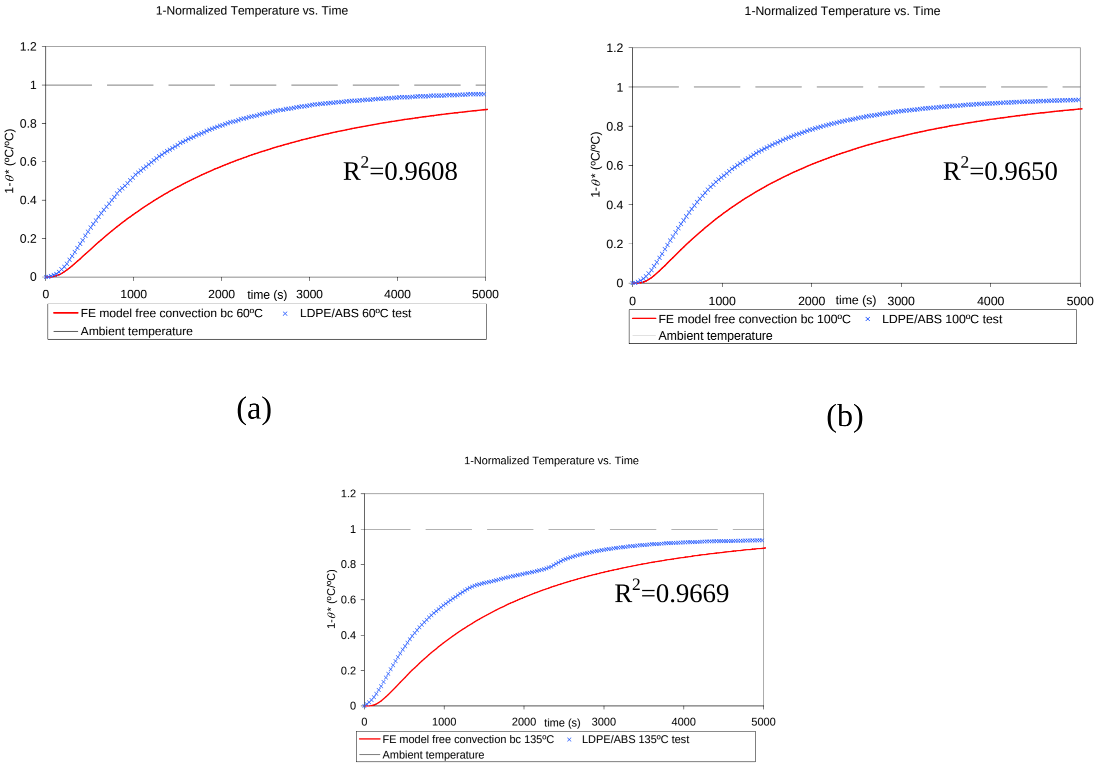

(a)

(b)

(c)

Figure 18 - Results of initial finite element simulations: (a) 60ºC case, (b) 100ºC case, and (c) 135ºC case

From the plots it is evident that the initial finite element model was not able to sufficiently represent the behavior of the experimental conditions. The response in all three cases is much slower, indicating that perhaps the approximation of the structural geometry is inaccurate or the free convective boundary condition is inappropriate for the oven.

To try to correct for this error the boundary conditions were changed to convection boundary conditions with a constant heat transfer coefficient of h = 12 W/m^2-K as was discovered to give excellent results for the homogeneous analytical solution and also with radial ROM homogenized analytical solution. The revised model simulation results are shown in Figure 19.

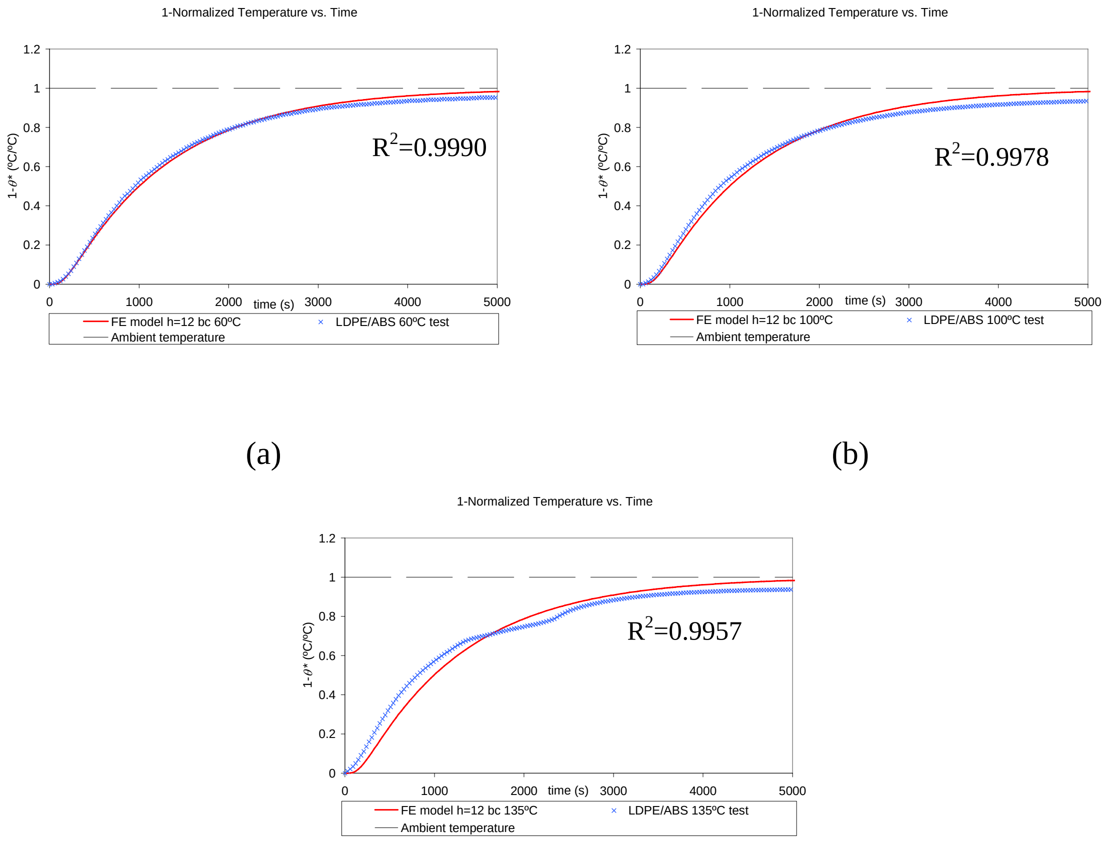

(a) (b)

(c)

Figure 19 - Finite element results with h = 12 W/m^2-K boundary condition: (a) 60º case, (b) 100ºC case, and (c) 135ºC case

Even with the adjustment of the boundary conditions, the finite element model still does not give as good of a correlation with the experimental data as the exponential fit formula. This is not to say, however, that this model is not a good representation of the thermal response, especially at the two lower test temperatures. Since there was still room for some improvement of the finite element model and the model is quite simple to modify, it was modified again to try to obtain even better results.

Since the radial ROM model proved to give accurate results when used as input parameters to the analytical solution, it was decided to use the same radial ROM parameters as inputs to the finite element model. The same convective boundary condition was used as in the previous simulation; the only differences were that the density, thermal conductivity, and specific heat values used for both layers of the sphere were the ones listed in the bottom row of Table 15. The results of the finite element simulation with the homogenized input parameters are shown in Figure 20.

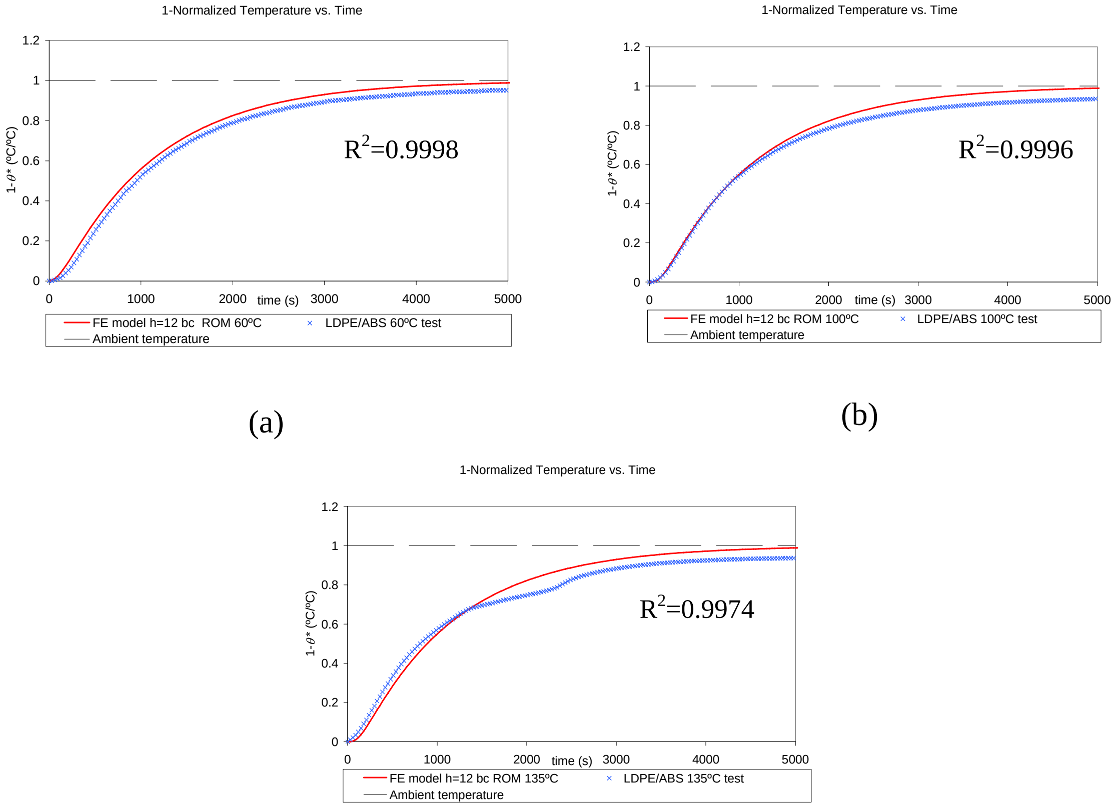

(a)

(b)

(c)

Figure 20 - Homogenized finite element results with h = 12 W/m^2-K boundary condition: (a) 60º case, (b) 100ºC case, and (c) 135ºC case

As can be seen from the values of Pearson's coefficient in the plots, the homogenized finite element model gives results that correlate even better to the experimental data than the finite element model with two concentric spheres with different sets of properties. This finite element model may be extremely beneficial for design requirements that call for maintaining the core of the module below a certain value because the results for the 60ºC and 100ºC simulations give the appropriate curve, but give slightly higher temperature predictions throughout the entire run.

The one thing that has been left out of the discussion for the finite element modeling up until now is the notion of temperature dependent properties. It is entirely possible to make the elements have properties that change depending upon their temperature. It is also conceivable to incorporate a phase change into the model, so that the finite element model truly and completely represents the complex polymer behavior observed during the higher temperature experiments. With this in mind, the finite element model was modified once more to include temperature dependent thermal conductivity as well as a phase change.

The literature was reviewed for potential polymer thermal conductivity temperature dependence functions. One reference, [Daws05], observed a sharp drop in polymer thermal conductivity with increased temperature, which was on the order of a 20-30 percent. Since for the 60ºC simulation, the finite element model agrees well with the experimental data but the 100ºC simulation starts to show signs of inaccuracies, it was decided to incorporate a 30 percent drop in thermal conductivity above 60ºC, from 0.33 to 0.27 W/m-K. The phase change temperature was chosen as 110ºC, taken straight from the data. The specific heat and density were held constant, the same as the in the previous simulation, even after the phase change. A value for the latent heat of fusion of 1×10^4 J/kg was input, based on some trial and error. It should be noted that only the inner part of the mesh representing the LDPE part of the module was given the temperature dependent parameters necessary to experience the phase change conditions. The results of the finite element simulation with the temperature dependent properties are shown in Figure 21.

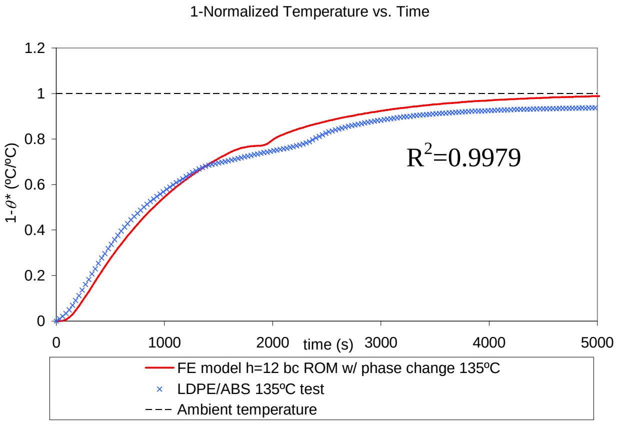

Figure 21 - Response for finite element model with added phase change and temperature dependence for 135ºC case

This temperature dependent model with phase change does show the response of the temperature increase begin to slow down with respect to time and then speed back up again as is seen in the experimental data. However, since the multi-material module exhibits such complex behavior above 100ºC, even this model is unable to obtain as good data correlation as the two lower temperature cases.

3.6 Conclusions and Contributions

In this chapter, experiments were conducted to obtain data for analyzing the effect of the MMIM process on the steady-state thermal conductivity of polymer systems. Contributions in the form of characterization of the steady-state thermal conductivity across the multi-material interface in a module in addition to the proposal of a correction term that can be applied to the standard ROM model for multi-material configurations were made. The characterization effort determined that the effect of adhesion plays the largest role in predicting the performance of a MMIM system. Poor adhesion gives the best overall performance, followed by good adhesion, and the worst performer is a multi-material system produced without using MMM technology with no adhesion.

A set of transient thermal experiments was also conducted, aimed at determining the effect of increased ambient temperatures on homogeneous and heterogeneous injection molded polymer systems. The results were analyzed and contributions were made in the form of homogenized analytical models, an exponential fit formula, and a finite element model. The analytical models and the exponential fit formula are able to predict the response of single material and multi-material polymer systems quite accurately for ambient temperatures under the melting temperature. Above the melting temperature, the finite element model is the only model that captures the behavior observed during the phase change of the polymer. All of the models have extremely high correlation with the experimental data. These high correlation values of the models show that it is possible to develop more complicated design scenarios for MMM modules and still completely capture the physics of the problem using similar methods.

Chapter 4: Thermomechanical Behavior of Multi-Material Modules with Embedded Electronics

4.1 Introduction

There are obvious necessities for understanding the thermomechanical behavior of multi-material modules with embedded electronic components in the fabrication stage of the life cycle in addition to the operational stage of the life cycle. In the fabrication stage, it must be known how the polymer melt interacts with the embedded electronic components during cooling so that appropriate models can be developed regarding the shrinkage so that these principles may be extended to future design applications. It must also be known how the multi-material module performs when the embedded electronics are generating heat internally and dissipating it through the thickness of the surrounding polymer.

In order to address these issues, the following sections describe tests that were carried out to determine the displacement and strain fields of the multi-material polymer melt while cooling in the mold. Also discussed in this chapter are experiments performed to ascertain the displacement and strain fields of multi-material modules with embedded electronic components to characterize the effects of internal heat generation. The development of appropriate thermomechanical finite element models to reproduce the observed behavior so that future designs incorporating MMIM and embedded electronic components can be improved is also discussed for each of the cases.

4.2 In-Mold Cooling Experimental Setup

The strains associated with a homogeneous polymer and multi-material configuration cooling around an embedded component must be characterized so that appropriate models can be developed. Models can be helpful in determining how much shrinkage is expected for a particular processing temperature and mold friction condition, which is important in many applications, specifically tight tolerance designs.

An experiment was devised to observe the behavior of a multi-material polymer melt as it cools around an embedded component. The representative mold was selected to be a 100 millimeter diameter glass Petri dish. Although glass is not a typical mold material, it does have similar frictional characteristics as smoothly polished metal, which is of prime importance in this study. Glass also serves as a better insulator, which slows down the cooling process so that it can be observed over a longer period of time. The coefficient of thermal expansion (CTE) of glass is also lesser in magnitude than common mold materials, which helps minimize the error in the data caused by the thermomechanical behavior of the mold.

As a means of observing the effects that frictional properties of molds have on the thermomechanical behavior of a cooling polymer, two cases of different friction magnitudes are analyzed, one with low friction where a silicone mold release agent was liberally applied to the surface of the mold, and one with high friction where no mold release was used in preparation of the mold. The specific mold release agent used is Huron Technologies, Inc. RC 6310 High Performance Silicone Mold Release and General Purpose Lubricant. Two different polymer configurations were also tested to determine the contribution of a heterogeneous distribution compared to a homogeneous one. The heterogeneous distribution contained an inner layer of LDPE surrounded by an outer layer of ABS, whereas the homogeneous case contained only LDPE. In all, six cases were tested as described in Table 17, viscoelastic effects were neglected.

Table 17 - Description of test cases for in-mold cooling observations

Case #	Embedded Component	Friction	Material Distribution
1	No	Low	Homogeneous
2	No	High	Homogeneous
3	Yes	Low	Homogeneous
4	Yes	High	Homogeneous
5	Yes	Low	Heterogeneous
6	Yes	High	Heterogeneous

For each of the homogeneous cases, LDPE polymer granules were heated up in-mold using a hot plate until fully melted and then allowed to cool by natural convection. A thermocouple was embedded in the mold at the perimeter and connected to a laptop computer via an Omega HH560R digital thermometer to record the temperature of the polymer. For the heterogeneous cases, it was necessary to first heat the ABS in-mold using a furnace set to 260ºC, and then transfer the mold quickly to the hot plate where the LDPE was added and heated to its melting temperature. Although these steps are not the same as would be case for an actual multi-material process, they were necessary steps to prevent burning the LDPE as would be the case if the ABS was melted while the LDPE was in the mold. This requires the assumption that the interactions between the LDPE and ABS are not dependent on the order in which they are molded.

Just prior to cooling, a speckle pattern was applied to each of the polymer melts so that the digital image correlation (DIC) technique could be used to recover the displacement fields and calculate the strain fields during cooling. The DIC technique compares images to a reference image and uses a pattern recognition-based mathematical correlation algorithm to obtain full-field displacements with sub-pixel resolution [Bruc04, Bruc89, Chen05]. It has been shown by [Helm96, Luo93] that the DIC technique can be used to measure deformations in up to three dimensions if so desired. A 1.3 megapixel Qimaging Retiga 1300 camera with a Micro-Nikkor 105 millimeter lens captured the digital images with a magnification of approximately 15.3 pixels per millimeter, with an 8-bit grayscale format. The complete setup is shown in Figure 22 and an example image from the experiment is shown in Figure 23.

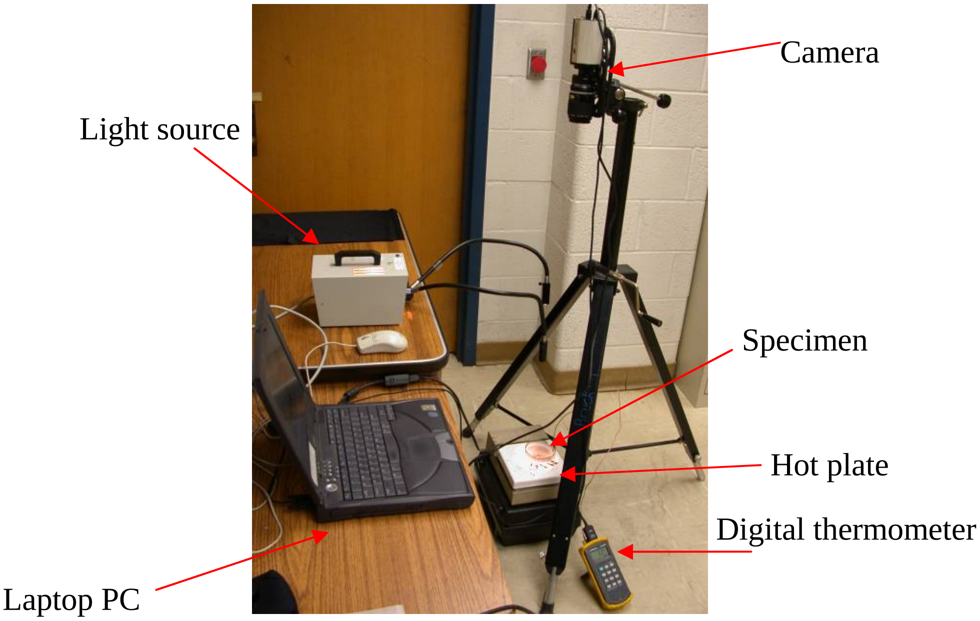

Figure 22 - In-mold cooling experiment setup

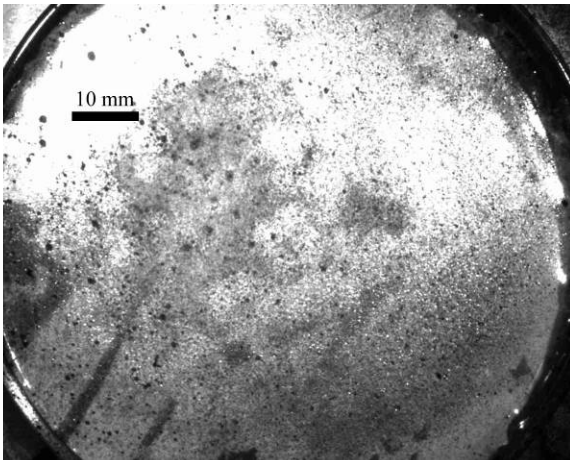

Figure 23 - Example image from in-mold cooling experiments

The DIC software in use is Correlated Solutions, Inc. VIC-2D, version 4.4.2. An area of interest is selected in the reference image, as well as a seed point. For each of the deformed images loaded, an initial guess of the locations of three points in the region of the seed point must be input as a starting point for the correlation algorithm. Each of the deformed images is compared to a reference image using a cubic B-spline interpolation on 101 pixel square subset sizes with a step size of 5 pixels. The results of the correlation calculation are the *x* and *y* components of the displacement vectors, the *u* displacement and *v* displacement respectively, at the step locations of the selected area of interest. From the displacement fields, the normal strain fields, in the *x* direction (shown as *exx*), referred to as the horizontal strain, in the *y* direction (shown as *eyy*) referred to as the vertical strain, and the shear strain (shown as *exy*) are calculated using 15 pixel square areas over the entire area of interest. All of the displacement and strain fields can be viewed using full-field color contour plots. In some cases, preliminary calculations of the displacement and resulting strain fields contained erroneous regions because of the areas of the images that reflect too much light, not enough light, or have poor quality speckle patterns. These regions were removed from the area of interest and the correlation calculation was completed again. Because of the circular geometry of the specimens, it is assumed that the response is fairly symmetric and these regions are similar to other corresponding regions.

4.3 In-Mold Cooling Experiment Results

For each of the cases described in Table 17, approximately 43 images were captured during the cooling experiments. After heating, the first images were captured at a high frequency, one every thirty seconds, and gradually taking fewer and fewer images as the temperature change slowed down as shown in the typical polymer temperature test curve in Figure 24. In most cases the change in temperature between images was somewhere between 2ºC and 4ºC until approximately 70ºC was reached where the change in temperature was between 5ºC and 8º. The results of each of the cases are discussed in detail in the following sections.

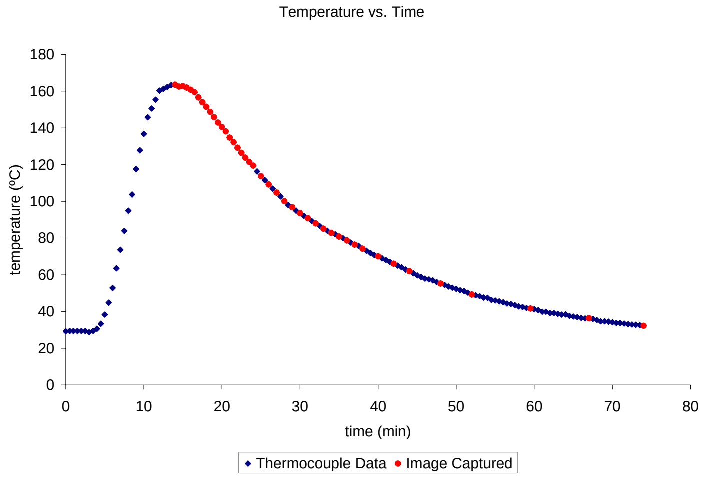

Figure 24 - Typical polymer temperature curve for in-mold cooling experiments

4.3.1 Case 1: Homogeneous Material Distribution with Low Friction

The DIC data for the first case shows how the homogeneous material shrinks in the mold due to cooling during processing when mold release has been applied to the mold, resulting in low friction conditions. The contour plots in Figure 25 show the time history of the horizontal, vertical, and shear strains during the cooling process.

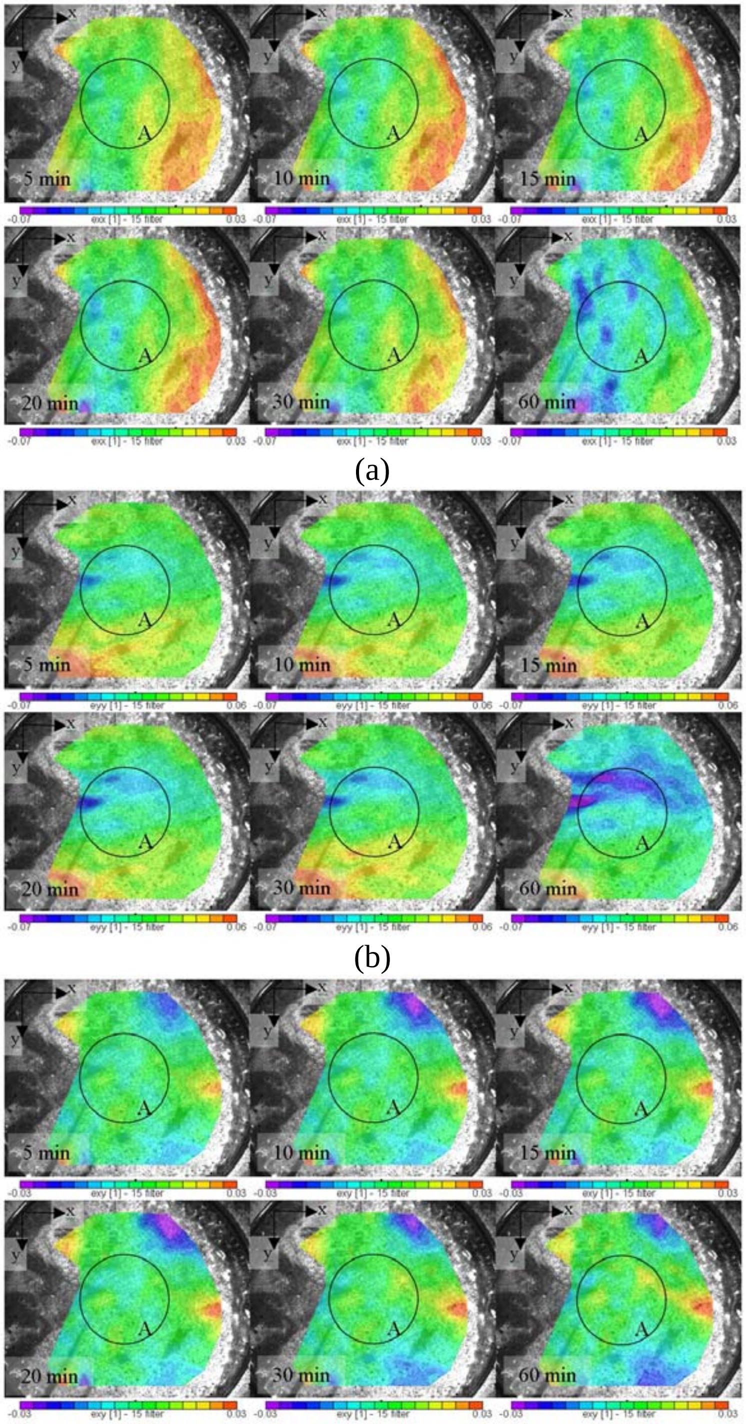

(a)

(b)

(c)

Figure 25 - Contour plots of strains with increasing time for case 1: (a) horizontal normal strain, (b) vertical normal strain, and (c) shear strain

As can be seen in each of the normal strain plots, there are variations in magnitude throughout the fields indicating that some regions are able to move more freely than other regions. This can be attributed to non-uniform temperatures, non-uniform application of the mold release, or even interactions with the sides of the mold. Initially, in some areas the normal strains are positive and in other areas, the normal strains are negative, ultimately resulting in the overall trend of negative normal strain, or shrinkage. The shear strain plot indicates that there are some small rotations occurring in the melt as the polymer solidifies, but the magnitudes of these rotations are small over much of the field suggesting that there is not much overall rotation of the polymer melt upon solidification. The higher magnitude rotations are near the edges of the specimen, where interactions with the sides of the mold are the most reasonable assumption for the cause for these shear strains.

The particular version of VIC-2D in use allows the user to probe the contour plots for data using “Inspector Tools.” These probes can be point probes, line probes, or circular area probes. The circular area probes allow the user to pick a region on the image and the average values of displacement and strain components in that region can be extracted for all of the deformed images. This allows the data to be displayed in the form of a line plot which reduces the number of figures to present and is easier to understand than a series of contour maps for the deformed images.

The center of the image was selected and a circular area with diameter of 460 pixels, approximately one-third of the image the diameter of the mold, was drawn as is shown by the circular area labeled ‘A’ in the contour plots in Figure 25. The average value within the circular region for all of the deformed image strain contour plots was extracted. The data was exported as a comma separated variable file so that it could be opened with Microsoft Excel. This gives the ability to combine the strain data with the thermocouple data for easier observation of the thermomechanical response. This data for case 1 is presented in Figure 26.

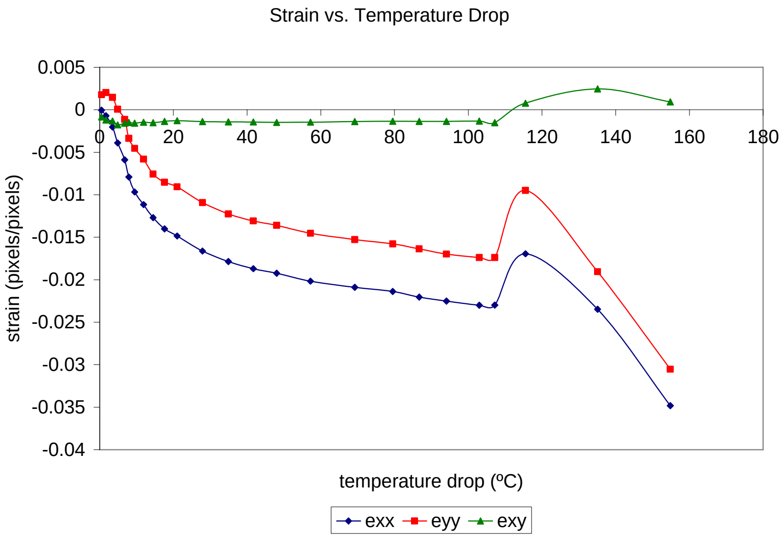

Figure 26 - Plot of strain in central region as a function of temperature drop for case 1

The beginning trends for the normal strains are the same, both decreasing with decreasing temperature to the point where they are almost constant, near 2 percent normal strain, with the magnitude of the horizontal strain being slightly higher than the magnitude of the vertical strain. The shear strain is much less in magnitude than the normal strains, and is approximately constant for much of the cooling period. At a temperature drop of approximately 107ºC, which corresponds to an actual temperature of 97ºC according to the thermocouple data, there is a sharp increase, roughly a 35 percent increase decrease in magnitude of the normal strains. This jump in the curves indicates a sort of relaxation of the polymer chains as the polymer changes phase and solidifies, resulting in lower magnitude normal strains and opposite sign shear strain. As the specimen continues to cool, the polymer bonds quickly retract again and continue to cause an overall shrinkage of the specimen and rotation back toward the original position. The final outcome of the data for the case of a homogeneous polymer with low friction conditions shows an overall shrinkage on the order of 3 to 3.5 percent strain.

After the sharp increases in strain, it should be noted that the decrease in strain with decreasing temperature in the solid phase can be approximated as linear. It is at this time that the polymer can be expected to have a thermomechanical response given by Equation (28), where α is the apparent CTE.

$$\varepsilon_t = \alpha \Delta T \tag{28}$$

The apparent CTE is different from the actual CTE because it is considered to be constant within the range of temperatures where it is evaluated and does not take into consideration the magnitudes of the temperatures, only the difference in temperature. The actual CTE value would be dependent on the actual temperature and may have non-linear behavior throughout the cooling process, and is very difficult to measure for polymer melts. Therefore, the average apparent CTE can be calculated for the polymer in the solid phase by taking the mean of the normal strains for the last two data points with the peak of the curves as the reference temperature. This calculation for this case of a homogeneous material with low friction results in an apparent CTE of approximately $490\text{x}10^{-6}\ ^{o}C^{-1}$.

4.3.2 Case 2: Homogeneous Material Distribution with High Friction

To determine the effect of friction on the thermomechanical behavior of a homogeneous polymer melt, the previous low friction case is compared to the high friction case presented here. It is expected that the frictional and adhesive forces that arise due to no mold release agent being present will constrain the deformation, resulting in less strain since the required forces developed in the polymer melt would have to overcome these frictional and adhesive forces. The DIC data for this case, shown in Figure 27, gives insight on how the homogeneous material shrinks in the mold due to cooling during processing when there is a large amount of friction, as would be the case if no mold release agent were applied to the mold.

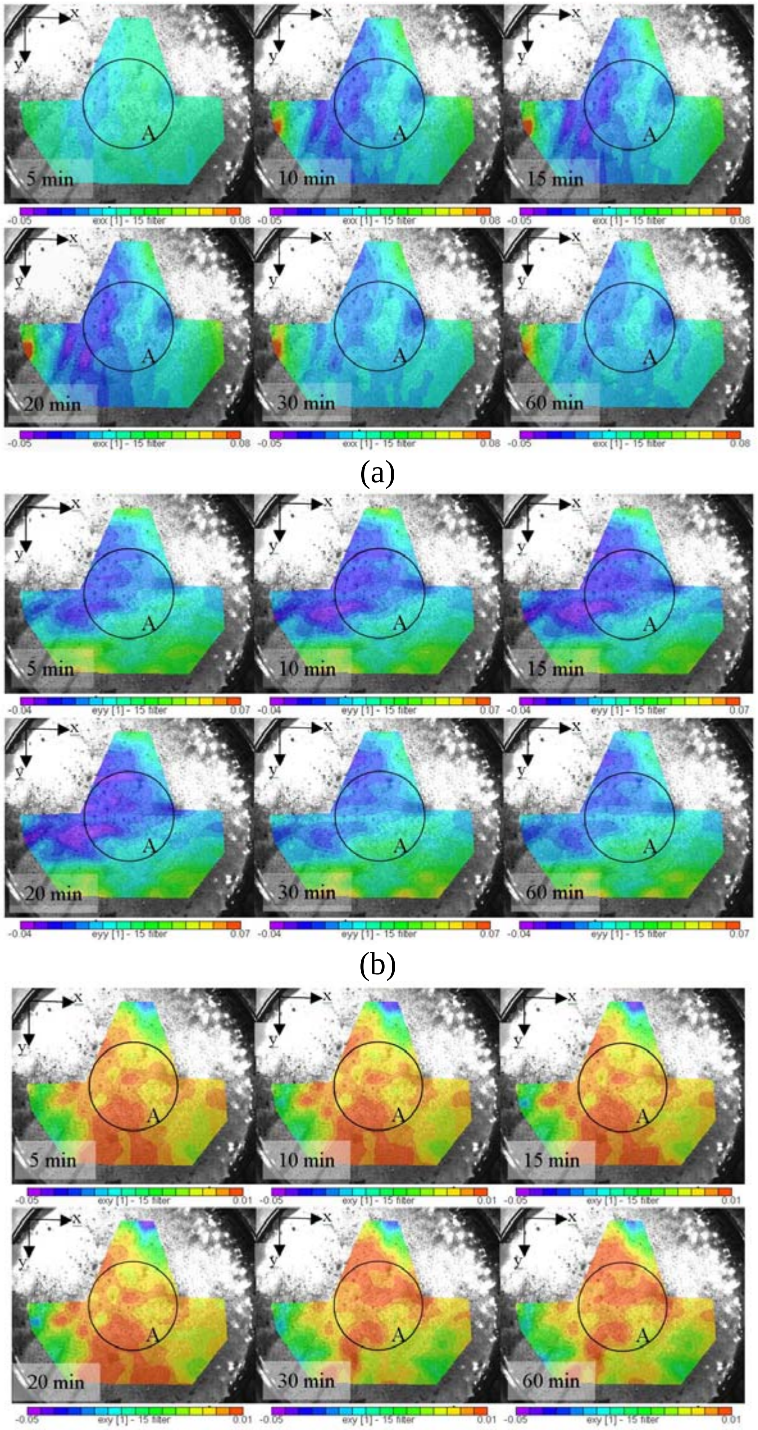

(a)

(b)

(c)

Figure 27 - Contour plots of strains with increasing time for case 2: (a) horizontal normal strain, (b) vertical normal strain, and (c) shear strain

The contour plots of the horizontal strain shows that in the central region of the mold, there is negative strain, or shrinkage, of different magnitudes throughout the specimen, with the left side of the specimen experiencing slightly higher magnitudes of shrinkage. The effect of shrinkage is also observed for the vertical strain, where the upper left portion of the contour plot indicates that there is more shrinkage in that region than in the lower regions. The shear strain, along with the variations in horizontal and vertical strain fields, indicate that there is a small amount of rotation involved in the motion of the polymer melt as it contracts, even in different directions in neighboring regions, which was also observed for the low friction case.

In a similar manner as was completed for the low friction case, the same circular region, shown by the area ‘A’ in Figure 27, was used to extract the average strain data so that it could be analyzed with the corresponding temperature data, as shown in Figure 28.

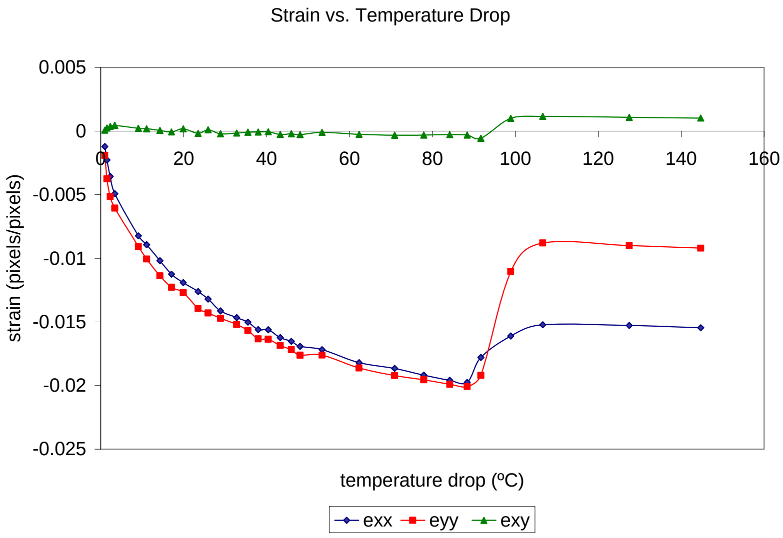

Figure 28 - Plot of strains in central region as a function of temperature drop for case 2

The strain plots in Figure 28 show that there is a definite decrease in strain in both the horizontal and vertical directions as a result of the cooling as was seen in the low friction case. At first the decrease in normal strain occurs at a fast rate, and then slows down to the point of almost being constant at a temperature drop of approximately 88ºC, where the magnitude of the normal strains is on the order of 2 percent strain. The magnitudes of both curves agree very well up to this point, indicating that the normal strains are symmetric. The point at which there are jumps in both graphs corresponds to the point at which the central region of the polymer melt begins to change phase and solidify, approximately 98ºC according to the thermocouple data. This temperature agrees with the temperature where the phase change began in the low friction case. In this high friction case, the change in strain due to the relaxation of the polymer chains is approximately 25 percent for the horizontal strain and near 40 percent for the vertical strains, but on the average the change in magnitude is close to what was seen in case 1. The final overall shrinkage for the case of the homogeneous polymer with high friction conditions is on the order of 1 to 1.5 percent.

The shear strain fluctuates up and down in a somewhat random pattern, but the overall trend is also a decrease as the temperature decreases after an initial jump, followed by a large jump that results in the shear strain doubling in magnitude and switching direction, from roughly -0.06 to 0.12 percent strain. Recall the change in rotation direction was also present in the low friction case.

In a similar manner as was completed for the low friction case, the apparent CTE was calculated in the linear portion of the strain curve. For this homogenous LDPE case with high friction conditions, the apparent CTE is calculated to be 62×10^{-6} $^{o}C^{-1}$. This is a remarkable difference in value from what was observed in the previous case; the friction causes a drop in the apparent CTE of approximately 87 percent. This information is essential to designers who are trying to design tight tolerance parts while accounting for the in-mold shrinkages.

4.3.3 Case 3: Homogeneous Material Distribution with Low Friction and Embedded Component

Since the focus of this thesis is geared toward embedding electronic components in molded modules, it was decided to embed a representative electronic component in the polymer to determine the effect of the component on the shrinkage of the polymer during cooling. The first case of embedded electronic components corresponds to case 1 presented earlier, low friction. The representative component was selected to be a large resistor, 24 millimeters long and 5.5 millimeters in diameter. The resistor was placed in the mold prior to melting the polymer but after the application of the mold release agent to better represent the actual conditions of embedding a component using a process such as injection molding. The time history of the cooling experiment is shown using the DIC contour plots in Figure 29.

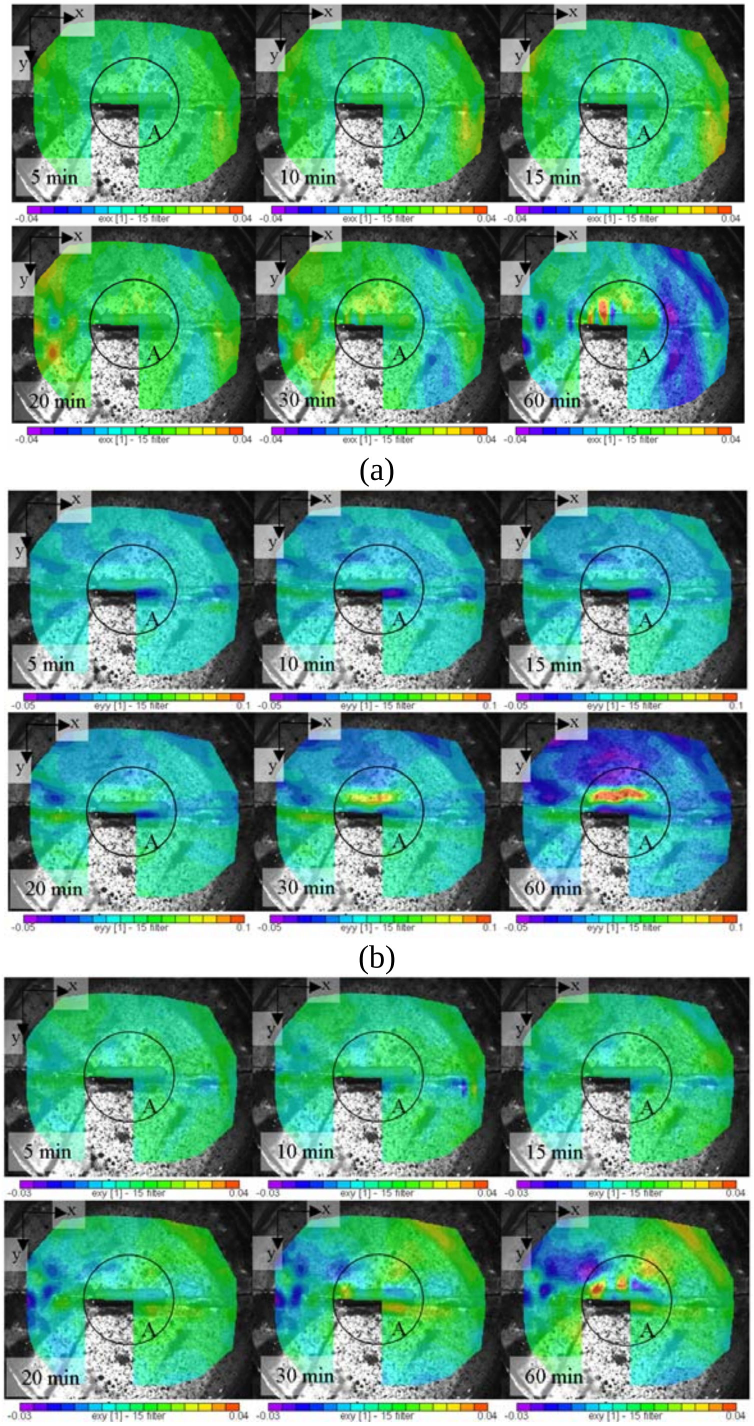

(a)

(b)

(c)

Figure 29 - Contour plots of strains with increasing time for case 3: (a) horizontal normal strains, (b) vertical normal strains, and (c) shear strains

The horizontal normal strain plots show that there is an effect on the axial strain field caused by the addition of the component. During the cooling experiment the strain is constant almost everywhere up until the last two images, where some large positive strains occur in areas near the component and the right hand side of the field shows a largely negative strain. Lower magnitudes of axial strains are observed globally than for case 1 where no component was embedded. The vertical normal strain plot also shows that there is an effect on the transverse strain caused by the addition of the component, but much less in magnitude than for the axial strain field in the vicinity of the component. Lower magnitudes of axial strain are also observed from a global perspective than for case 1. The shear strain plot also shows some sharp gradients, showing that there are rotations caused by the addition of the component.

In order to better determine the local response caused by the addition of the component, the same circular region labeled 'A' in Figure 29 was used to extract the strain data so that it could be associated with the corresponding thermocouple data. The results are shown in Figure 30. It should be noted that the resistor component has of a ceramic coating that prevents too much expansion, giving it a CTE of approximately $30 \times 10^{-6}\ {}^{o}C^{-1}$ according to the manufacturer. Since the resistor is in the central region, accounting for approximately 19 percent of the area, it is also included in the average strain results that are extracted and therefore affects the magnitude of the strain data reported in the plot.

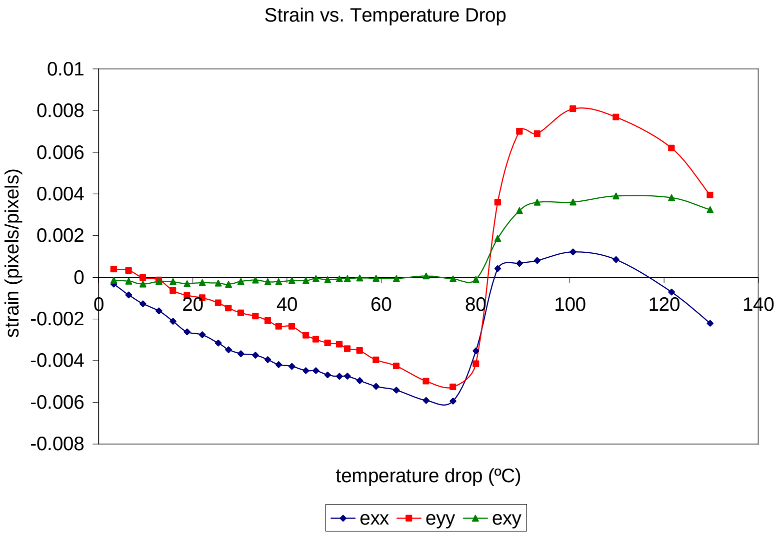

Figure 30 - Plot of strains in central region as a function of temperature drop for case 3

The axial and transverse strains in the central region have similar response to the previous low friction case, showing a decrease in strain with decreasing temperature as expected up until the temperature at which the curves have a steep jump. The decrease is more linear than observed for the previous cases, for both the axial and transverse strains. The shear strain appears to not be affected too much by the addition of the component, as the results are similar to the previous cases.

The large change in strain experienced by the polymer as it changes phase is severely affected by the addition of the embedded component. It is expected for the previous cases to see a decrease in normal strain magnitude by approximately 35 percent, however, in this case the axial normal strain increases in value by over 106 percent and the transverse normal strain increases in value by roughly 220 percent. After the drastic change in strain, the normal strains decrease in a similar manner as seen for the case without an embedded component. The final result is shrinkage on the order of 0.2 percent strain in the axial direction, but a larger expansion of 0.4 percent strain in the transverse direction.

4.3.4 Case 4: Homogeneous Material Distribution with High Friction and Embedded Component

This case corresponds to case 2, homogeneous polymer without mold release, except for the addition of an embedded component. The component is the same type of resistor used in case 3. The time history of the cooling experiment is shown using the DIC contour plots in Figure 31. Unfortunately, half of the sample area was unable to be correlated and had to be removed from the area of interest for the DIC calculations. However, this case is only necessary to verify what can already be deduced from the previous cases.

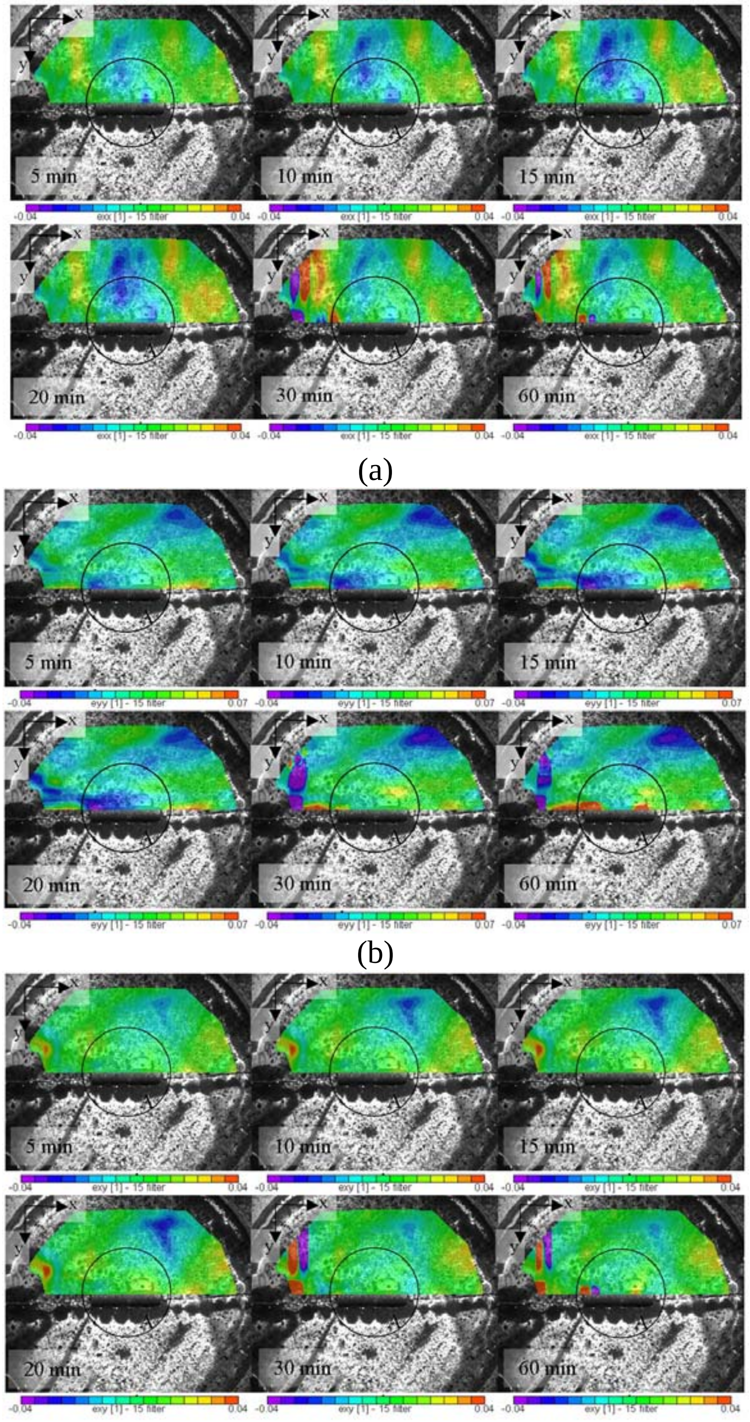

(a)

(b)

(c)

Figure 31 - Contour plots of strains with increasing time for case 4: (a) horizontal normal strain, (b) vertical normal strain, (c) shear strain

As can be seen from the time history contour plots of the axial strain, the addition of the component as well as the lack of mold release agent causing friction constrain the motion of the polymer. There are some areas of expansion observed, but overall the global response of the specimen is to experience a small amount of strain shrinkage. Alternatively, the transverse strain time history plots show large regions of negative strain near the component initially, followed by those same regions experiencing positive strain. The shear strain plot shows many similarities to the axial normal strain plot, resulting in very little strain throughout the field.

Again the same circular area was used to plot the strain data against the thermocouple data as shown in Figure 32. It should be noted that even though only half the circular area is used for the data extraction in this particular case, if it is assumed that the response is symmetric, then the plot captures the essence of the strains during the cooling process.

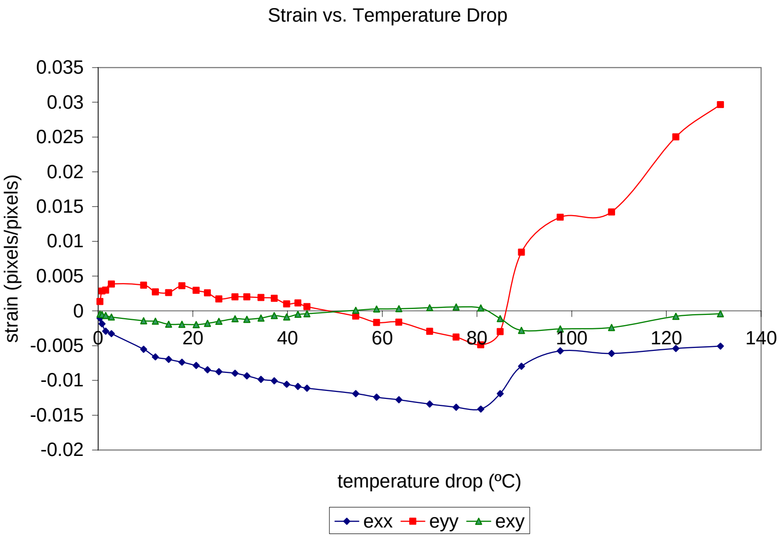

Figure 32 - Plot of strain in upper part of central region as a function of temperature drop for case 4

In the plot it is observed that the normal strains decrease with temperature in a linear fashion as was seen in the embedded component case with low friction. This plot does contain the unexpected result of the transverse strain starting out positive and decreasing up until the sharp change in strain. In this case, the change in magnitude of axial strain caused by the polymer changing phase is approximately a 57 percent increase and the change in magnitude of the transverse strain is on the order of a 360 percent increase. After the polymer solidifies, the axial strain is slightly increasing but the transverse strain increases drastically. He overall effect of the cooling process causes an axial shrinkage 0.5 percent strain and a transverse expansion of 3 percent strain in the central region. The shear strain remains somewhat constant near zero throughout the cooling process.

4.3.5 Case 5: Heterogeneous Material Distribution with Low Friction and Embedded Component

This case is the counterpart of case 3, where a mold release agent is applied to the mold prior to embedding the component; however, here two materials are used to represent a multi-material module. As discussed in the beginning of Section 4.2, the ABS was heated first in a furnace, prior to the addition of the LDPE granules to prevent burning. It can be seen in the images that the ABS granules do not flow into each other as the LDPE granules do. This results in the ABS granules retaining their shape, even though they were heated above the melting temperature and were very compliant. Figure 33 shows the DIC results of the strain fields at different times during cooling.

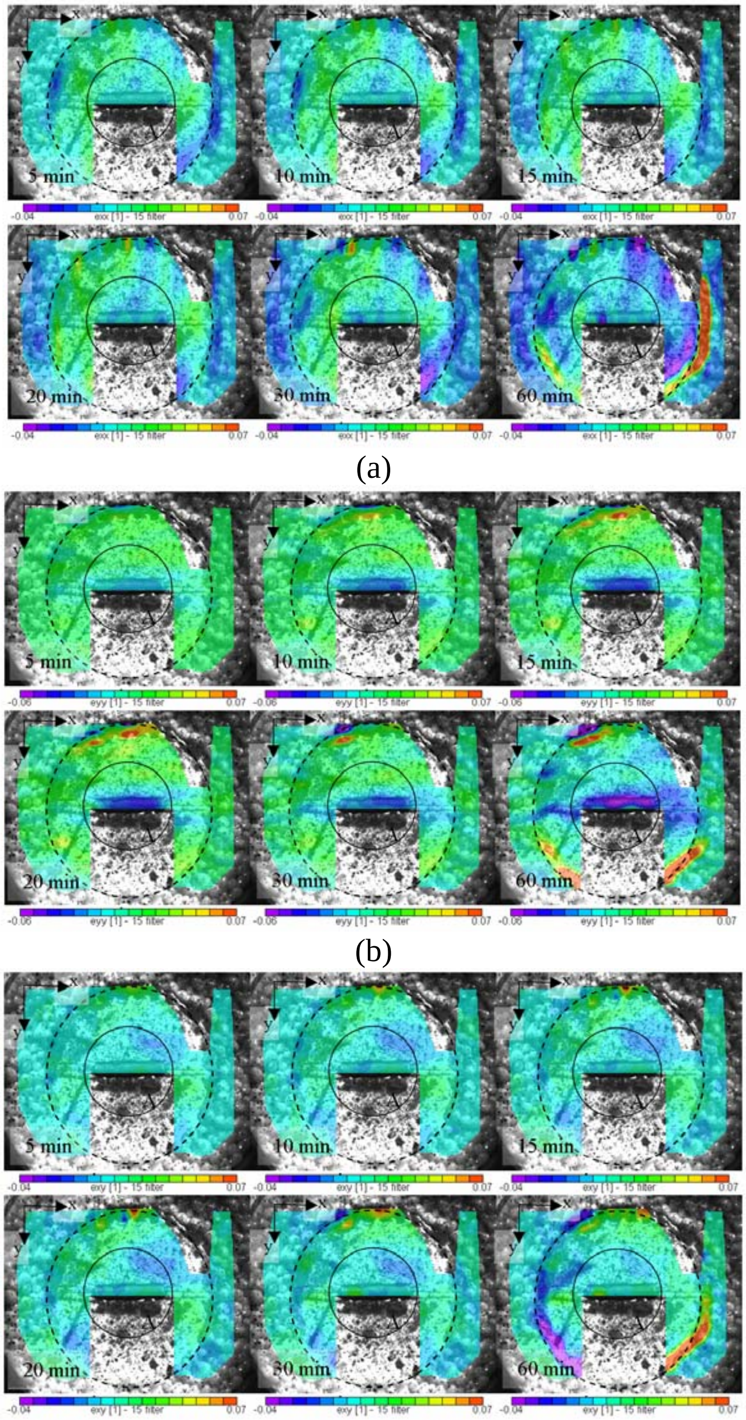

(a)

(b)

(c)

Figure 33 - Contour plots of strains with increasing time for case 5: (a) horizontal normal strains, (b) vertical normal strains, and (c) shear strains

The contour plots show that, initially, negative horizontal normal strains develop everywhere in the field, but higher in magnitude in the interface region which is shown by the dotted line on the contour plots. As the specimen cools, the negative axial strains in the ABS region increase in magnitude quickly, while the LDPE increases in axial strain slightly more slowly. At the interface between the ABS and LDPE, the axial strains that develop late in the experiment are high in magnitude and positive, which has not yet been seen for the axial strain in the previous experiments. Since the interfacial effects caused by adding a second material cause large axial strains, the effects near the embedded component are practically negligible. This is not to say that the effect of the component being there can be ignored. The effect of the component geometry is evident by looking at the transverse strains plots.

The transverse strain plots show that there are large magnitude positive transverse strains at the interface as was seen for the axial strains. However, what is not seen in the transverse strain plots is the difference in strain in the ABS region compared to the LDPE region. Had there not been large strains at the interface, it would be possible to see a difference in the strain values in the different regions. It can also be seen that there are large negative transverse strains caused by the embedded component.

The shear strains are near zero throughout much of the field, in both the LDPE and ABS regions; however, at the interface the shear strains are high in magnitude indicating that there are rotations at the interface in addition to the largely positive normal strains.

In order to determine the response of the multi-material specimen with embedded component, the same circular area was extracted and compared to the appropriate thermocouple data. The results are shown in Figure 34. It should be noted that the temperature data was obtained at the edge of the mold, where ABS was the material in which it was embedded.

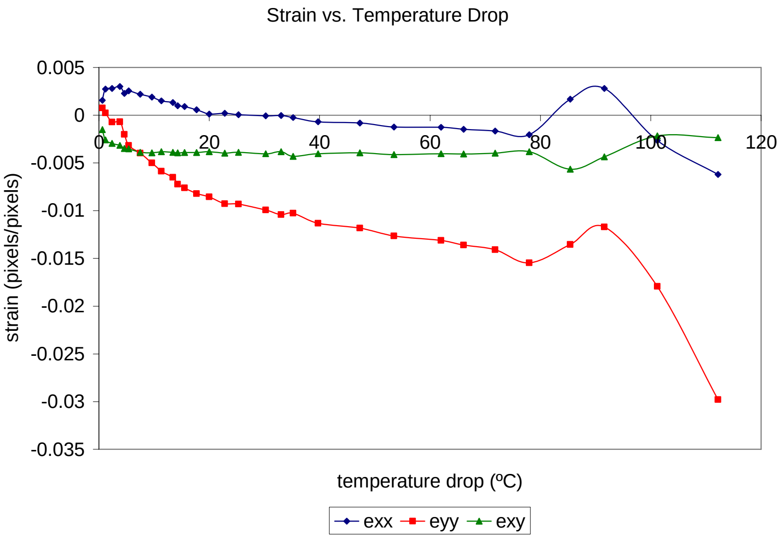

Figure 34 - Plot of strains in central region as a function of temperature drop for case 5

The plot shows the average axial strain starts positive in the central region and decreases linearly to the point where the sharp change in magnitude occurs. The sharp change in magnitude is on the order of 200 percent, which is followed by a sharp decrease in axial strain to a final strain near -0.5 percent strain. The average transverse strain is negative throughout the cooling process, experiencing a linear decrease in strain with decreasing temperature as was seen in the corresponding homogeneous case. The sharp change in strain that occurs as the central region changes phase is only on the order of roughly 30 percent, much less than the axial component. This is followed by a severe decrease in strain, approximately 170 percent to a final transverse shrinkage on the order of 3 percent strain. The average shear strain in the central region remains somewhat constant throughout the cooling process.

4.3.6 Case 6: Heterogeneous Material Distribution with High Friction and Embedded Component

The final cooling experiment to be discussed is the multi-material counterpart to case 4, where no mold release was used. The results of the DIC calculations are shown in the time history plots of the strains in Figure 35.

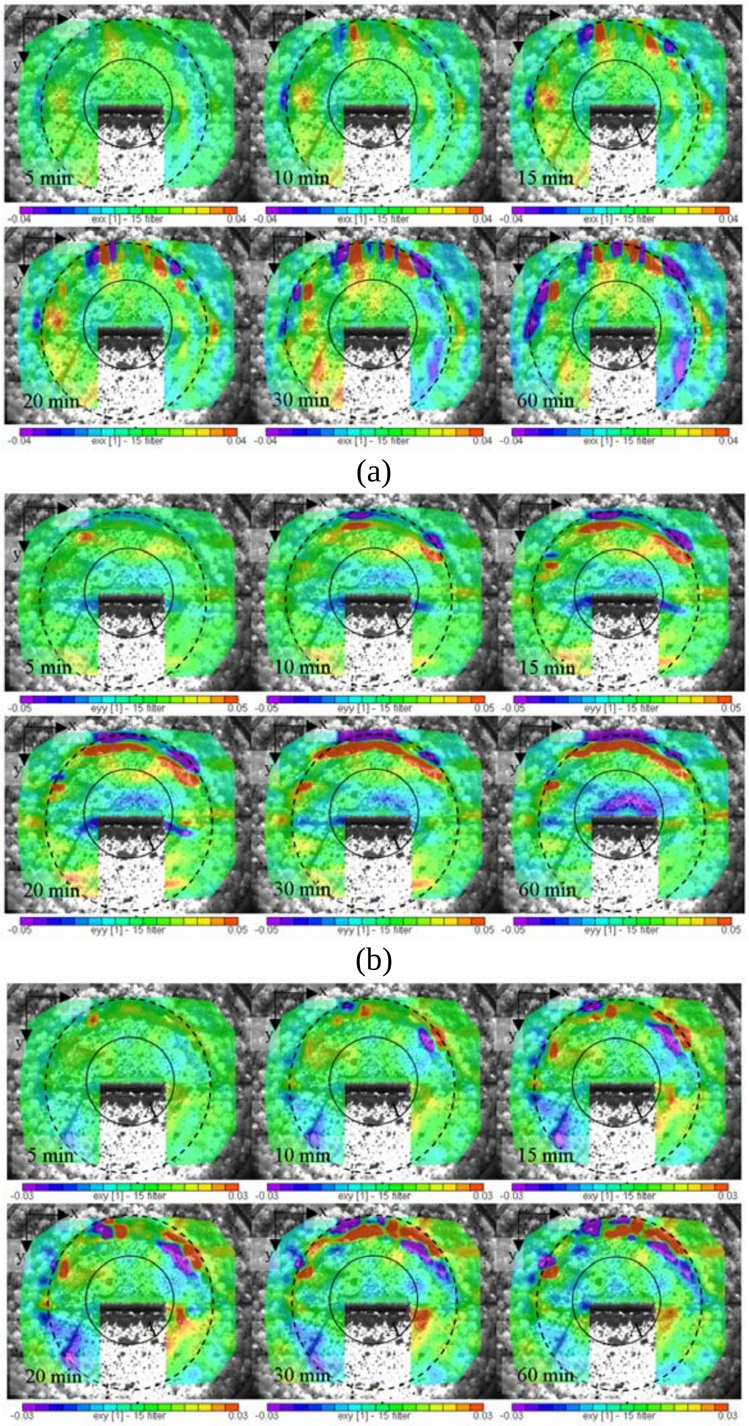

(a)

(b)

(c)

Figure 35 - Contour plots of strains with increasing time for case 6: (a) horizontal normal strains, (b) vertical normal strains, and (c) shear strains

The contour plots of the axial strain for this case agree with the plots for the previous multi-material case in the way that there is a difference in the magnitudes of the axial strain experienced in the different material regions, but both being negative. There are also regions of sharp gradients in strain at the interface between the materials. And it is also the case here that the effects of adding another material dominate the effects of the embedded component for the axial strains.

The transverse strains for this case also agree with the previous multi-material case. There are large magnitude strains at the interface, but the regions far enough away from the interface are essentially similar in magnitude for both materials. There is also a region of negative strain near the embedded component as was seen in the previous case.

The shear strain plots show that there are significant rotations occurring as time progresses and the polymers cool down. Most of the large magnitude rotations occur at the interface and near the embedded component as is expected.

The same data extraction in the central circular region was used in this case as was used for the previous cases; the results are shown in Figure 36.

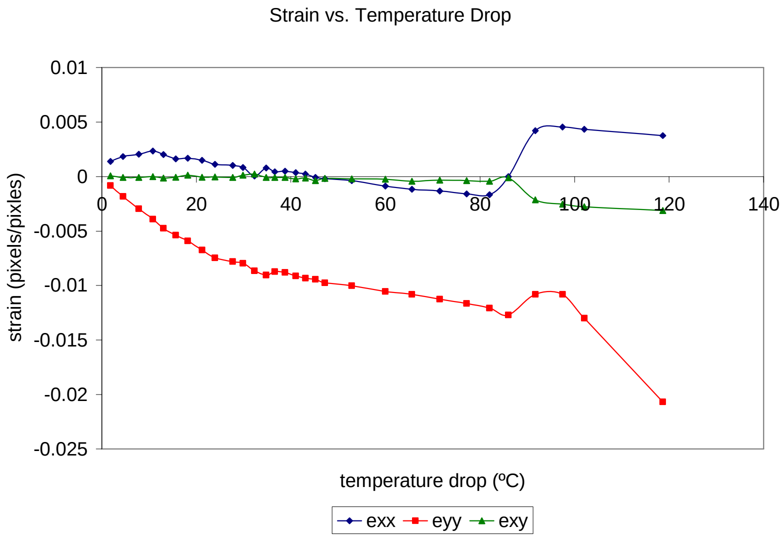

Figure 36 - Plot of strains in central region as a function of temperature drop for case 6

This plot is extremely similar to the corresponding plot in the previous section for the multi-material case with low friction. The axial strains experience an initial increase and slowly decrease until the sharp increase which in this case is more than a 200 percent change in magnitude. The final average axial strain in the central region is the main exception to the previous case; here the magnitude is similar but opposite in sign. The transverse strain experiences a similar response to cooling as the previous case as well, with the main difference being that the final strain is lower in magnitude here, on the order of 2 percent strain. From the results of the last two experiments, it can be concluded that effects of friction and embedding a component of a simple geometry are dominated by the effects of adding a second material.

4.4 Thermomechanical Finite Element Model for Cooling Experiments

A simple thermomechanical finite element model was developed to determine whether or not it is possible to accurately predict the thermomechanical response of multi-material modules when subjected to conditions such as those from the in-mold cooling experiments. As opposed to the modeling effort in Chapter 3, the software used in the following sections for the thermomechanical modeling is COSMOSWorks 2005, the analysis tool of the SolidWorks CAD software package. COSMOSWorks was chosen because it has many of the same features and capabilities as the I-DEAS package used in Chapter 3, but is easier to implement for thermomechanical simulations. The following sections discuss the development of the finite element model and its application to the different experimental cases.

4.4.1 Thermomechanical Finite Element Model for Case 1: Homogeneous Material Distribution with Low Friction

The experiments discussed in the previous section show complex behavior that is difficult to model, however a thermomechanical finite element model is developed from the results of the case 1 experiment that simplifies the conditions to something much more manageable and neglects plasticity. Since it is known that a static finite element analysis for a homogeneous material with only thermal loading will do nothing more than solve Equation (28), which depends on the difference between the applied temperature and the reference temperature in addition to the CTE of the material, and the temperatures of the experiment are already known, all that is left is to determine the apparent CTE that fits the data. It should be noted that the apparent CTE values discussed in the previous sections are valid for the linear end portion of the cooling curve, not as an approximation to the entire cooling curve, which is what is being done here.

The feat of determining the apparent CTE is not as simple as it may sound. First, it should be mentioned that although the focus of the previous section was on the strains, the focus must now be switched to displacements. This is because as Equation (28) implies, the strain is only based on the temperature and the resulting strain field for a given temperature is constant throughout the body unless the temperature varies. It is conceivable to input a temperature profile and solve the model to obtain the strain profile, however, the CTE would still need to be calculated in some manner in addition to the temperature field. The simpler route is the taken here, where the symmetry of the experimental setup is exploited along with Equation (29) to determine an average CTE for the entire field, where u_r is the radial displacement and r is the radial position.

$$u_r = \alpha \Delta T r \tag{29}$$

Since the data that VIC-2D output is in Cartesian coordinates with the origin at the upper left corner of the image, all of the data must be converted to Polar coordinates with the center of the image being the origin. This was accomplished by writing a MATLAB code that reads in the VIC-2D data and calculates the radial distance from the center of the image. Then Equation (29) was solved for α at every point in the field using the initial and final temperatures from the thermocouple data and the average value taken as the apparent CTE. In order to be able to compare the values of the displacements determined from the thermomechanical finite element model to the VIC-2D data, it was necessary to also scale the displacements to be in millimeters rather than the default pixel displacement values. The code also calculated an average around the center of the image and then subtracted this value from every point in the field to eliminate any rigid body motion experienced by the entire specimen because the thermomechanical finite element model would have zero displacement as is indicated by Equation (29) unless a displacement was specified as a boundary condition. Finally the code plotted the data as a contour plot in Cartesian coordinates for comparison to the model results.

For case 1, the homogeneous LDPE specimen with low friction, the apparent CTE was calculated to be $280\text{x}10^{-6}$ $^{\text{o}}\text{C}^{-1}$ for initial and final temperatures of 190.3ºC and 35.5ºC respectively. For easier comparison purposes, the solid model was drawn to be the same size as the average size of the field calculated by VIC-2D (r = 29 mm), which is obviously smaller than the actual experimental mold size of 50 millimeters. The data results and model results are shown in Figure 37, with the contour plot of the data being constrained to only show the same shape and location as the model. It is worth noting that the finite element program COSMOSWorks assigns a wider range of values to the color green than the MATLAB program does, making the results appear as though there is less correlation than there actually is.

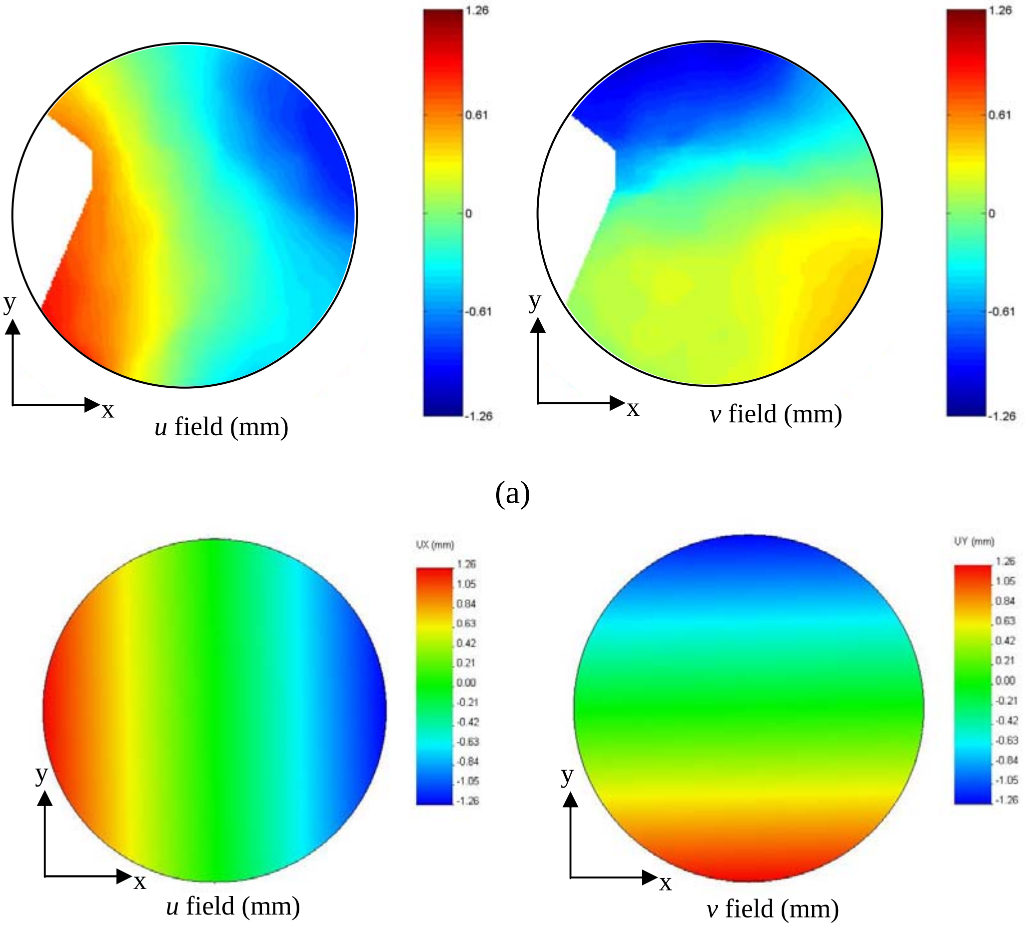

(a)

(b)

Figure 37 - (a) data and (b) FE model results for case 1

It can be seen by the figures that there is obviously some rotation in the actual experiment that is not captured by the finite element model. The model results show that the *u* field correlates quite well with the experiment, which was the intent. The *v* field does not correlate as well at the bottom of the field, but the top of the field represents the thermomechanical response of the homogeneous case accurately.

4.4.2 Thermomechanical Finite Element Model for Case 2: Homogeneous Material Distribution with High Friction

Although the data suggested that the apparent CTE decreases by 87 percent for the case where no mold release was used, as stated previously, those values do not apply to the temperatures being used here. Instead the apparent CTE for the case 2 data was calculated for the whole field and determined to be $90\text{x}10^{-6}$ $^{\circ}\text{C}^{-1}$, indicating a 68 percent decrease in apparent CTE value for the entire experiment when no mold release is present. Using this apparent CTE, and the initial and final temperatures of 177.8ºC and 33.1ºC respectively, the static analysis was completed and plotted with the data for the homogeneous LDPE with high friction case as shown in Figure 38.

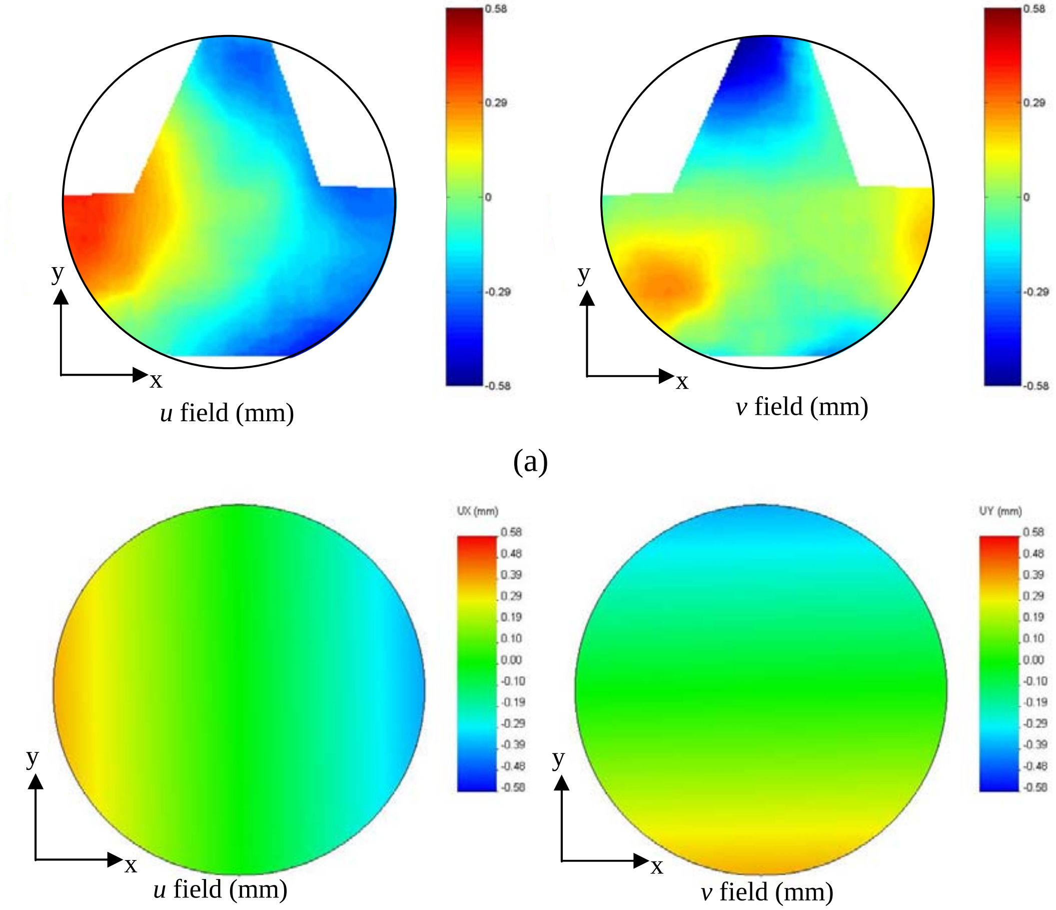

(a)

(b)

Figure 38 - (a) data and (b) FE model results for case 2

It can be seen by the contour plots that although the apparent CTE was calculated directly from the data, using that CTE in the finite element model ends up slightly underestimating the thermomechanical response in the form of the displacement field. Both the *u* field and *v* field calculated from the data contain a wider spectrum of values than the thermomechanical finite element model, however, considering the values along the perimeters rather than the colors of the circular areas show that the results are closer than they appear.

For comparison purposes, the values of the apparent CTE from both the *u* field and the *v* field for the low friction case and the high friction case were calculated at different times of the cooling experiments and correlated with the appropriate temperature data using the starting temperature as a reference, as is shown in Figure 39.

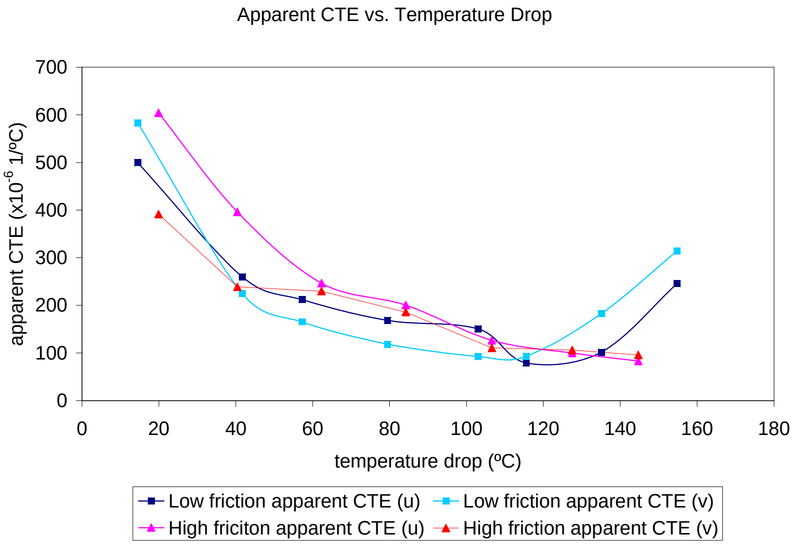

Figure 39 - Plot of apparent CTE vs. temperature drop for cases 1 and 2

It can be seen from the plot that throughout the cooling process, the general trend is a decrease in apparent CTE with temperature difference as is expected. It is non-linear, however this is expected after seeing the corresponding strain data for each of the cases. The decrease in apparent CTE is sharp in both cases at first, then the decrease is not quite as drastic as the polymers continue to cool. Although at first, the two curves from the high friction case (case 2) differ in initial values, they quickly approach each other and remain consistent for the latter portions of the experiments showing that there is a uniform shrinkage overall when there are high frictional forces present. Alternatively, the low friction case (case 1) maintains some difference in the values throughout the experiment, but the same behavior is observed for the apparent CTE calculated from the *u* and *v* fields where there is an initial decrease followed by an increase after the phase change. In both cases the increase in apparent CTE is on the order of over 200 percent. The final result agrees with what is expected, the low friction case has a much higher apparent CTE than the high friction case, as calculated from both the *u* and *v* fields.

4.4.3 Thermomechanical Finite Element Model for Case 3: Homogeneous Material Distribution and Embedded Component

Using the apparent CTE that was determined by calculation for the previous low friction case (case 1, $\alpha = 280\text{x}10^{-6}\ ^{o}\text{C}^{-1}$), the manufacturer supplied flexural modulus (E = 0.23 GPa), and a literature value for Poisson's ratio (ν = 0.35), the thermomechanical finite element model was applied to the conditions of case 3. This case included the embedded resistor which was drawn into the solid model and given the properties specified by the manufacturer. The cylindrical face of the resistor was assigned zero displacement boundary conditions to represent the experimental conditions where the resistor was epoxied to the mold. The initial and final temperatures used for the analysis were 161.3ºC and 31.5ºC respectively. The data and results are shown in Figure 40.

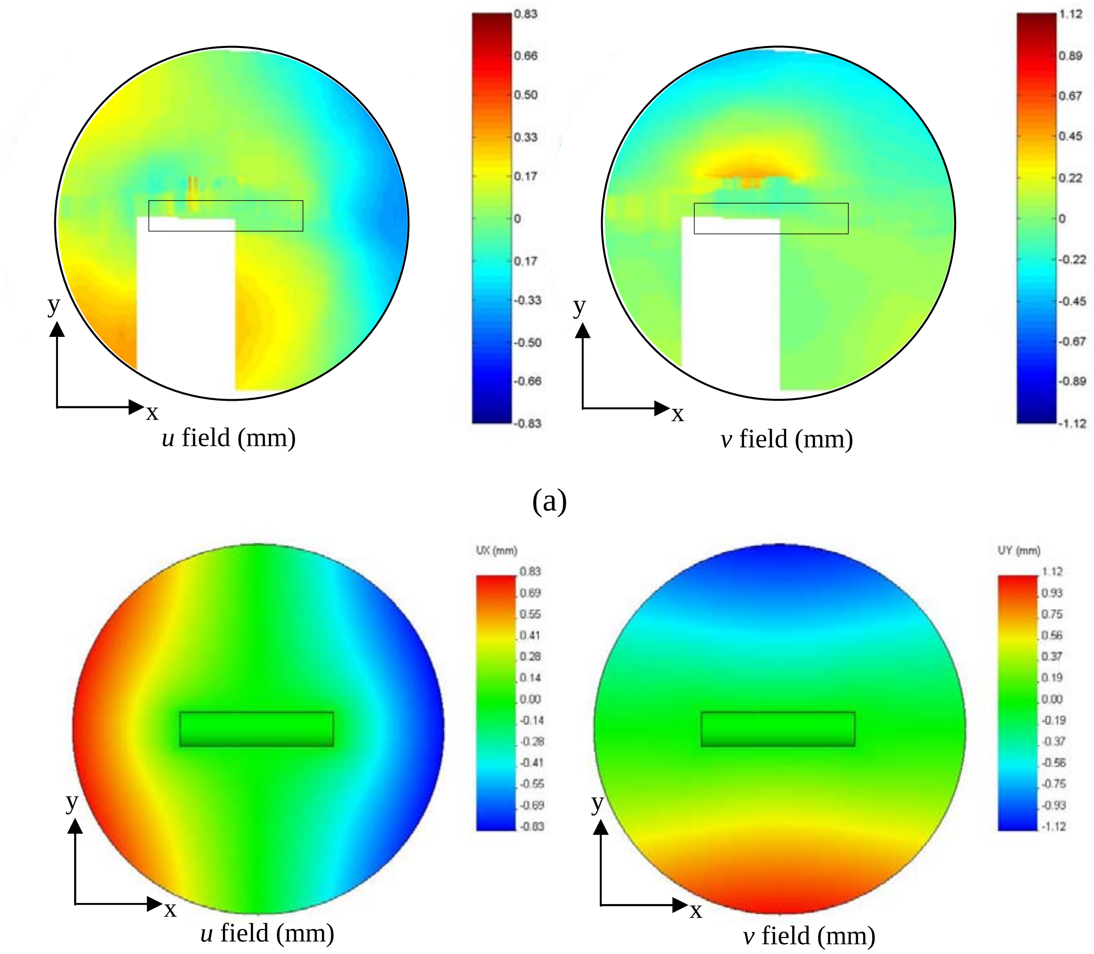

(a)

(b)

Figure 40 - (a) data and (b) FE model results for case 3

In this case the thermomechanical finite element model represents the data much better than was observed for case 2, which is good considering the goals of this research include embedding components in modules. In the previous case, the model underestimates the thermomechanical behavior, but here the model slightly overestimates the response which can be a good thing for design. Unfortunately, the subtle displacements of the polymer near the resistor are not captured by the finite element model, but at least the global response is captured within acceptable accuracy limits. The model also predicts the contours bending away from the embedded component in the *u* field and toward the component for the *v* field, however the experimental data actually shows the opposite effect.

4.4.4 Thermomechanical Finite Element Model for Case 4: Homogeneous Material Distribution with High Friction and Embedded Component

For the experimental case 4, which was the resistor embedded in homogeneous LDPE with no mold release, the apparent CTE used in the thermomechanical finite element model is the same apparent CTE calculated from the previous high friction case (case 2, $\alpha = 90\text{x}10^{-6}\ ^{\circ}\text{C}^{-1}$), the other material properties were left unchanged. The initial and final temperatures of the simulation were the same as those from the experiment, 163.6ºC and 32.2ºC respectively.

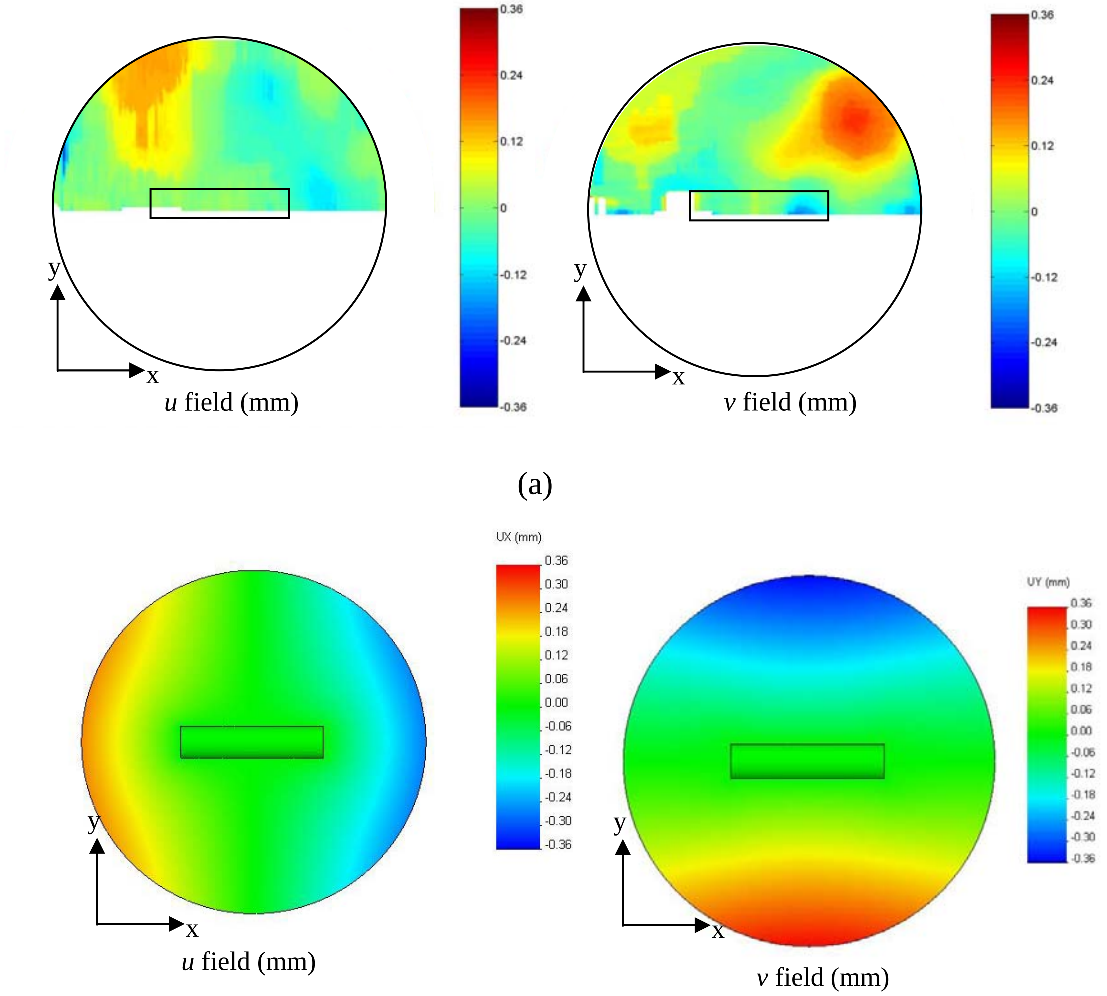

(a)

(b)

Figure 41 - (a) data and (b) FE model results for case 4

Unfortunately, there is only half of the field from the data to compare the model results with. However, by looking at the *v* field it can be seen that although the general response from the data does not match perfectly, the maximum and minimum values calculated by the model do correspond to the extreme values for the data. For the *u* field, some of the predicted response matches up nicely with the actual data whereas other areas do not match.

4.4.5 Thermomechanical Finite Element Model for Case 5: Heterogeneous Material Distribution with Low Friction and Embedded Component

For the multi-material cases, no data was obtained referring to the apparent CTE of the ABS in the experiments. Perhaps a calculation of the average CTE could have been made with the MATLAB code however, that would homogenize the response throughout the entire field of the model, which was not desired. Instead it was opted to use a value found on Matweb.com for general purpose ABS, α = 100x10^{-6} ºC^{-1}. Other relevant parameters for the ABS are the flexural modulus (E_{ABS} = 2.3 GPa) which was supplied by the manufacturer and Poisson's ratio (ν = 0.35) was taken from the literature. The dimensions of the solid model had to be modified to account for the different dimensions of the areas for each material, where the inner LDPE diameter was changed to r_i = 26.5 millimeters and the outer diameter for the ABS was set to r_o = 36 millimeters to correspond with the average size of the data field. The temperatures that were used in the calculation were 163.6ºC for the initial and 32.2ºC for the final temperature. The data and thermomechanical finite element model results are shown in Figure 42, where a dotted circle has been superimposed to show an approximate location of the interface between the LDPE and ABS.

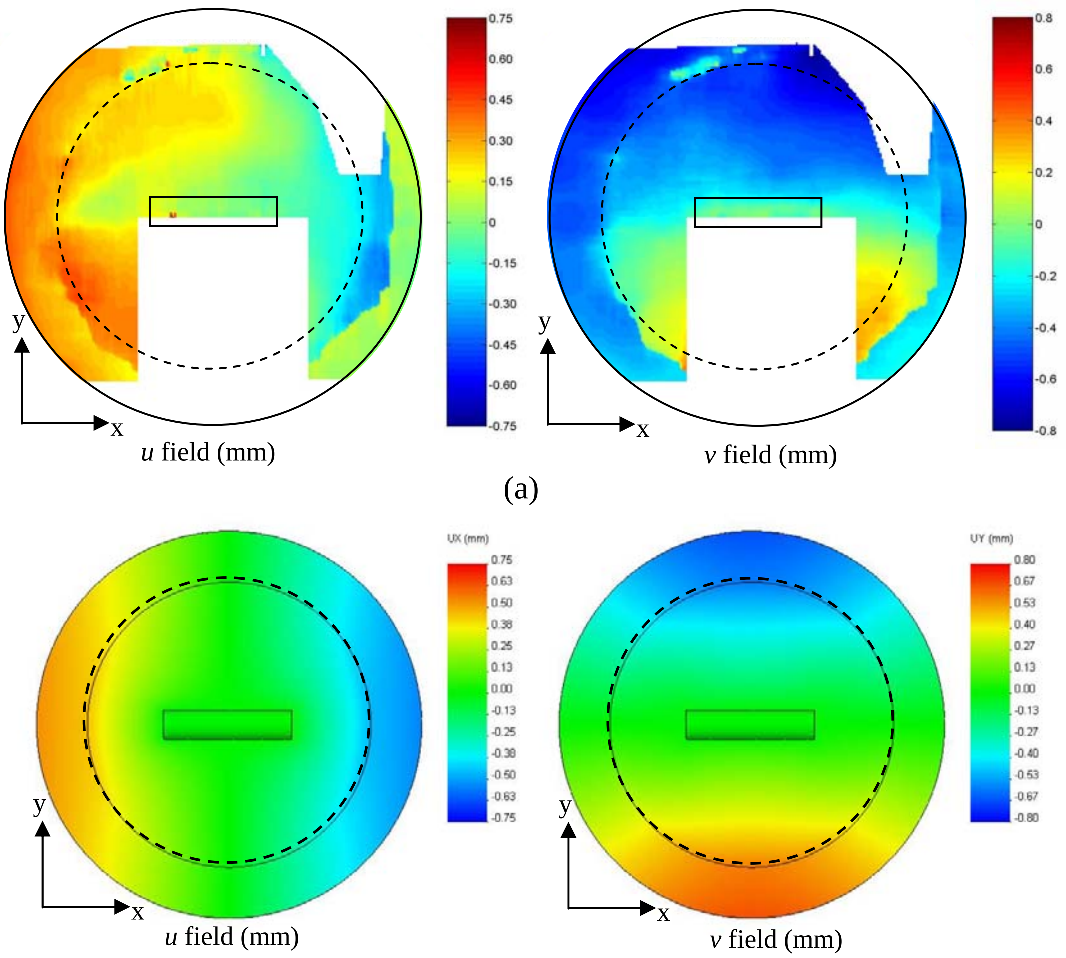

(a)

(b)

Figure 42 - (a) data and (b) FE model results for case 5

It can be seen from the plots that the relative values of displacements match up quite well. The inner part of the model also corresponds well with the inner part of the data; however, the ABS outer region of the model does not predict the appropriate response of the ABS region for the data. This could be attributed to an incorrect value assumed for the CTE of ABS. However, it is more likely the case that the model was not defined appropriately to account for sharp gradients in displacement as is the case at the interface. An attempt was made at redefining the model to account for this by using contact entities; however, this resulted in singularities and an unsolvable model. Regardless, the most important details are the displacements near the embedded component, which was captured with high accuracy.

4.4.6 Thermomechanical Finite Element Model for Case 6: Heterogeneous Material Distribution with High Friction and Embedded Component

For the final experimental case, the heterogeneous material distribution without mold release, the same dimensions were used as in case 5. The apparent CTE value for LDPE was the same value that was used for the previous high friction cases. Since it was not known how the friction affects ABS, the same percent decrease was assumed, 68 percent, making the high friction apparent CTE value α = 32x10^{-6} ºC^{-1}. The remaining material parameters for both LDPE and ABS were left unchanged. The initial and final temperatures used in the simulation were 150.6ºC and 31.9ºC respectively. The data and simulation results are shown in Figure 43.

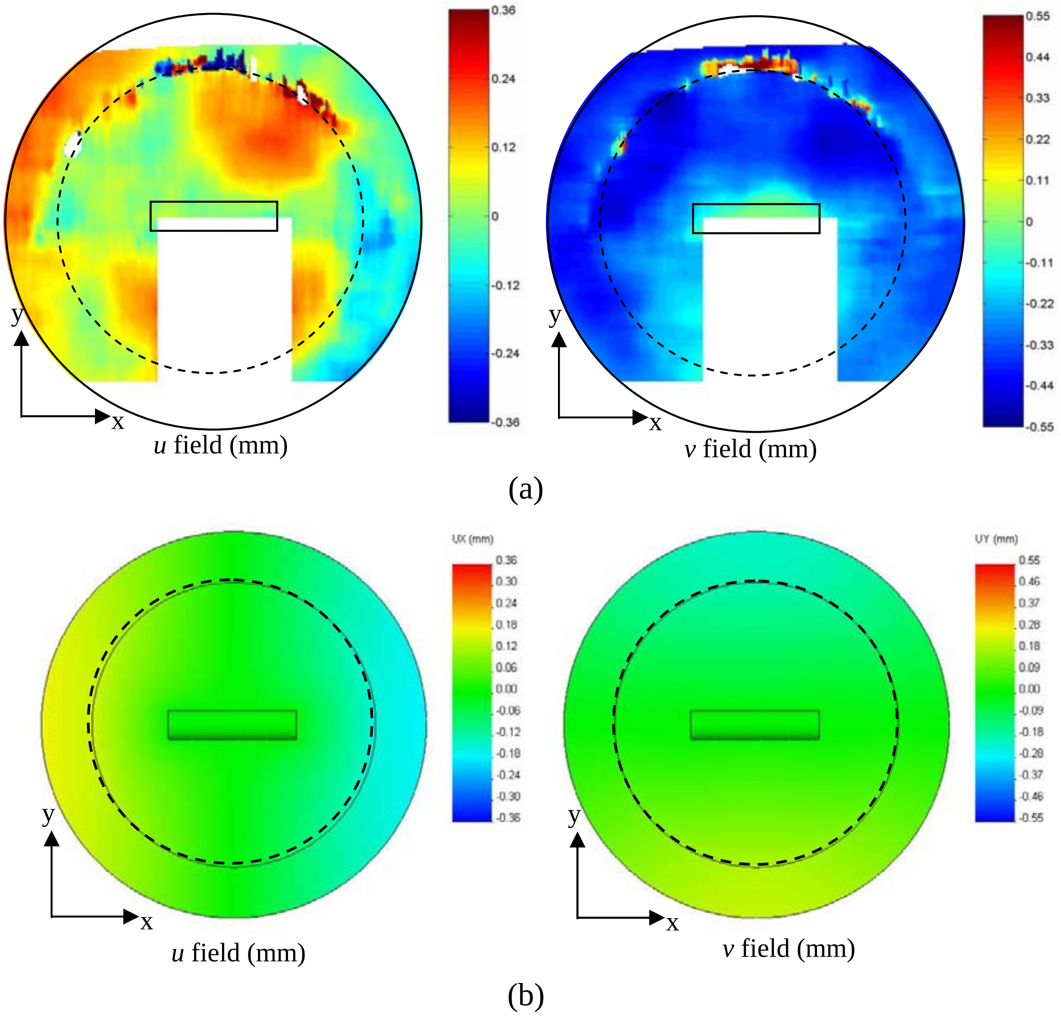

Figure 43 - (a) data and (b) FE model results for case 6

The plots indicated that the model does not capture the response of the data at all for the case of the heterogeneous material distribution without mold release. Much of this can be attributed to incorrect values of the CTE assumed for LDPE and ABS when there is friction. In addition, as discussed in the previous section, the model needs to account for steep gradients in the displacement at the interface, which this model is unable to do. These items will be left for future work.

4.5 Embedded Heating Element Experimental Setup

The previous section dealt with the processing stage of the life cycle and the thermomechanical response of multi-material modules with embedded electronic components in-mold during cooling. Using a similar approach, another phase of the life cycle of the structures can be characterized, the operational stage. It is necessary to characterize the thermomechanical strains associated with an embedded component dissipating heat so that MMIM modules can be better designed for the inherent thermal loads. The strains measured from an embedded electronic component dissipating heat allow for representative models to be developed. Using these models, the thermal stresses can be evaluated to determine whether a circuit with a given power dissipation will be damaged because the material distribution of the module is unable to conduct enough heat away from the circuit, causing components to fail.

Aside from [Sarv04], there is no published work regarding the thermomechanical behavior of embedded electronics while they are generating heat as they would under normal operating conditions. That work did not go into great detail on the experimental aspects, therefore this section aims to characterize the effects of embedded electronics on the surrounding material while generating heat. Table 18 lists the four test cases to be analyzed. The low friction cases are mostly for reference purposes and completeness since the experiments were already set up from the previous section; however it is conceivable that they represent the embedded electronic support structure that has been molded inside another structure to which it does not adhere. The high friction cases are more representative of the cross section of an actual completely surrounded molded module.

Table 18 - Description of test cases for embedded heating element experiments

Case #	Embedded Component	Friction	Material Distribution
1	Yes	Low	Homogeneous
2	Yes	High	Homogeneous
3	Yes	Low	Heterogeneous
4	Yes	High	Heterogeneous

The experiments were set up for a DIC analysis in the exact same manner as was described in Section 4.2, and included the addition of a power supply unit for generating the voltage and current for the heating elements. The experimental setup is shown in Figure 44.

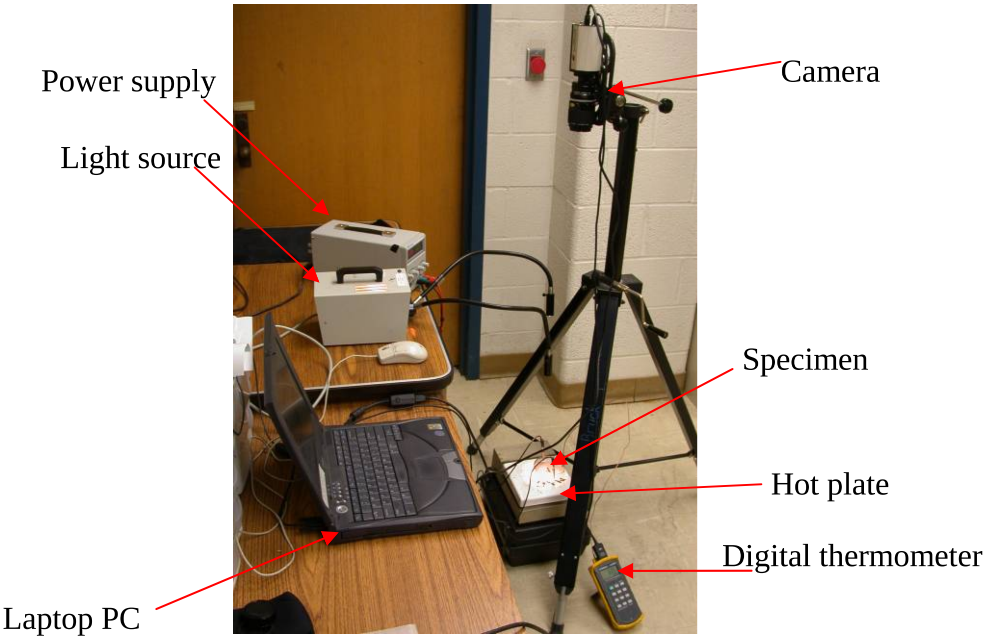

Figure 44 - Setup for embedded heating element experiments

The surrogate embedded components are in the form of heating elements, Ohmite 95J15R 15 Ohm resistors rated at 5 Watts, which were epoxied in the mold prior to adding the polymer granules. The polymer was heated and cooled around the heating element to ensure proper surface contact. Prior to turning on the power supply, a reference image was taken. After turning on the power supply, images were taken over a thirty minute period. The temperature was also recorded at the edge of the mold every 30 seconds using a laptop computer via the Omega HH506R digital thermometer.

4.6 Embedded Heating Element Experiment Results

A thorough DIC analysis was completed on the images for each of four test cases. It was determined from the analysis that most of the strains occurred within the first 10 minutes. The DIC results are discussed in the subsequent sections, again viscoelastic effects are neglected.

4.6.1 Case 1: Homogeneous Material Distribution with Low Friction and Embedded Component

The first case includes a homogeneous LDPE material distribution with the section being unconstrained aside from the epoxied heating element. The strains calculated for different heating times are shown in Figure 45.

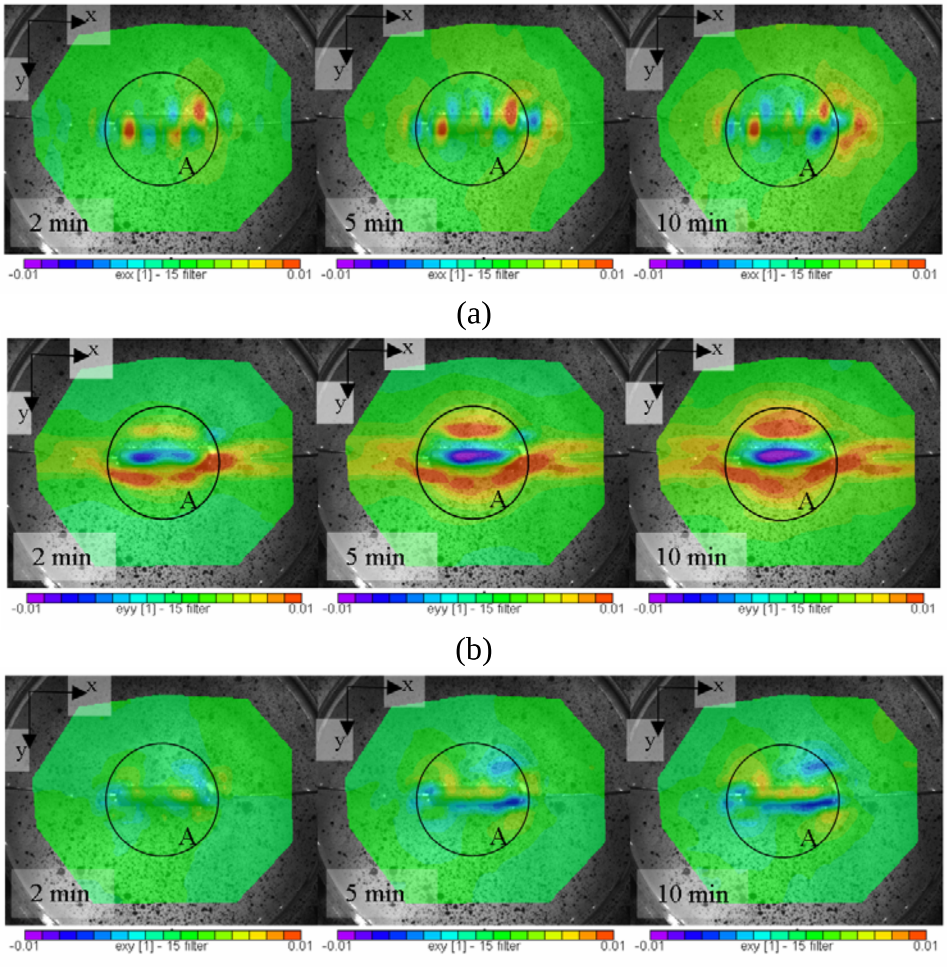

(a)

(b)

(c)

Figure 45 - Contour plots of strains with increasing heating time for case 1: (a) horizontal normal strains, (b) vertical normal strains, and (c) shear strains

By looking at the horizontal or axial strain contour plots it is seen that there are no axial effects far away from the heater. There are axial strains in localized regions near the heating element, on the order of up to 1 percent strain. For the vertical or transverse strains, there is a much more drastic effect than in the axial strain case. The transverse strains extend away from the heating element, however this effect may be attributed to the heating of the wires going into and out of the heating element.

There are also some shear strains of magnitude up to 1 percent strain, but far way from the component the field shows no effect.

Similar to the data extraction technique used in Section 4.3, the circle labeled ‘A’ in the plots shows the area that was used to extract average strain data to get an idea of the response in the form of a line plot, shown in Figure 46.

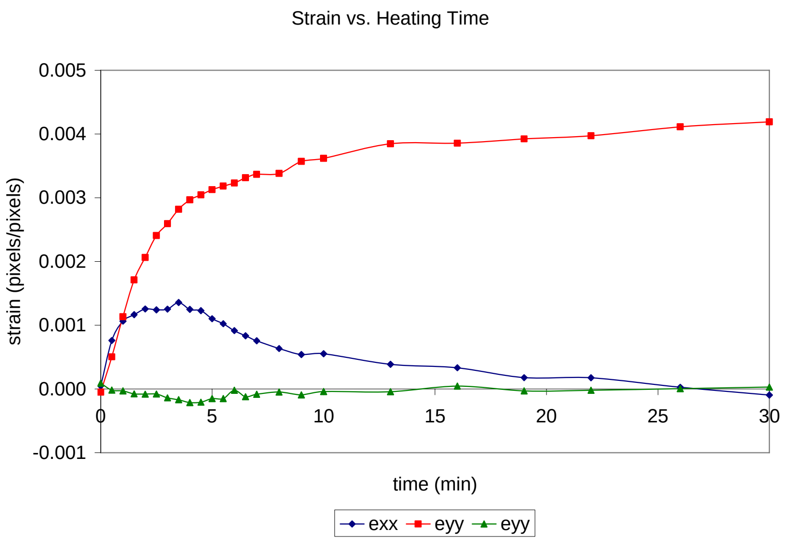

Figure 46 - Plot of strains in central region as a function of heating time for case 1

As can be seen from the plot, the average value of transverse strain is much more significant than the average value of axial strain, reaching a steady-state value of approximately 0.4 percent strain. The axial strain shows an initial increase, up to just over 0.1 percent strain, followed by a slow decrease throughout the remainder of the heating time. The average value of the shear strain starts off with small in magnitude and negative but slowly decreases and then remains negligible throughout the rest of the test.

4.6.2 Case 2: Homogeneous Material Distribution with High Friction and Embedded Component

The second case tested includes the same homogenous LDPE material distribution, but there was no initial application of mold release, resulting in some adhesion between the LDPE and the glass substrate. The DIC results for case 2 are shown in Figure 47.

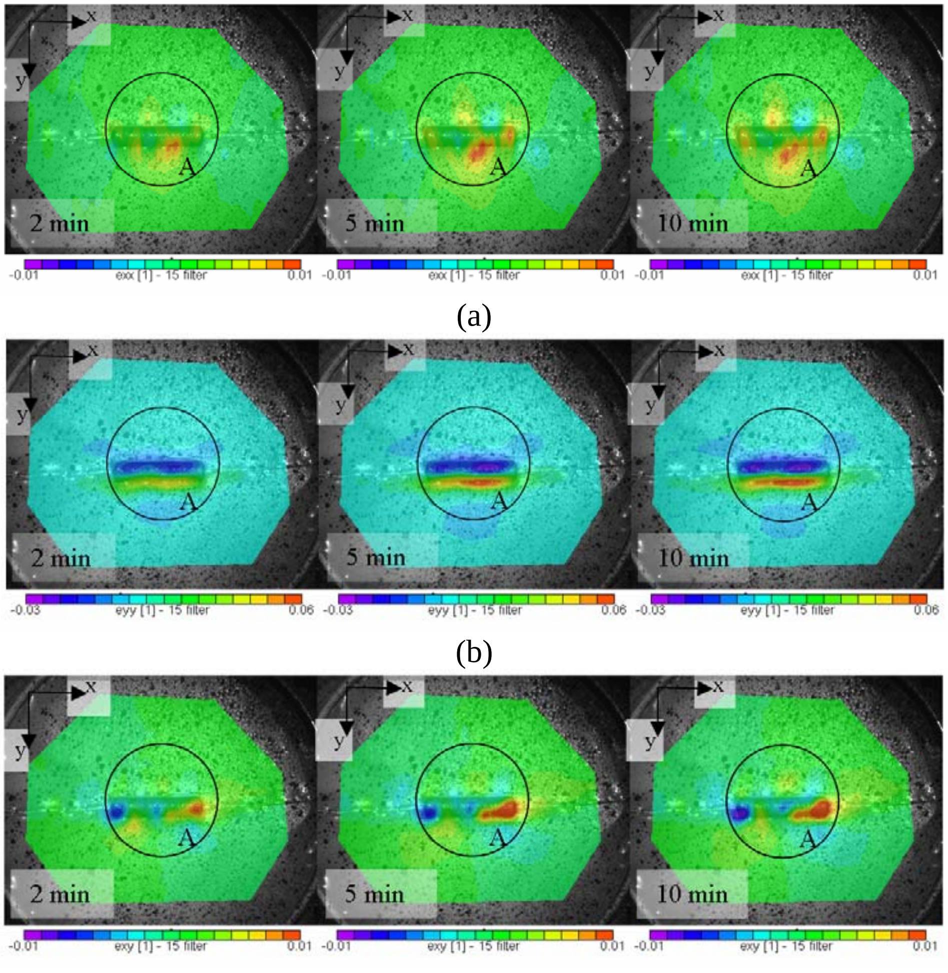

(a)

(b)

(c)

Figure 47 - Contour plots of strains with increasing heating time for case 2: (a) horizontal normal strains, (b) vertical normal strains, and (c) shear strains

Similar results as those obtained for the unconstrained case are observed here for the axial strains; the only effects are very localized in the regions near the heating element and on the order of 0.1 percent strain. Unlike the previous case, the transverse strains for this case are also contained in the vicinity of the heating element. An unexpected result is the magnitude of the transverse strain near the heating element for this case is higher than the previous unconstrained case. However, upon close examination of the specimen after the experiment, it could be seen that the polymer separated from the heating element. The excessive heat dissipated by the element caused the polymer to crack resulting in more strain than was seen in the case where the polymer was unconstrained. The shear strains show similar results as what was seen before, localized effects only.

Again the results were extracted from the portion of the plot labeled ‘A’ and these average strain values were plotted as a function of time as shown in Figure 48.

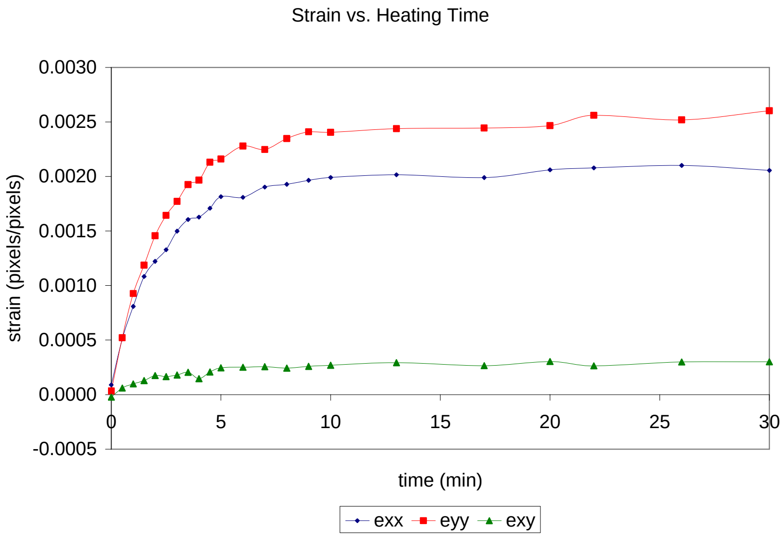

Figure 48 - Plot of strains in central region as a function of heating time for case 2

In this case the average value of the axial strain increased and did not decrease as was seen in the previous case. The magnitude of the normal strains in the central region is smaller for this case than was seen for the unconstrained case. The final strain values were attained after approximately 10 minutes, with the transverse strain being approximately 0.25 percent strain and the axial being 0.2 percent strain. Comparing magnitude of the two homogeneous cases, the addition of frictional and adhesive constraints on the system induces a 35 percent decrease in transverse strain.

4.6.3 Case 3: Heterogeneous Material Distribution with Low Friction and Embedded Component

This case represents the heterogeneous counterpart to case 1, where mold release was used in the preparation of the polymer melt. The second material is ABS as was the case in Section 4.2. The results of the DIC analysis at three different times are shown in Figure 49, where the dotted line represents the interface between the LDPE and the ABS.

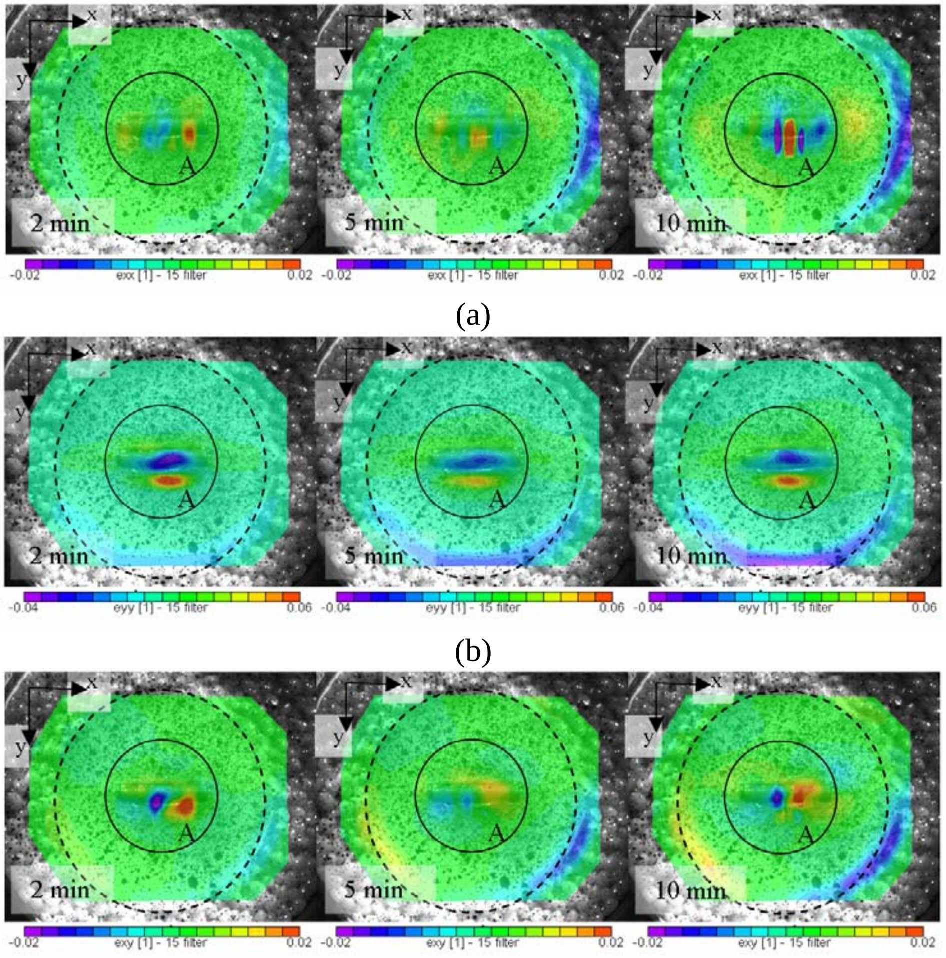

(a)

(b)

(c)

Figure 49 - Contour plots of strains with increasing heating time for case 3: (a) horizontal normal strains, (b) vertical normal strains, and (c) shear strains

It can be seen from the contour plots that the addition of a second material does result in effects far away from the heating element, which was not observed in the homogeneous cases. In both the cases of normal strains as well as shear strains there are regions at the interface where the strains are on the order of 2 percent, twice the magnitude of the highest strains for the homogeneous cases. Figure 50 shows how the average values of the strains in the central region develop over time.

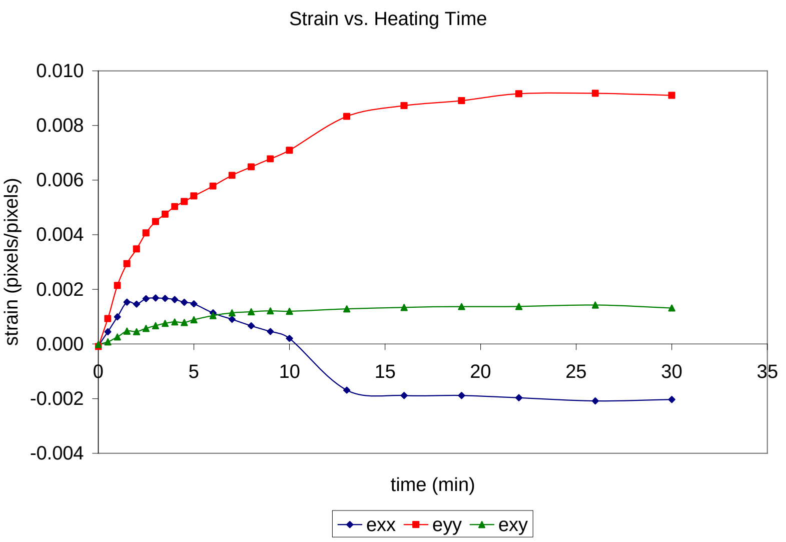

Figure 50 - Plot of strains in central region as a function of heating time for case 3

The average axial strains in the central region of the specimen have the same behavior that was observed for the unconstrained homogeneous case, leading to the conclusion that near the component the addition of the second material does not affect the axial strain. However, the transverse strain is much higher in magnitude than was seen in the previous cases; more than double what was observed for the corresponding unconstrained homogeneous case, on the order of 0.9 percent strain. The shear strain results are similar to what has been observed before.

4.6.4 Case 4: Heterogeneous Material Distribution with High Friction and Embedded Component

This final case represents the heterogeneous counterpart to case 2, where the system is constrained by the adhesion of the materials to the glass substrate. The DIC data in the form of the strains is shown at three different times in Figure 51.

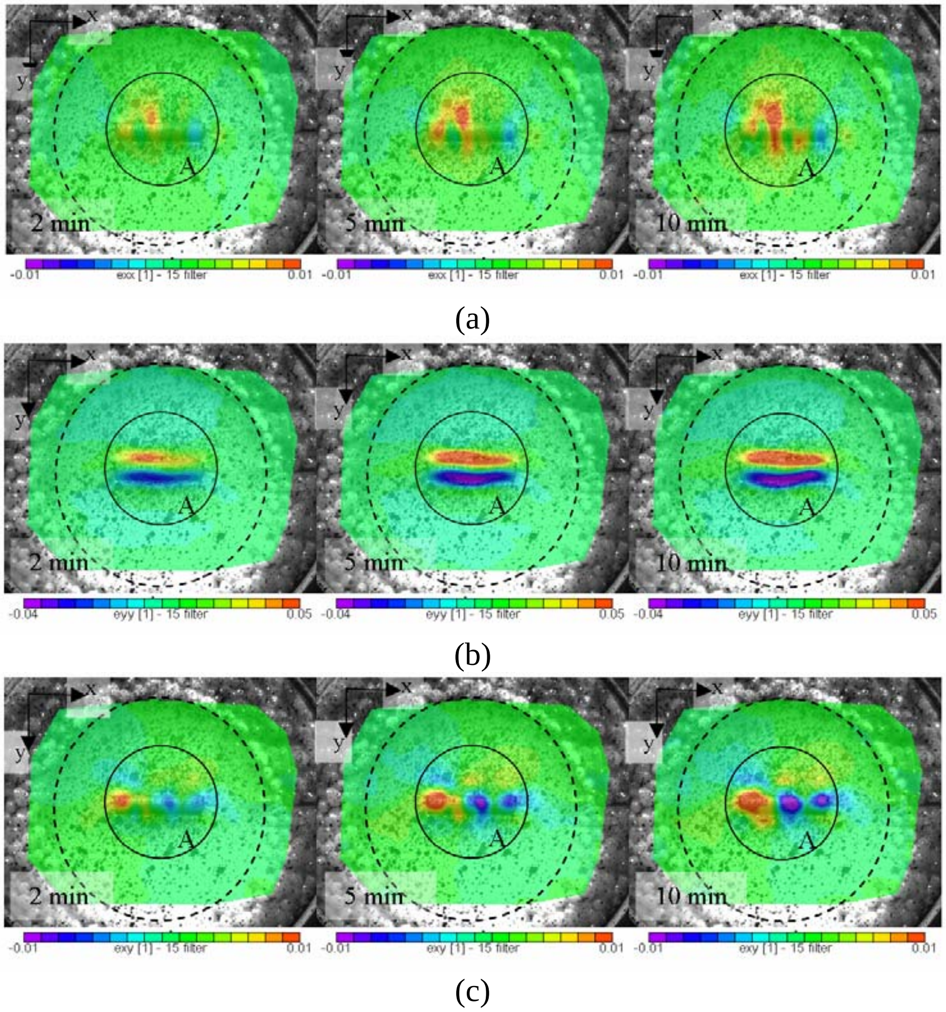

(a)

(b)

(c)

Figure 51 - Contour plots of strains with increasing heating time for case 4: (a) horizontal normal strains, (b) vertical normal strains, and (c) shear strains

In this case the contour plots of the strains are similar to the homogeneous constrained case. The effects of the heating only cause localized strains in all cases and there are no far away effects, even at the interface. The average strain rate data in the central region is plotted as a function of heating time in Figure 52 to visualize the evolution of the strains.

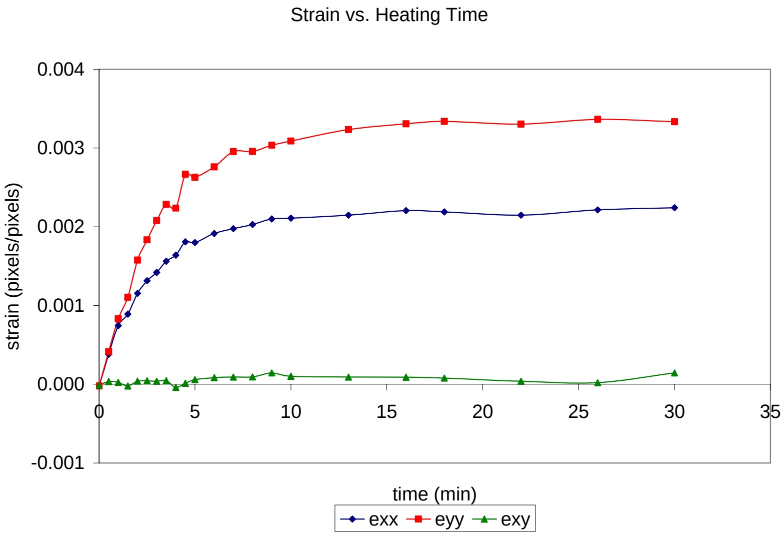

Figure 52 - Plot of strains in central region as a function of heating time for case 4

This plot also resembles the corresponding plot for the homogenous case. The only difference is that the average value of the transverse strains is slightly higher than seen in the homogenous case and in this case the shear strain remains essentially zero. The curve for the average value of the axial strain is almost identical to the one observed in case 2.

4.7 Thermomechanical Finite Element Model for Embedded Heating Element Experiments

A thermomechanical finite element model was developed to determine how well the thermomechanical response could be predicted for the experiments discussed in Section 4.6. Again COSMOSWorks was the software of choice because of the ease of implementation for this type of study. Only two cases are to be modeled, the constrained (high friction) cases, since they represent cross-sections of a larger structure, whereas the unconstrained cases are too ideal. Since the temperature profile of the specimen during heating is not known at every point, a two part approach must be taken. The first part includes developing an appropriate transient thermal model. This involves arriving at the appropriate convective boundary conditions that accurately represent the transient temperature profile experienced by the module with embedded heating element. The second step involves using the obtained temperature profile as an input and running a static analysis to obtain the displacements and strains where plasticity was again neglected.

4.7.1 Thermomechanical Finite Element Model for Case 2: Homogeneous Material Distribution with High Friction and Embedded Component

The specimen from case 2 is modeled as a solid disk with the thermal parameters discussed in Chapter 3 for LDPE ($k = 0.39$, $c_p = 2200$ J/kg-K, $\rho = 890$ kg/m^3). The heating element is modeled as a solid cylinder with a uniform heat power of 4.1 Watts as measured during the experiments. The bottom of the disk is insulated and the top and sides of the disk given convective boundary conditions. The model is run with ambient temperature of 22.8ºC and different values of the convection coefficient until the correlation of the temperature profile at the outside boundary and the data recorded during the heating experiment is satisfactory. Figure 53 shows the transient profile obtained for a point on the outer edge of the specimen during the heating experiments and the obtained results for a corresponding point on the model with an average convection coefficient of 14 W/m^2-K.

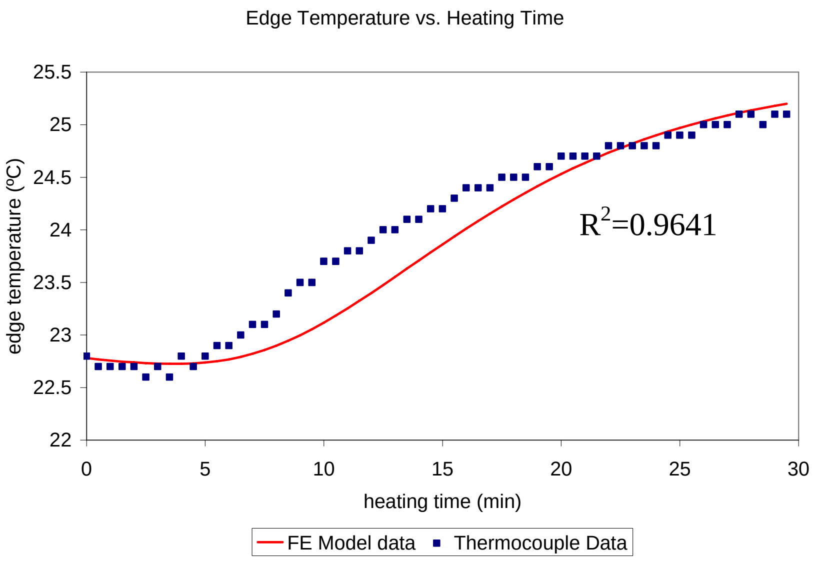

Figure 53 - Transient thermal profile for point on outer edge

As can be seen from the value of Pearson's coefficient in the plot, the conditions arrive at a suitable transient thermal profile. The resulting temperature profile in the solid disk at the final time step is shown in Figure 54.

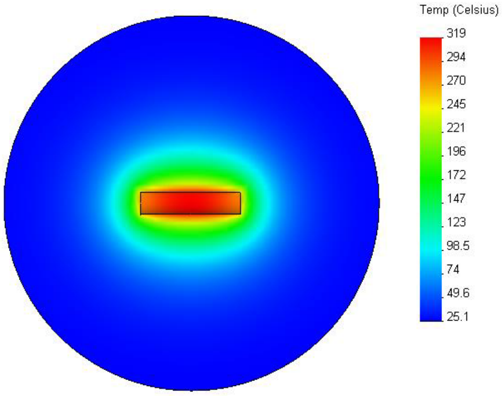

Figure 54 - Temperature profile for heating element models

The temperature profile shows that far away from the heating element the temperatures are near constant throughout the module, whereas near the heating element there are steep gradients in temperature. The profile indicates that the temperature at the center of the heating element is over 300ºC, which is probably higher than the actual temperature during the experiments, however the temperature during the experiments was still high enough to melt and in some cases crack the polymer.

For the second step of the thermomechanical modeling effort, the temperature field calculated in the first step is input into the static analysis model with the same configuration and same mesh. The apparent CTE used for the static analysis in this case is the same apparent CTE that was determined from linear end portion of the strain curve the in-mold cooling experiments, $\alpha = 62\text{x}10^{-6}$ ºC^{-1} and the material parameters are the same as used in the previous thermomechanical analysis (E_{LDPE} = 0.23 GPa, ν = 0.35). The parameters for the heating element were the manufacturer supplied value of CTE, $\alpha = 30\text{x}10^{-6}\ {}^{o}\text{C}^{-1}$, and literature values for the elastic modulus (E_{heater} = 100 GPa) and Poisson's ratio (ν = 0.22). The bottom surface is constrained in the out-of-plane direction and the edge of the disk is fixed. Using these boundary conditions, the resulting displacements are calculated and compared to the data obtained from the VIC-2D and subsequent MATLAB calculations as shown in Figure 55. It should be noted, in this case it was not possible to reduce the size of the model to the size of the field calculated by VIC-2D because the thermocouple data was recorded at the outer edge of the specimen.

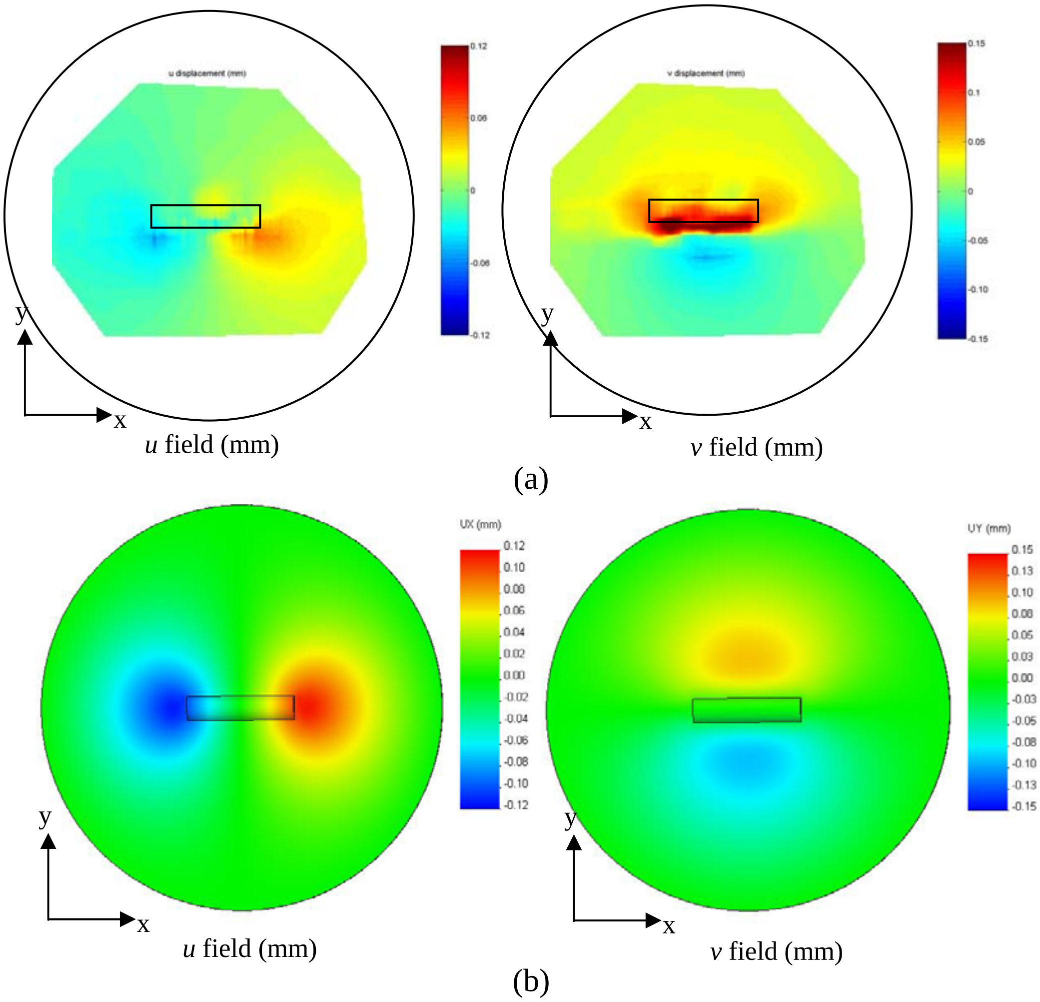

Figure 55 - Displacement fields for case 2 (a) data and (b) FE model

The circle around the data contour plots in Figure 55 (a) shows the outer diameter of the model and the heating element is shown by the rectangle. As can be seen from the contour plots, the model does a very good job capturing the local displacements near and far away from the heating element for the homogeneous material case. There are some values of strain that appear in the data, but do not seem to appear in the model results; however, this is mostly due to the large portion of the model that appears green, which takes up a wide range of strain values according to the legend.

4.7.2 Thermomechanical Finite Element Model for Case 4: Heterogeneous Material Distribution with High Friction and Embedded Component

Having developed a two-part thermomechanical finite element model that can predict the response of a heating element embedded in a homogeneous polymer, the model was applied to a heterogeneous structure. The dimensions of the model had to be modified to be similar to the experimental specimen measurements, resulting in an inner radius of 26.5 millimeters and an outer radius of 48.5 millimeters. The same boundary conditions that were applied to the homogeneous transient thermal model were applied to the heterogeneous transient thermal model, with the material parameters for the ABS being those arrived at from the previous analyses (Apparent CTE $\alpha = 32\text{x}10^{-6}\ ^{o}\text{C}^{-1}$, $k = 0.18$, $c_p = 2000$ J/kg-K, $\rho = 980$ kg/m^3, $E_{ABS} = 2.3$ GPa, $\nu = 0.35$). The resulting thermal profile was input into the static analysis solver with the same boundary conditions as in case 2. The resulting displacement fields shown in

Figure 56 were obtained where the dotted line represents the interface between the LDPE and the ABS.

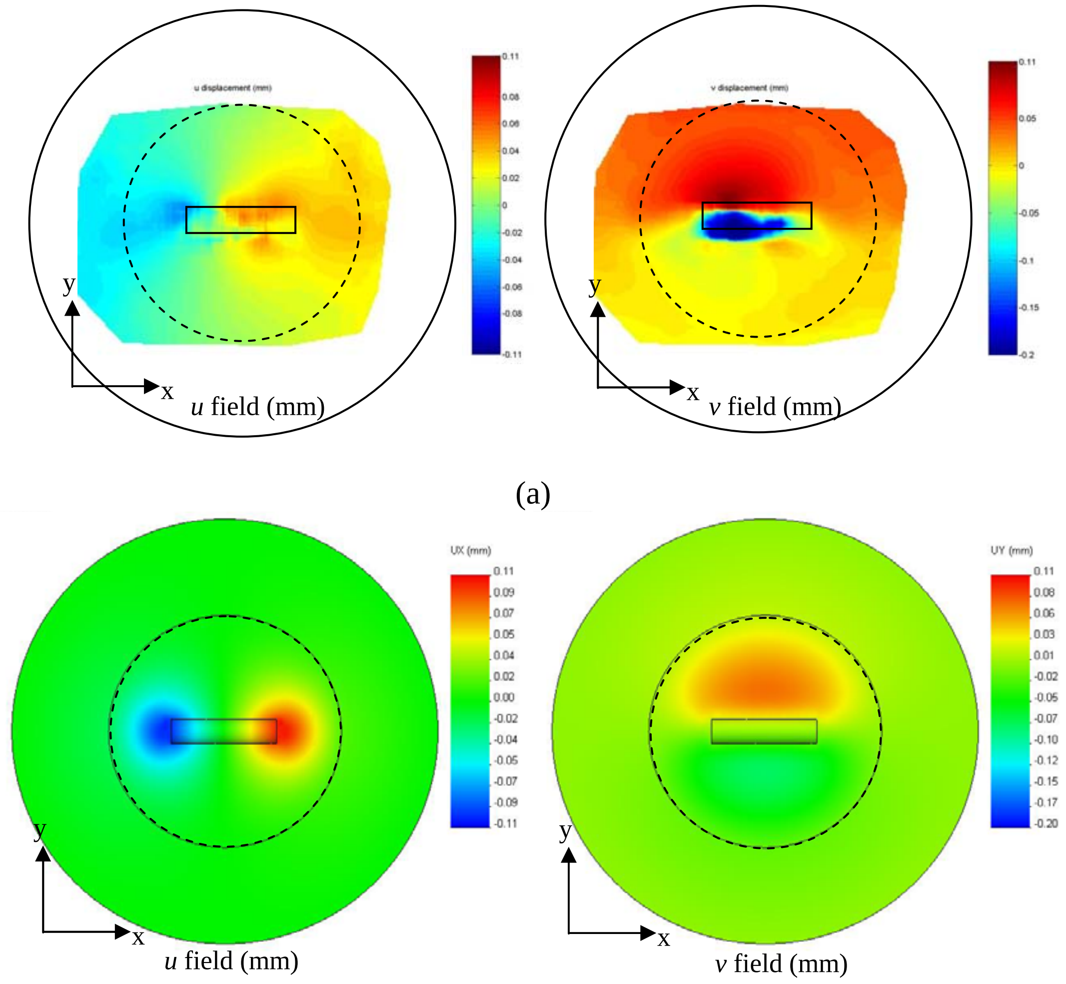

(a)

(b)

Figure 56 - Displacement fields for case 4 (a) data and (b) FE model

As can be seen from the displacement fields, the model is a fairly accurate representation of the actual experimental data. The *v* field is not quite represented as well as possible, but there are many factors that could be contributing to this. Examples of the errors could be incorrect value of thermal conductivity used in the thermal model resulting in the incorrect temperature profile or incorrect convection coefficient which is possible since the model size is larger. The *u* field of the model results agrees well with the *u* field obtained from the experimental data. Overall the model could be improved slightly, but given the room for error in running a two-part model especially with large temperature gradients, it is a relatively accurate tool to use for predicting the thermomechanical response of multi-material structures with embedded heating elements.

4.8 Conclusions and Contributions

In this chapter, in-mold cooling experiments were conducted to gather information on the thermomechanical behavior of homogeneous and heterogeneous molded modules using the DIC technique. It was observed that there is a 35 percent decrease in strain magnitude upon a cooling polymer changing phase in mold. This is the first time that an expansion as a polymer changes phase has been observed, however the overall cooling process does result in shrinkage for the homogeneous cases. The effects of friction were characterized, and it was concluded that the overall strain in low friction mold conditions results in approximately 3-3.5 percent strain, which is reduced down to 1-1.5 percent strain when a mold release agent is not present. In addition, it was observed that the friction increases the anisotropy of the thermomechanical strains upon cooling. An apparent CTE can be calculated for the linear portion of the cooling curve, which decreases by 87 percent without the use of a mold release agent. The change in the strain fields associated with the addition of a stiffer electronic component were analyzed and determined to show increased positive strains in the transverse direction, but decreased shrinkage in the axial direction. The effects of adding a second material dominates the effects of friction and embedding component factors because of the large strains at the interface between the materials.

Experiments were also conducted concerning the heat generation caused by the operation of embedded electronic components in molded modules represented by an embedded heating element. The DIC technique was utilized again to analyze the strain fields associated with the thermomechanical response of homogeneous and heterogeneous material distributions with the embedded heating elements. The results of the analysis indicate that for the homogeneous cases the strains are quite localized because of the high thermal resistance of the polymer. The effect of a heterogeneous distribution of material is quite pronounced, the strains are no longer only in the regions near the heating element, but also are significant in the interface region between the materials.

In addition to the described characterization effort, more contributions are made in the form of thermomechanical finite element models. A thermomechanical finite element model was developed to represent the in-mold cooling experiments to show that the thermomechanical response of homogenous and heterogeneous material systems with and without embedded electronic components can be predicted within a reasonable amount of accuracy.

Another thermomechanical finite element model was developed to represent the embedded heating element experiments. This model includes two parts, a transient thermal analysis to calculate a temperature profile and a static analysis that uses the temperature data to calculate the thermomechanical response. This model shows that the thermomechanical response of homogeneous and heterogeneous molded modules with embedded heating elements can be reliably predicted. Finite element models such as these provide a platform to show that more complex models can be developed to accurately represent and predict the thermomechanical behavior of more advanced material systems or embedded electronic assemblies.

Chapter 5: Development of Multi-Functional Structures Fabricated by Multi-Material Molding Processes

5.1 Introduction

This chapter serves as a proof of concept chapter, meaning that it shows that it is possible to develop affordable, mass producible multi-functional structures with embedded electronic components fabricated by a MSM process. This is accomplished in two steps. The first step involves the design and fabrication of a serpentine robot using a MSM process, which is the focus of Section 5.2. The research discussed in this section was actually conducted prior to performing the research discussed in all of the previous sections to show that it is possible to produce affordable, molded serpentine robots without wheels. The second step is addressed in Section 5.3, where it is shown that it is possible to embed electronic components for rugged and robust applications using a MMIM process.

5.2 Development of a Serpentine Robot Using a Multi-Stage Molding Process

This section addresses the necessary steps for developing a serpentine robot fabricated by a MSM process. The first step in designing an affordable serpentine robot for search and rescue reconnaissance type applications is to develop the design objectives. For this serpentine robot design, it was decided that the most important objectives to meet are:

- Modular
- Self-sufficient
- Scalable
- Inexpensive
- Require few manufacturing steps
- Mission time >30 minutes

Many of the existing designs of serpentine robots make use of modules connected in series that form the serpentine configuration. For this work, it was also decided to make use of a modular design as this would aid in reducing manufacturing costs and steps. Another design objective is for each module to be self-sufficient. This implies containing all necessary components for supplying power, controlling motors, and also housing the motors. Having a design that is scalable is another requirement, as this makes it possible to have choices on robot size depending on the particular situation. One of the problems associated with other serpentine robots is that they are extremely expensive, making it costly to use in dangerous and extreme environments. Therefore, one of the goals of this design is to have a robot that is inexpensive enough that if it happens to be incinerated, the monetary loss is not substantial. In order to keep the robot inexpensive, another objective is to limit the number of assembly operations and minimize the number of manufacturing steps. The final design objective is to design for a mission time of over 30 minutes, enabling rescue workers enough time to use the robot for its intended purpose, finding victims.

The design of the serpentine robot is broken into three sections: mechanical system, electrical system, and gait implementation.

5.2.1 Mechanical System

The mechanical system is comprised of two subsystems; the actuation subsystem and the structural support subsystem. Descriptions of the decision making process for the design of each of these subsystems are given in the following sections.

5.2.1.1 Actuation Subsystem

Before designing the structural support system or the actuation subsystems of a serpentine robot, it must first be decided what kind of global motion is to be achieved. There are essentially four common modes, or gaits, of snake locomotion: serpentine, side-winding, concertina, and rectilinear as shown in Figure 57(a), (b), (c), and (d) respectively [Gray50, Liss50]. In developing a serpentine robot without using wheels as others have done such as [Hiro93, Klaa99, Cresp05] the rectilinear is the simplest to mimic because it does not require complex frictional properties to achieve the motion.

(a) (b) (c) (d)

Figure 57 - Snake locomotion gaits: (a) serpentine, (b) side-winding, (c) concertina, and (d) rectilinear

In order to achieve a global rectilinear gait, the movement that is necessary for each module is local rotation in the vertical plane. As long as local rotation of one module relative to the next can be provided, a global rectilinear gait can be achieved similar to a caterpillar gait.

The functional requirements of the actuation system are shown in block diagram form in Figure 58. It is worth noting that the input energy can be of any form, such as thermal, electrical, solar, or chemical, so as to not eliminate any possible design solutions. From the diagram it can be seen that there are five requirements to be satisfied in order to achieve and control relative rotation between modules.

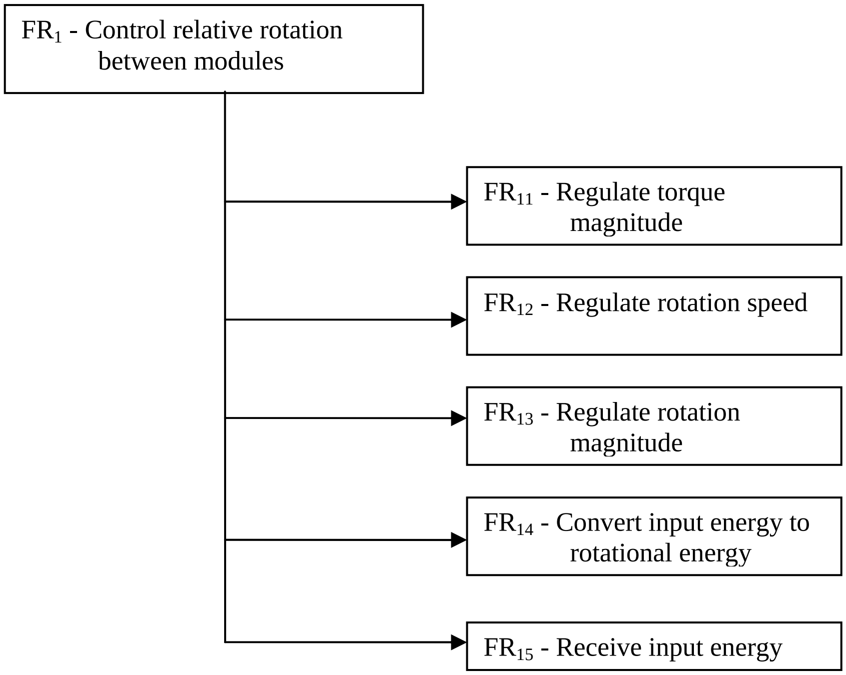

Figure 58 - Functional requirements block diagram

In order to address these functional requirements, all of the possible existing actuation techniques are examined. Developing a new technology for actuation has not been considered since it would most likely add to the cost of the robot significantly. Ideally, the actuation system would be as efficient as possible; however as is shown in the following sections, there are tradeoffs that must be considered.

The metrics that are used to evaluate the performance characteristics of possible actuation systems are shown in Table 19.

Table 19 - Metrics used to describe actuators

Quantity	Units (SI system)
Force or Torque / Stress	Newtons (N) or Newton-meter (Nm) / Pascals (Pa)
Stroke or Rotation/ Strain	Meters (m) or Degrees (º) / Percent (%)
Response time / Frequency	Seconds (s) / Hertz (Hz)
Lifetime	Number of cycles (#)
Mass / Density	Kilograms (kg) / Grams per cubic centimeter (g/cm^3)
Efficiency	Percent (%)

Other important actuator characteristics include actuation mode, power source, environment, and supplementary hardware. For the actuation mode, design choices are rotational or linear, and push or pull. Power sources can be electrical, thermal, or chemical. Common actuation environments include water, air, and vacuum. Some of the supplementary hardware includes linkages, fluid connections, pumps, and controllers.

Conventional actuation techniques for the most part involve moving a shaft, either by rotation or translation, by a power source which is usually electrical. Discussed in the following sections are four types of conventional actuation systems: servos, electric motors, pneumatic actuators, and hydraulic actuators.

Servos

A servo is a feedback-controlled device that has a rotating output shaft that can be positioned to specific angular orientations, depending upon the coding of the input signal from the controller. The metrics for servos are shown in Table 20.

Table 20 - Metrics for servos

Metric	Value
Torque	< 5 Nm
Rotation	0º - 180º
Frequency	< 40 Hz
Lifetime	> 10^5 cycles
Mass	50 - 100 g
Efficiency	< 75%

Overall, servos for robotics applications have high torques and high power outputs with small electrical inputs on the order of 4 to 7 volts. Since one of the largest markets for servos is they have been used in the actuation of radio controlled models, the weights and sizes of servos are continuously being made smaller and smaller. In addition to this, the cost of servos is low, between $10 and $60 for most applications. One major drawback of actuation with servos is the control system which becomes more and more complicated with the addition of every servo.

Electric Motors

Electric motors include all motors driven by electric energy that dos not require a coded signal as a servo does. Electric motors strictly rotate at a constant speed whenever a voltage is applied and stop whenever the voltage is interrupted. Examples of electric motors are direct current (DC) motors, alternating current (AC) motors, brushless DC motors, synchronous motors, asynchronous motors, and stepper motors. In addition, electric motors can be used to turn screws for linear actuators. Although there are many types of electric motors, the metrics for those used in robotics applications are similar and are listed in Table 21.

Table 21 - Metrics for electric motors

Metric	Value
Torque	< 0.5 Nm
Rotation	360º
Frequency	< 45 Hz
Lifetime	> 10^6 cycles
Mass	100 – 200 g
Efficiency	< 95%

The electric motors used for small-scale robotics applications have less torque than servos for the most part. However, as discussed previously, electric motors only require an input power which makes them easier to control. Many wheeled robots take advantage of this and use electric motors to provide the torque necessary to turn the wheels. Another common trait among electric motors is that they are slightly larger and heavier than servos. In addition, although specific angular orientations can be achieved using large diameter gears, this makes the overall system even larger and heavier. One of the major advantages of electric motors over servos is the very high efficiencies, but they do typically require more input energy than servos, anywhere from 4 to 24 volts.

Pneumatic and Hydraulic Cylinders

The underlying principles behind pneumatic and hydraulic are quite similar; a force is applied to one piston-cylinder device and the other one responds to keep the system in equilibrium as shown in Figure 59. The working fluid in a pneumatic actuator is a gas, usually air, whereas the working fluid in a hydraulic actuator is a liquid, usually hydraulic oil. The output force is equal to the input force times the ratio of Area 2 to

Area 1, where Area 1 and Area 2 are the cross sectional areas of the input cylinder and output cylinders respectively.

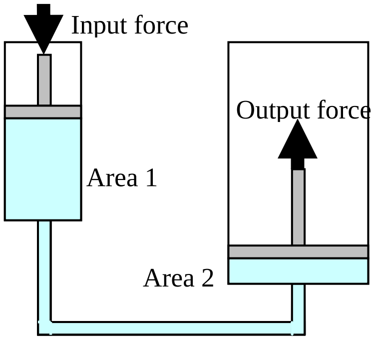

Figure 59 - Hydraulic and pneumatic system diagram

The term cylinder actuators will be used from here on to describe both pneumatic and hydraulic actuators because of their similarities. The metrics for cylinder actuators are shown in Table 22.

Table 22 - Metrics for cylinder actuators

Metric	Value
Stress	$< 10^6$ MPa
Strain	< 100%
Response time	$\sim 10^{-1}$ second
Lifetime	$> 10^6$ cycles
Mass	40 – 1600 g
Efficiency	> 80%

Typical cylinder actuators used in robotics are lightweight, but either a pressurized tank is required for pneumatics, or a pump is required which adds to the weight significantly. Alternatively, cylinder actuators provide a higher force per unit mass than other actuation techniques [Binn95]. This implies that cylinder actuators may be able to make up for the added weight of a tank or pump because they can output more power. In addition, the efficiencies of cylinder actuators are high, topped only by high performance electric motors.

Since the concept of the serpentine robot is itself bio-inspired, it is thought that the optimal actuation system may itself be a bio-inspired system. Several of these techniques, inspired by natural muscles, are described in the following sections such as shape memory alloys, shape memory polymers, electroactive polymers, and piezoelectric materials. The main advantage of these methods over the traditional methods for is that the materials themselves provide the actuation when a voltage or increase in temperature is applied.

Shape Memory Alloys

An SMA is a metal that experiences the shape memory effect which is made possible via phase changes, as shown in Figure 60. In the martensite phase, an SMA is soft and easily deformed, but upon heating the phase changes to austenite and the original shape is recovered if unconstrained. One disadvantage of the shape memory alloy wires is that training of the wires is necessary.

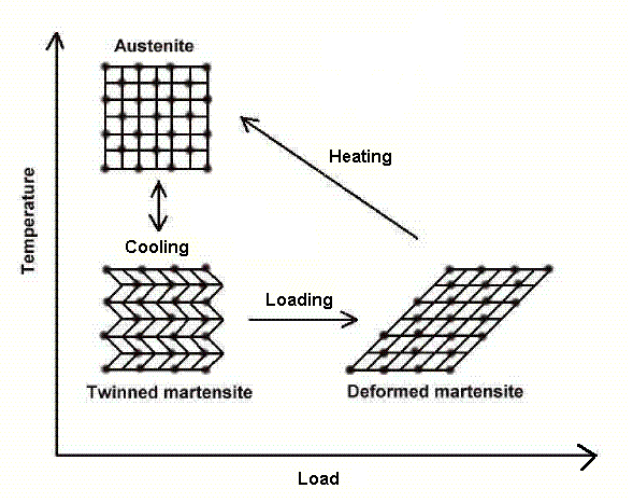

Figure 60 - Microscopic diagram for shape memory alloys

Common shape memory materials include nickel-titanium (NiTi), copper-zinc-aluminum (CuZnAl), copper-aluminum-nickel (CuAlNi), and iron-manganese-silicon (FeMnSi) [Bord91]. The metrics for NiTi, the most common SMA, are listed in Table 23.

Table 23 - Metrics for shape memory alloys

Metric	Value
Stress	< 200 MPa
Strain	< 8%
Response time	~ 1 second
Lifetime	> 10^6 cycles
Density	~ 8 g/cm^3
Efficiency	< 5%

SMAs are commercially available and are inexpensive. The price depends upon the diameter of the wire, but most wires cost between $15 and $25 per meter. Typical recoverable strains near 8% can be achieved in SMA wires, but for cyclic actuation the 3-5% range is more realistic. One of the drawbacks of SMAs is the response time. The austenite phase can be reached fairly quickly by resistance heating, but cooling back to martensite can pose more of a problem and takes more time. The recovery weight, or actuation force, is highly dependent on the diameter of the wire. However, several wires can be placed parallel to each other to obtain the same overall strain with much more force than a single wire. The efficiency of SMAs is on the order of 5%, making them much less efficient than any of the conventional actuation techniques.

Shape Memory Polymers

Similar to the shape memory alloys, another class of materials, called shape memory polymers (SMPs), also exhibits the shape memory effect. SMPs change from a rigid state to a flexible state above a critical temperature known as the glass transition temperature. If heated, deformed, and then heated above the glass transition temperature again, it will revert back to its original "memorized" shape. Unfortunately, SMPs are not as readily available as SMAs, making it difficult to obtain mechanical property and performance information. However, one major advantage of SMPs is that they are easily molded and a variety of shapes can be fabricated for different actuation situations.

Electroactive Polymers

An electroactive polymer (EAP), also known as a dielectric polymer, can change shape in response to an applied voltage. Typically, two compliant electrodes are separated by the insulating polymer. When a potential difference is placed across the two electrodes, an attractive force is generated between the electrodes and the polymer is squeezed and it expands laterally because of its incompressibility as shown in Figure 61.

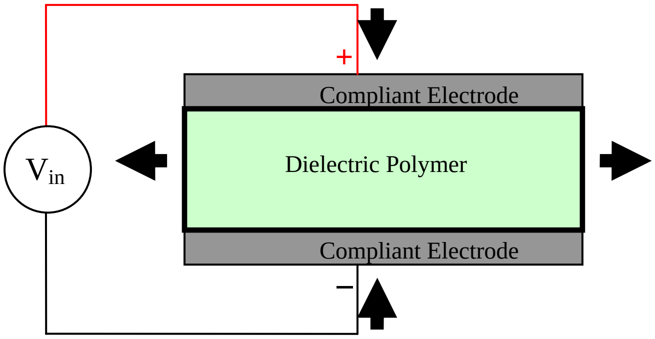

Figure 61 - Electroactive polymer diagram

Some of the more common types of elastomers used are polyurethane, butadiene, isoprene, and silicone. The type of elastomer used in this technology is not too critical, as long as it is compliant, incompressible, and insulating. The metrics for EAPs are shown in Table 24.

Table 24 - Metrics for electroactive polymers

Metric	Value
Stress	< 10 MPa
Strain	< 300%
Response time	$< 10^{-3}$ second
Lifetime	$< 10^{7}$ cycles
Density	~ 1 g/cm^3
Efficiency	< 90%

These polymers are referred to as low stress-high strain, similar to biological muscle. EAPs are capable of the highest strains of all of the actuators discussed. The response time is quick and the density is low. These properties together with high efficiencies make for a good actuation material. However, EAPs also have disadvantages. The stress is low, which implies that the forces generated may not be strong enough for robot locomotion. In addition, even to develop these small forces high voltages must be applied, on the order of 100 volts per millimeter of thickness of polymer. But, the technology is fairly new and future developments in this area may give rise to better results.

Piezoelectric Materials

Piezoelectric (PE) actuators are permanently polarized materials that change shape when an electric field is applied. They can be ceramics, polymers, or even molecules, but most commercially available piezoelectric materials are made of a ceramic material, lead-zirconia-titanate (PZT, short for PbZrTi). Stack PEs, those often encountered in robotics applications, make use of layers of PZT to obtain a larger total stroke. Unlike electroactive polymer actuators, multilayer PZT stacks increase in thickness in the direction of the applied electric field as is shown in Figure 62.

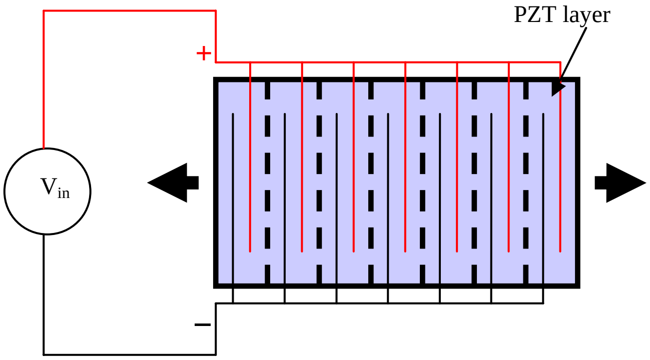

Figure 62 - Piezoelectric stack diagram

Like SMAs, PEs are commercially available in many sizes and shapes. They are actually quite frequently used in micro-electromechanical systems (MEMS) which has given PE's a considerable amount of attention. The metrics for stack-type PEs that may be used for robotics applications are shown in Table 25.

Table 25 - Metrics for piezoelectric actuators

Metric	Value
Stress	< 150 MPa
Strain	< 2%
Response time	$< 10^{-3}$ second
Lifetime	$> 10^{9}$ cycles
Density	~ 8 g/cm^3
Efficiency	< 70%

PEs are capable of generating large forces on the level with SMAs, but the strains developed are quite small. However, they do have fast response times, nanometer level resolution, and can be cyclically loaded many times before failure. One of the major advantages of PEs is their size, but still fairly high voltages need to be applied, at least 150 volts even for a PE actuator cube as small as 3 millimeters on a side. Another major disadvantage of PEs is their cost. Although there are many brands to choose from, competition has not yet driven PE prices down, average costs are well over $100 per actuator.

Selection Process

In order to determine which actuation technique to choose, all of the metrics must be compared and weighted to ensure that the most important characteristics of the serpentine robot are addressed appropriately. To accomplish this, an analytical hierarchy process is completed as shown in Table 26. Each metric was compared to the others across the rows and given a rank of 1, 3, 5, 7, or 9 based on importance to the final goals of the disposable serpentine robot. Two more metrics were added to the chart for comparison purposes; cost and input power. Both of these quantities are extremely important in the design of an affordable, scalable robot.

Table 26 - Analytical Hierarchy Process Table

Metric	Number	1	2	3	4	5	6	7	8	Total	Weight
Torque/ Stress	**1**	1.00	5.00	5.00	7.00	0.33	0.20	0.20	5.00	23.73	0.19
Rotation/ Strain	**2**	0.20	1.00	0.14	5.00	0.14	0.20	0.14	3.00	9.83	0.08
Response time/ Frequency	**3**	0.20	7.00	1.00	7.00	0.20	0.33	0.14	0.33	16.21	0.13
Lifetime	**4**	0.14	0.20	0.14	1.00	0.20	0.33	0.11	0.14	2.27	0.02
Mass/ Density	**5**	3.00	7.00	5.00	5.00	1.00	5.00	0.20	3.00	29.20	0.23
Efficiency	**6**	5.00	5.00	3.00	3.00	0.20	1.00	0.33	0.33	17.87	0.14
Cost	**7**	5.00	7.00	7.00	9.00	5.00	3.00	1.00	7.00	44.00	0.35
Input Power	**8**	0.20	0.33	3.00	7.00	0.33	3.00	0.14	1.00	15.01	0.12

The ‘weight’ column in Table 26 shows the importance of the metrics, with cost, mass, and torque being the most important for this application. Other metrics such as lifetime and rotation/strain have rank low in comparison because it is not felt that these are as important. Since the robot is to be inexpensive, the lifetime is not too important because it may be considered replaceable. The rotation or strain is not considered to be extremely important either because gears can be used to magnify the amount or rotation or strain. Once these weights are determined, each actuation technique can be compared to the others using the previously discussed metrics and their weights in a weighted decision matrix. The weighted decision matrix is shown as Table 27.

Table 27 - Weighted Decision Matrix

Metric	**Weight**	**Servo**	**Electric Motor**	**Cylinder**	**SMA**	**EAP**	**PE**
Torque/ Stress	0.20	4	5	6	3	1	2
Rotation/ Strain	0.08	3	4	5	2	6	1
Response time/ Frequency	0.13	3	4	2	1	5	6
Lifetime	0.02	1	3	4	2	5	6
Mass/ Density	0.24	3	1	2	5	6	4
Efficiency	0.15	3	6	4	1	5	2
Cost	0.33	5	4	2	6	3	1
Input Voltage	0.12	5	4	3	6	1	2
Total		**4.93**	**4.89**	**4.09**	**5.04**	**4.77**	**3.25**

The different actuation techniques are ranked from 1 to 6 with 6 being the highest and 1 being the lowest. The highest scoring actuation technique did turn out to be a biologically-inspired one, shape memory alloy, showing once again how beneficial biologically-inspired materials and structures can be. Due to the particular applications that the robot is being designed for, such as search and rescue reconnaissance missions which may involve heat from fires, the notion of using heat controlled actuation devices like SMA wires was abandoned. In lieu of this, the second highest scoring actuation technique, servo motors, were chosen as the means of achieving the relative motion between modules in order to locomote the serpentine robot.

Servo Selection

In order to determine which servo to use for the preliminary serpentine robot design, the main factors that were under consideration were overall volume, mass, torque, speed, and current consumption. It was decided to start by making the preliminary design as small as possible, which allows for expanding to larger servo motors and a larger robot overall while taking care of keeping the cost down. By searching several hobby shops and internet sites for the smallest servos available several choices were found: the Xiangyu xy-ms-3.7, the Xiangyu xy-ms-4.4, and the Hitec HS-55. The specifications of these servos are shown in Table 28.

Table 28 - Servo Specifications

Model	Supply Voltage (V)	Angular Velocity (rad/s)	Torque (kg-cm)	Operating Current (mA)	Idle Current (mA)	Volume (cm^3)	Mass (g)
Xiangyu xy-ms-3.7	4.8 – 6.0	17.5	0.4	100	1	2.82	3.7
Xiangyu xy-ms-4.4	4.8 – 6.0	17.5	0.6	100	1	3.14	4.4
Hitec HS-55	4.8 – 6.0	15.0	1.3	180	5.5	6.35	8

The two Xiangyu models are much smaller than the Hitec model; however the Hitec model did have a reasonably large amount of torque for its size. The amount of torque is mainly what contributes to the size and weight of a servo, and finding a servo with a good combination of high torque as well as small size and lightweight makes for a good design. In order to make the best decision several ratios were considered: torque-to-mass, torque-to-volume, and torque-to-operating current. The optimal servo would have high values for all of these ratios, since the tradeoffs for torque are mass, volume, and current consumption. The ratios for each of the servo models are shown in Table 29.

Table 29 - Servo parameter ratios

Model	**Torque/Mass**	**Torque/Volume**	**Torque/Operating Current**
Xiangyu xy-ms-3.7	0.108	0.142	0.004
Xiangyu xy-ms-4.4	0.136	0.191	0.006
Hitec HS-55	0.163	0.205	0.007

It can be seen that although the Hitec servo is larger and heavier than the two Xiangyu models, the amount of torque that the Hitec servo has balances the added volume and mass as well as the amount of current consumed by the servo when operating. For this reason, the actuation device chosen for the preliminary design of the serpentine robot is the Hitec HS-55, depicted in Figure 63, which has a cost of $14 each.

Figure 63 - Hitec HS-55 servo

http://www.hitecrcd.com

Note: Since making this decision, a new model has been released that advertises to have a higher torque (1.6 kg-cm), while being even more lightweight (7.4 g) and having less total volume (4.75 cm^3), the Futaba S3110. This may prove to be an even better choice for actuating the next generation of serpentine robots.

5.2.1.2 Multi-Stage Molded Structural Support

The role of the structural support is also important, as it is the part of the system that protects the other subsystems from damage, keeps the positions of the other subsystems stable, and also provides the surface that contacts the ground for motion. The standard approach used by other serpentine robot researchers such as those discussed in [Hiro93, Wors96, Dowl97, Gran05] is to make each module using some sort of metal frame, usually aluminum, connected by compliant joints or revolute joints, depending on the type of actuation system used. This is by no means the optimal solution because although aluminum is a low density metal, the design objectives can still be met using a polymer that has an even lower density. A polymer can provide enough stiffness to support all of the components as well as protect them from damage.

In addition to meeting the necessary structural requirements, a polymer support system has numerous manufacturing benefits. If a molding process is used, only one mold needs to be fabricated, and all of the modules can subsequently be processed in that mold. This greatly reduces the amount of time spent machining parts, which is a very good thing for a design which calls for many modules to be fabricated. Also, MSM can be used to fabricate the modules, allowing the entire module including the joints to be molded. This not only drastically reduces the manufacturing and assembly time, but it also reduces the cost significantly. Since the joints can be made out of the same material as the rest of the module there is a reduced part count as well as reduced expense from not having to buy a different material for the joints. This does not mean that a different material cannot be used for the joints, only that it is not necessary.

The MSM process in use for fabricating the structural support subsystem makes use of a thermosetting polyurethane material obtained from Innovative Polymers, Inc. The specific grade of polyurethane is IE-72 DC with the properties listed in Table 30.

Table 30 - Properties of Innovative Polymers, Inc. IE-72 DC

Parameter	Value	Test Method
Specific gravity	1.1	N/A
Hardness (Shore D)	80	ASTM D-2240
Tensile Strength (psi)	8000	ASTM D-638
Elongation @ Break	2%	ASTM D-638
Flexural Modulus (psi)	250000	ASTM D-790
Notched Izod (ft-lbs/in)	0.5	ASTM D-256
Linear Shrinkage (in/in)	0.004	ASTM D-2566

The structural support subsystem was designed and fabricated by Brent W. Spranklin [Spra06]. Molds were first modeled using the CAD software using Pro/Engineer and numerical codes were generated using the integrated CAM software, Pro/Manufacturing. The molds were made out of polyurethane tooling board purchased from Freeman Supply Company and manufacturing was completed using a 3-axis CNC mill, the Benchman XT.

The MSM process for this design requires three molds, one for each half of the module and one for the joint in between the halves. The main structural components of the design are molded in the first stage, shown in blue in Figure 64. Removable cores are placed in the mold to create a cavity to receive the universal joint in the second stage of the molding process. The side core is for aligning multiple structural components for connecting in series, a male end is included on the other half (not shown in figure).

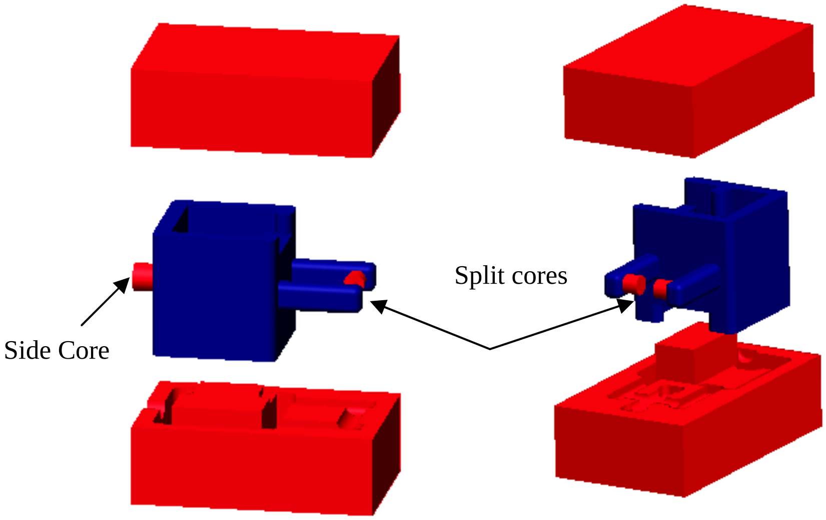

Figure 64 - Stage one, left and right halves [Spra06]

The second stage consists of connecting the two pieces from the first stage together in mold, so that a universal joint can be molded in place, shown in yellow in Figure 65. The shrinkage the polymer experiences during the curing process gives the joint enough clearance to rotate inside of the two larger structural components.

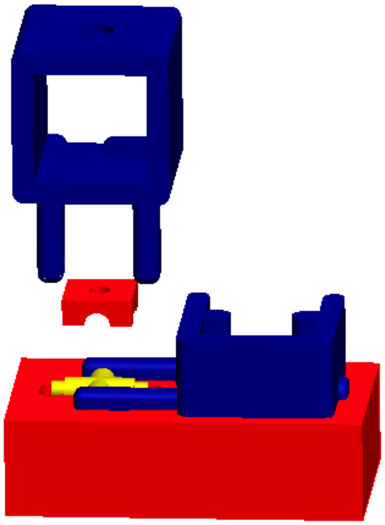

Figure 65 - Stage two, exploded view [Spra06]

5.2.2 Electrical System

For the preliminary design of the serpentine robot, it was decided that it was only necessary to actuate one servo for each module to achieve a forward rectilinear locomotion. Servos require two types of signals for operation, a power signal which is discussed in Section 5.2.2.1 , and a signal known as a pulse-width modulation (PWM) signal. There are pre-fabricated and pre-programmed controllers that generate PWM signals, such as the BASIC Stamp manufactured by Parallax, however it was determined that controllers such as this would drive up the cost, especially since one controller is required for each module. The alternative method of designing electronic circuitry is discussed in Section 5.2.2.2.

5.2.2.1 *Power Supply*

As discussed previously, the serpentine robot design objectives call for a modular and autonomous robot. This means that the power source for each of the modules must be on-board. Research was conducted on energy storage systems to find the optimal choice for supplying power the servos. As can be seen in Figure 66, for the mission time of approximately 30 minutes as stated in the design objectives, batteries and supercapacitors/ultracapacitors have the best combination of specific energy and specific power [Thom02, Thom04]. However, when also considering cost, batteries are the optimal choice because supercapacitors and ultracapacitors are relatively expensive. In addition, the mission time is at the upper limit for supercapacitors and ultracapacitors making them less applicable to the robot design.

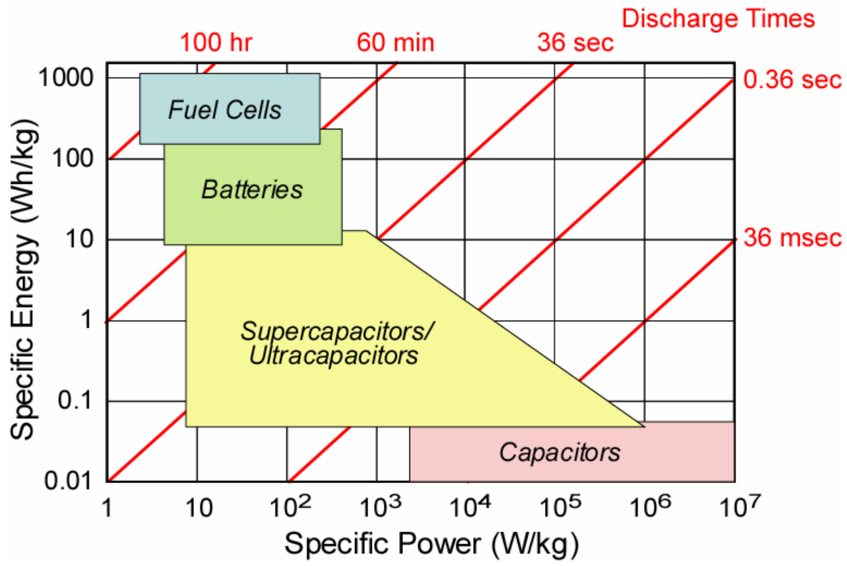

Figure 66 - Energy Storage Performance Data [Thom02, Thom04]

Battery selection is critical, since the weight, size, and storage capacity of the battery can determine how effective the entire robot will be. There are several types of batteries that are worth considering, including lead acid, nickel-cadmium, nickel-metal hydride, lithium-ion, and lithium-ion polymer all of which are secondary cells meaning they are capable of being recharged. The best way to compare these batteries is using a performance chart, shown as Figure 67, which depicts the amount of energy storage capability per unit mass against the energy storage capability per unit volume. The obvious choice is a lithium-ion or lithium-ion polymer because it has the best combination of energy storage capacity, size, and weight.

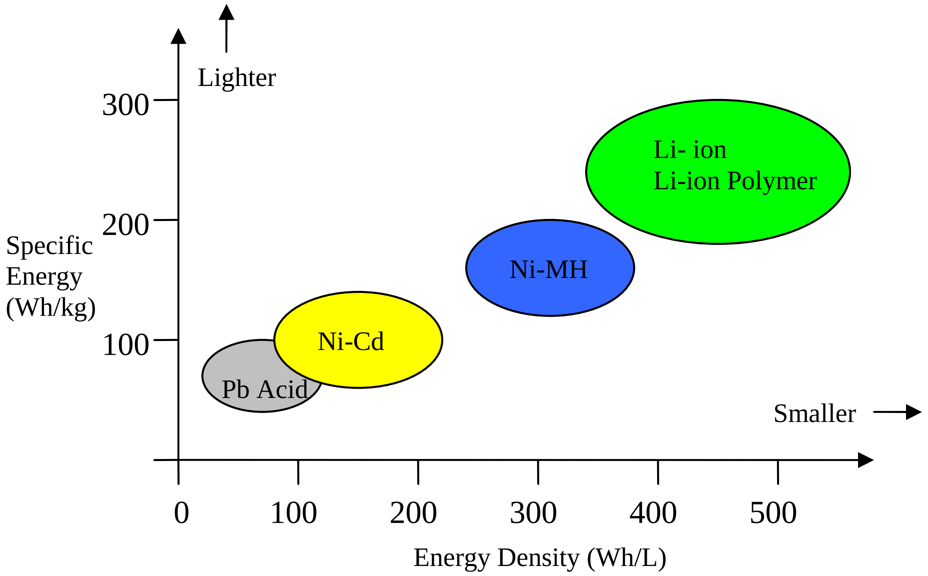

Figure 67 - Comparison of Battery Energy Densities [Thom02, Thom04]

Lithium-ion polymer batteries are characterized by their capacity and number of cells. Typical cell sizes produce 3.7 volts and can be placed in series or parallel depending upon the application. The capacity, measured in milliamp-hours (mAh), is the maximum amount of current that can be drawn from the battery in one hour. The servo requires at least 4.8 volts and draws current at 180 mA. This information along with the mission time of 30 minutes requires the battery for the serpentine robot to have a capacity of at least 90 mAh at 4.8 volts.

The Kokam 145-2S was determined to be the smallest available battery pack meeting the requirements. It consists of 2 cells in series, making it have a total capacity of 145 mAh at 7.4 volts, as shown in Figure 68. It measures only 30x19x9 millimeters, has a mass of only 9 grams, and costs $15.

Figure 68 - Kokam Lithium-ion Polymer Battery

http://www.fmadirect.com

5.2.2.2 Circuit Design

In order to generate the PWM signals that control the servo motors, a custom circuit was designed. It was decided to keep the circuit as simple as possible for the preliminary design, thereby only including what is necessary to control the servos and not implementing any sensors into the circuit design.

A schematic of the circuit is shown in Figure 69. The main components of the circuit include a voltage regulator, a microcontroller, a toggle switch, several capacitors, and a resistor. A National Semiconductor LM340 Series 3-pin positive voltage regulator takes the 7.4 volts from the battery and reduces it to 5.0 volts to supply the microcontroller as well as the servo. The voltage regulator specifications call for two capacitors, one 0.33 microfarad across the input and ground pins and one 0.10 microfarad capacitor across the output and ground pins.

An 8-pin Microchip 12F629 was selected as the microcontroller for several reasons. It has reprogrammable Flash-based memory, making it easier to write to the device using a development board attached to a personal computer. The microcontroller also has an internal oscillator for running the instruction set and has 2 timers, one 8-bit and one 16-bit, for generating the PWM signals. The microcontroller specifications also call for one 0.10 microfarad capacitor across the V_{SS} and V_{DD} pins. The other six pins can be used as either inputs or outputs.

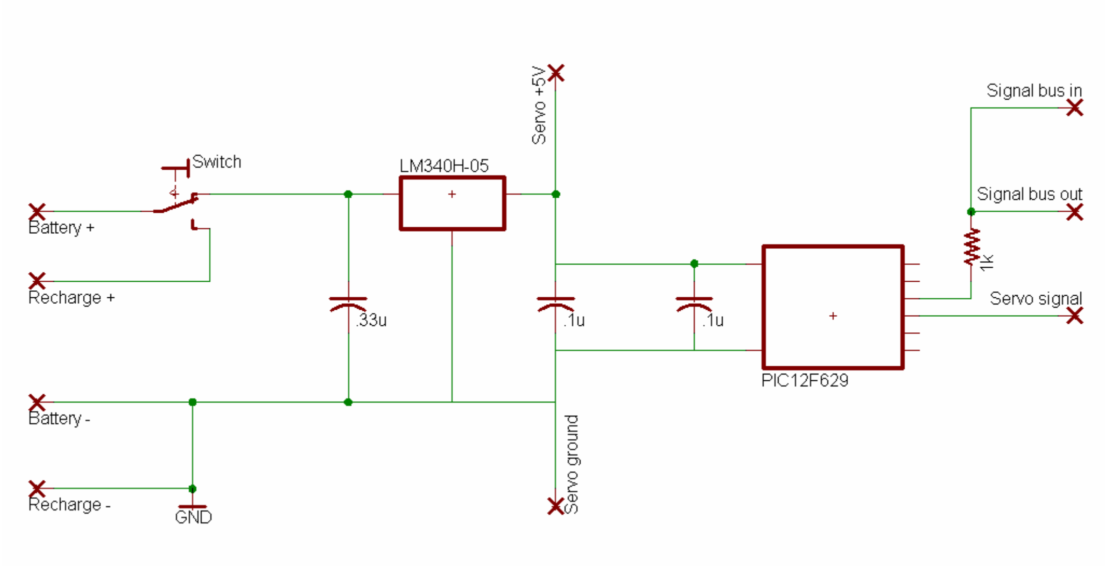

Figure 69 - Preliminary Circuit Design

The toggle switch is a single pole-double throw switch. The battery is connected to the common pole and the circuit is powered when the switch is thrown one way and to leads for recharging the battery when the switch is thrown the other way. The resistor is for dropping the voltage of the signal bus to protect the microcontroller. The signal bus is discussed in more detail in the Section 5.2.4.

The circuit board layout was designed using free software downloadable from the internet called Eagle Layout Editor, version 4.16, from Cadsoft USA. The layout was completed in conjunction with the specifications of the printed circuit board (PCB) manufacturer Advanced Circuits. The minimum size the manufacturer allows for a reduced "prototyping" price is 31.75 millimeters square. Using this size as a guideline, the circuit components were drawn to specification and placed in the PCB layout. Special attention must be paid to the layer of the circuit board, drill size, and trace wire size. The result of the PCB modeling effort is shown in Figure 70. The red traces are on the top layer and the blue traces are on the bottom layer. In this case the bottom layer was used as a ground.

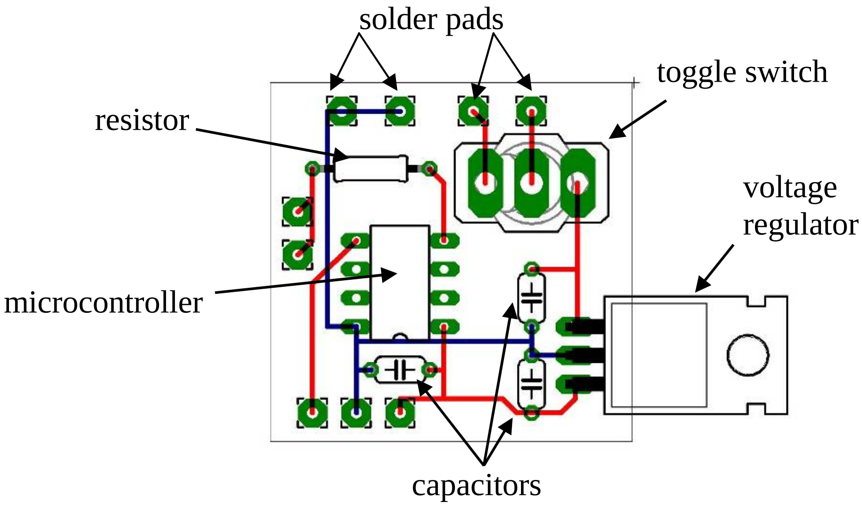

Figure 70 - Preliminary circuit board layout

Upon completion of the PCB layout, the appropriate files were generated using the Eagle CAM Processor. Advanced Circuits requires several files to fabricate the boards, including a drill file specifying the location of all of the holes, and a Gerber file for each layer which specifies the locations of the traces and solder pads. Once the files are uploaded to the Advanced Circuits website, the boards are fabricated using 2-layer, 0.062 inch thick FR-4. All of the traces and solder pads consist of a tin finish over 1 ounce copper.

Upon receipt of the PCBs, the components were soldered in place using Kester 44 rosin-core solder. Solid 22 gage insulated wires were attached to the solder pads along the perimeter for connecting the required inputs and outputs. A completed board is shown in Figure 71. The total cost of one circuit board with all components is approximately $13, most of which is from the cost of fabricating the board and the toggle switch.

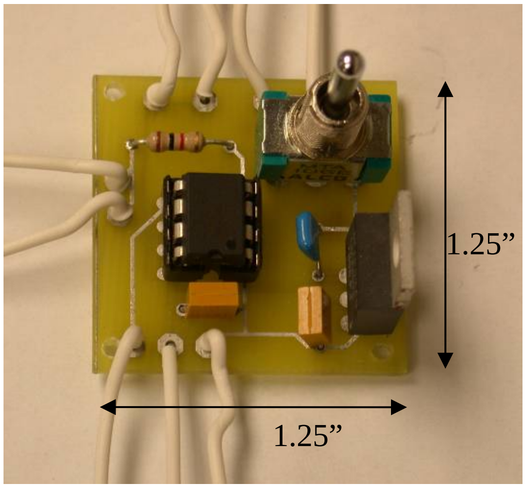

Figure 71 - Completed PCB with components

5.2.3 Assembly

Once all of the components were soldered to all of the boards, the boards could be installed into the structural modules. For this design, the boards and servo motors were secured to the structural members using screws and tie rods. Wire ties were used to secure the batteries in position as well as for joining the structural modules together. All of the ground wires were tied in together along with the bus input and output for each circuit. The bus allows for one switch to be used to control when the servos start even though each module has its own microcontroller and power switch. The completed serpentine robot with five modules in shown in Figure 72, with the total cost of each module being in the vicinity of $60, most of which is the cost of the battery and the two servo motors, which could be reduced if purchased in bulk.

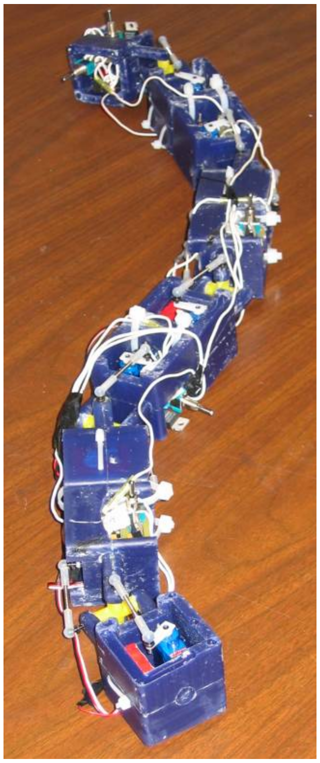

Figure 72 - Completed serpentine robot

5.2.4 Gait Implementation

The circuit discussed in the previous section is capable of delivering the PWM signal to the servos. This section discusses how the global motion is achieved and the microcontrollers were programmed in order to generate the appropriate PWM signals.

As discussed before, the global motion for this preliminary design is a vertical rectilinear gate. Previous work was completed by Merino and Tosunoglu [Meri04] which included a simple rectilinear gait that is easy to realize, shown in Figure 73.

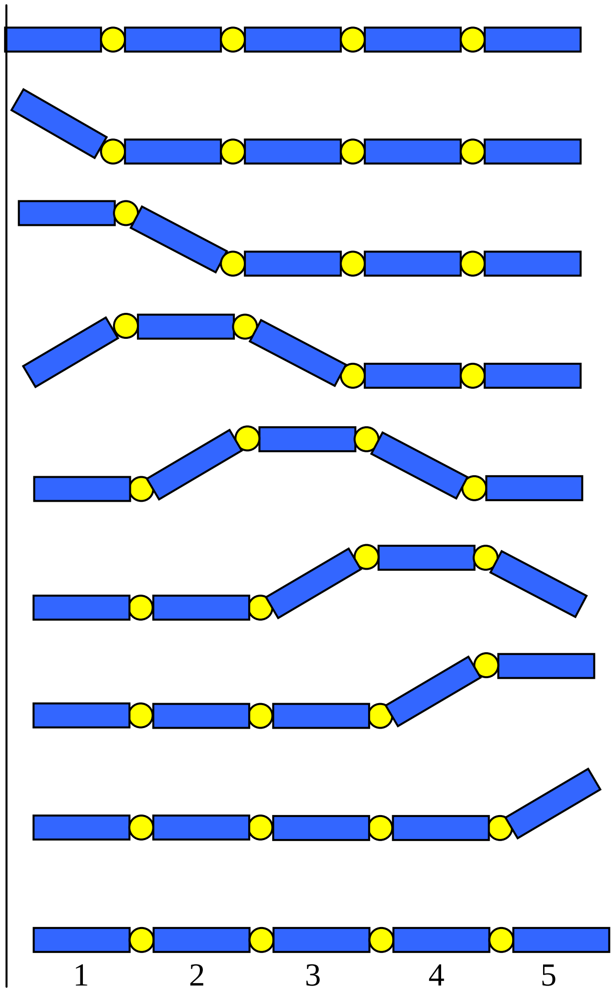

Figure 73 - Merino and Tosunoglu gait [Meri04]

As can be seen from Figure 73, a global horizontal motion can be achieved by propagating a wave through the length of the robot. This is accomplished by moving the links relative to each other at the appropriate instant in time.

As stated in Section 5.2.1.2, the each module contains a left half and a right half separated by a universal joint. There is a tie rod that connects the servo horn in one half to a spherical joint located on the other half. When the servo turns clockwise or counter-clockwise, the two halves are forced to rotate relative to each other about the universal joint. If it is considered that the servo starts centered when all of the links of the robot are flat on the ground, then each servo only needs to be programmed to go clockwise, back to center, counter-clockwise, and repeat at the appropriate time relative to the other servos.

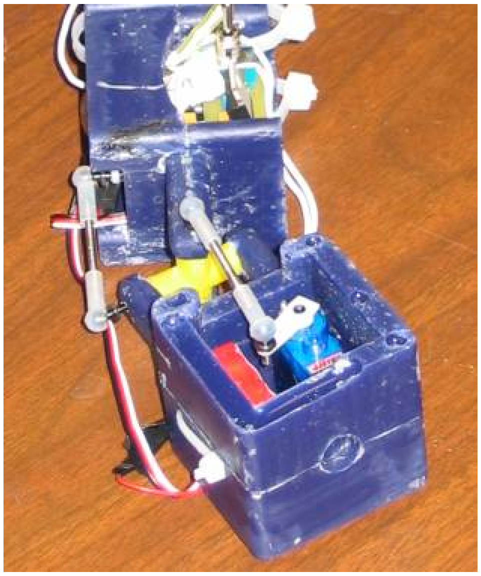

Figure 74 - Universal joint (yellow) and tie rods with spherical joints

Programming

The PIC12F629 was selected as the microcontroller to use for controlling the servo positions. The chip can be programmed with a variety of development boards and programming kits. For this project the Microchip PICKit 1 was used. Programs were written in assembly language using the manufacturer’s data sheet as a guide. The PIC12F629 has an internal 4 megahertz oscillator is capable of running the built-in timers, an 8-bit Timer0 and a 16-bit Timer1, at 1 megahertz.

In order to generate the PWM signals a method for having one of the input/output pins send the appropriate signal was devised. The timers run at a much faster pace than is necessary for communicating with the servo. The servos in use require a pulse with a 20 millisecond period as shown in Figure 75. The duration of the high voltage part of the pulse varies from 0.9 milliseconds to 2.1 milliseconds with 1.5 milliseconds being the center position for the servo.

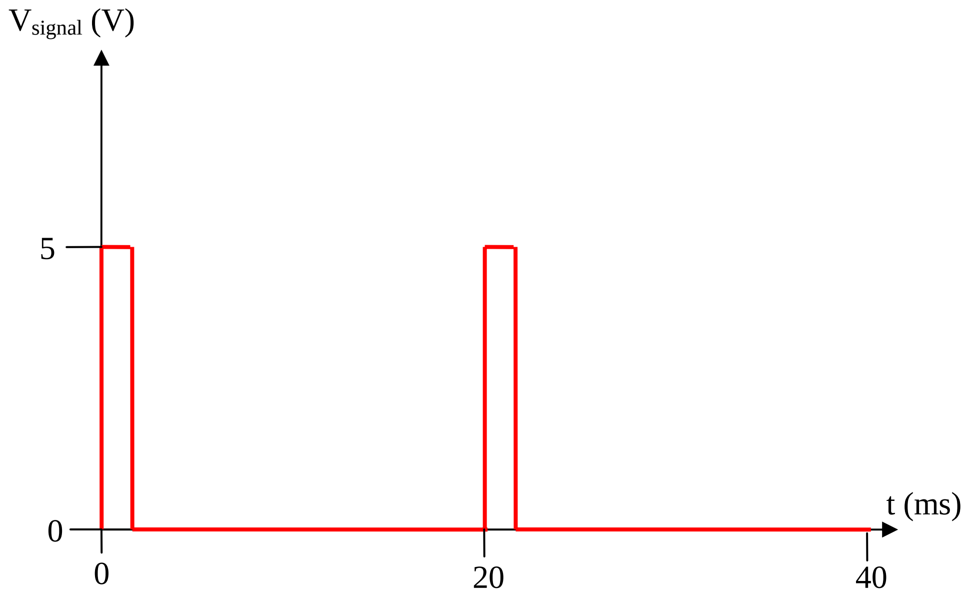

Figure 75 - PWM Signal

The code to achieve this sort of pulse essentially consists of four loops. There is an "on" loop, an "off" loop, a main loop, and a timing loop. When the program gets to the timing loop, it runs that loop for 100 microseconds before breaking. This amount of time is used to ensure that whole numbers are achieved for the on and off signals. For the center position, the "on" loop supplies the appropriate pin with +5 volts for 15 runs of the 100 microsecond timing loop. The off time is calculated depending on the on time supplied to the servo to ensure that the pulse period remains 20 milliseconds. The main loop ensures that the entire action is repeated in the appropriate manner that corresponds to the gait described above.

A digital video was taken and Figure 76 contains still shots from the video at three second intervals to show the motion of the serpentine robot on a flat surface such as a carpeted floor.

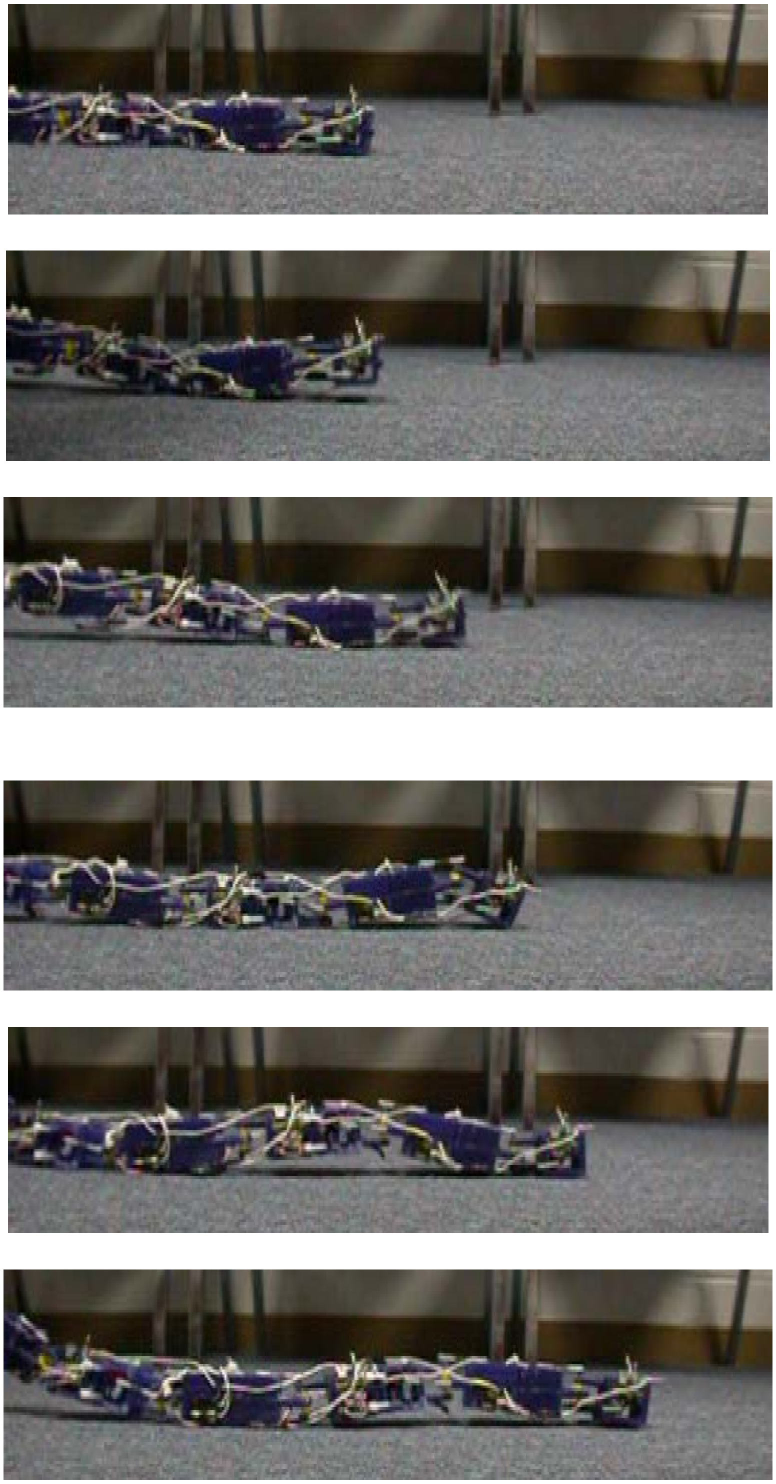

(a) t = 0 sec

(b) t = 3 sec

(c) t = 6 sec

(d) t = 9 sec

(e) t = 12 sec

(f) t = 15 sec

Figure 76 - Still shots of serpentine robot in motion

This work shows that it is possible to develop an affordable serpentine robot fabricated by a MSM process. The design makes use of a modular, multi-functional architecture that is scalable and does not require a large number of manufacturing steps as other serpentine robots have in the past. The gait was successfully implemented, and adding an additional degree of freedom for turning to avoid objects is merely a matter of reprogramming the circuitry since a second set of servos is already on-board.

5.3 Development of a Multi-Material Injection Molded Module with Embedded Electronic Components

This section addresses the robustness of a prototype MMIM module with embedded electronic components, which can be designed for applications such as the serpentine robot described in Section 5.2. These types of modules can eliminate the weaknesses in the design of such structural support subsystems because of the increased thermal and impact protection obtained from using MMM and embedded electronic systems.

5.3.1 Materials

As discussed in Section 3.1, MMM consisting of several stages is necessary in order to design modules with embedded electronic components for extreme environments because of the direct relationship between polymer strength and processing temperature. For this prototype module, a two-material system was selected to show the robustness of these types of multi-material configurations with embedded electronics.

The same circuit board, shown in Figure 71, that was designed for the serpentine robot was selected as a candidate circuit for embedding since all of the components were already on-hand. LDPE was selected as the first layer material because of its low processing temperature. The second layer material, ABS, was selected for its high impact strength. It is often necessary to determine the minimum thickness of the electronics protection layer, in order to prevent damage to the electronic components upon the injection of the second higher temperature layer. However, in this particular case, the amount of polymer for the first layer is constrained by the size of the circuit board, which a simple finite element thermal analysis confirmed was well beyond the minimum thickness necessary for shielding the heat when injecting the second layer.

5.3.2 Embedding of Electronic Components Using Multi-Material Injection Molding

Since the purpose of fabricating this prototype module was only to show the robustness of embedded electronics, it was decided that a spherical shaped module is the optimum choice because of the lack of sharp edges where stress concentrations could develop when subjected to extreme loading.

In order to create modules with embedded electronic components using an injection molding process, it is often necessary to add stages to the molding process to ensure the embedded electronic components remain in position. In the case of a sphere with a circuit board embedded in the center, one fabrication method consists of four stages, one stage for each hemisphere for each of the layers.

The first stage mold, shown in Figure 77 is by far the most difficult to produce. One half of the mold consists of a hemispherical cavity with two holes. One hole is located in the center of the cavity, serving as the injection location, while the other hole must be properly positioned to allow for the toggle switch to protrude. A piece of polyvinyl chloride tubing the same size as the hole is placed around the toggle switch to provide a seal to prevent any polymer from entering the switch and causing an open circuit. The other half of the mold must be machined to the size and shape of the circuit board while also having traces milled in allowing for a tight seal around the protruding power and signal wires.

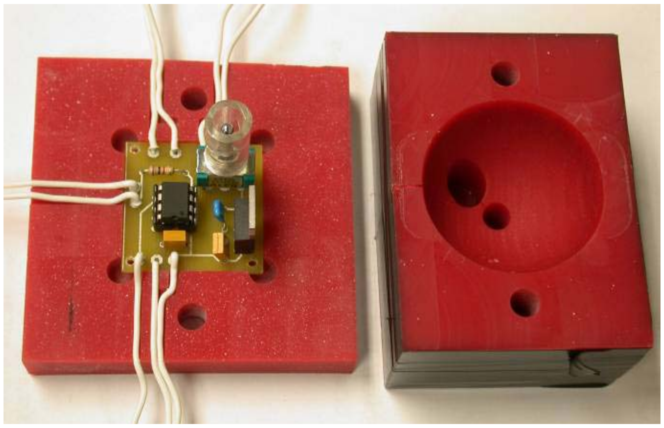

Figure 77 - Circuit board and first stage mold

The second stage mold is similar to the first stage except that both mold halves must be hemispheres. One hemisphere is to hold the part that was molded in the first stage, in this case the cavity half of the first stage mold was used to keep mold tooling to a minimum. The second stage cavity is does not need to have the second hole for the toggle switch since the other side of the circuit board is completely flat. This mold half must have traces milled in to allow for a tight seal around the protruding wires. Figure 78(a) shows the first layer of the spherical module with embedded circuit board along with the second stage mold. Figure 78(b) shows another view of first layer of the module. The protrusions caused by the corners of the circuit board were cut off prior to proceeding to the third stage.

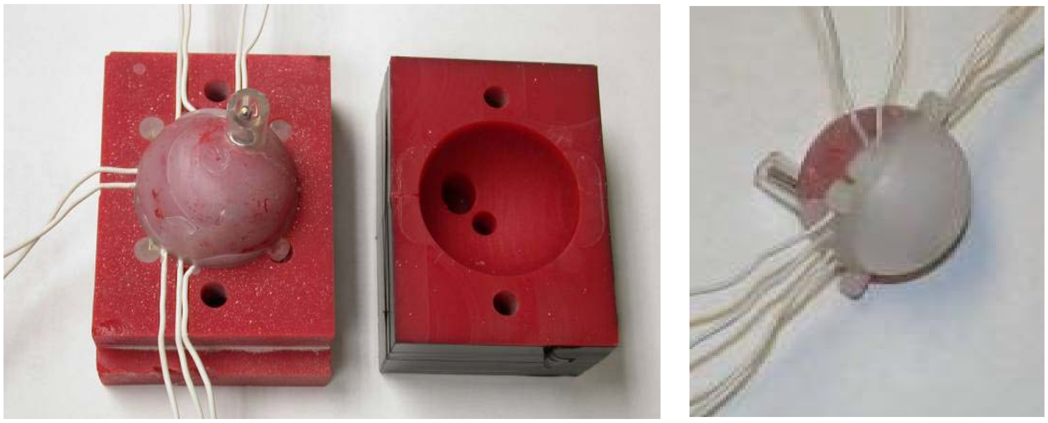
(a) (b)

Figure 78 - (a) completed second stage part and mold, (b) completed part, bottom view

The third and fourth stages are quite similar to the second stage except that larger hemispherical cavities are used to allow for the first layer to be overmolded. The same mold that is used in the second stage for holding the first stage part can also be used in the third stage to hold the second stage part. This allows for the first layer of the module to be appropriately centered enabling a more uniform thickness of the second layer. In a similar manner, the third stage cavity can be used in the fourth stage to hold the part. The final, two layer spherical module prototype with embedded circuit board is shown in Figure 79.

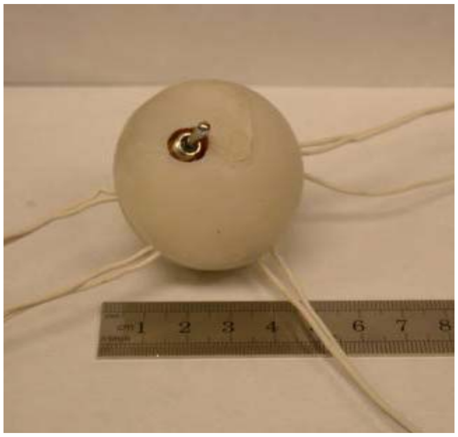

Figure 79 - Completed part; fully embedded circuit board

5.3.3 Thermal, Impact, and Static Load Testing of Module with Embedded Component

In order to demonstrate the robustness of the module, it was subjected to three tests that were designed to replicate the possible extreme loading conditions to which a search and rescue reconnaissance robot might be subjected. The three tests include a thermal test, an impact test, and a compression test.

The first test was designed to mimic a situation in which the robot enters an environment with fire nearby. Although the melting temperature of the outer layer of the module is approximately 250ºC, it was decided that it should be able to be subjected to this temperature for a short time without losing any functionality of the electronic parts. A furnace was heated to 250ºC and the structure was placed in the furnace and heated for 30 seconds and then removed. Some minor melting occurred to the outer surface, but it was only superficial. The electronic circuitry was then tested to ensure it was still functional.

The second test was much more extreme. An impact test was devised to replicate many of the hazardous conditions that may be experienced on a search and rescue mission, such as falling debris or missing floor sections. The drop height was just over 6.7 meters (22 feet), which gives an impact velocity of approximately 11.5 meters per second (37.6 feet per second) if air resistance is neglected. Figure 80 shows still shots taken from a digital video of one of the drop tests. The red string in the images of Figure 80(b), (c), and (d) was used for measuring purposes and was not touching the structure at all. Five drop tests were completed overall, all from the same height. After the fifth test, the prototype began to form a crack at the interface between the third and fourth stage shots, but the electronic components remained functional as is shown by the moving servo horn the long exposure image in Figure 81 .

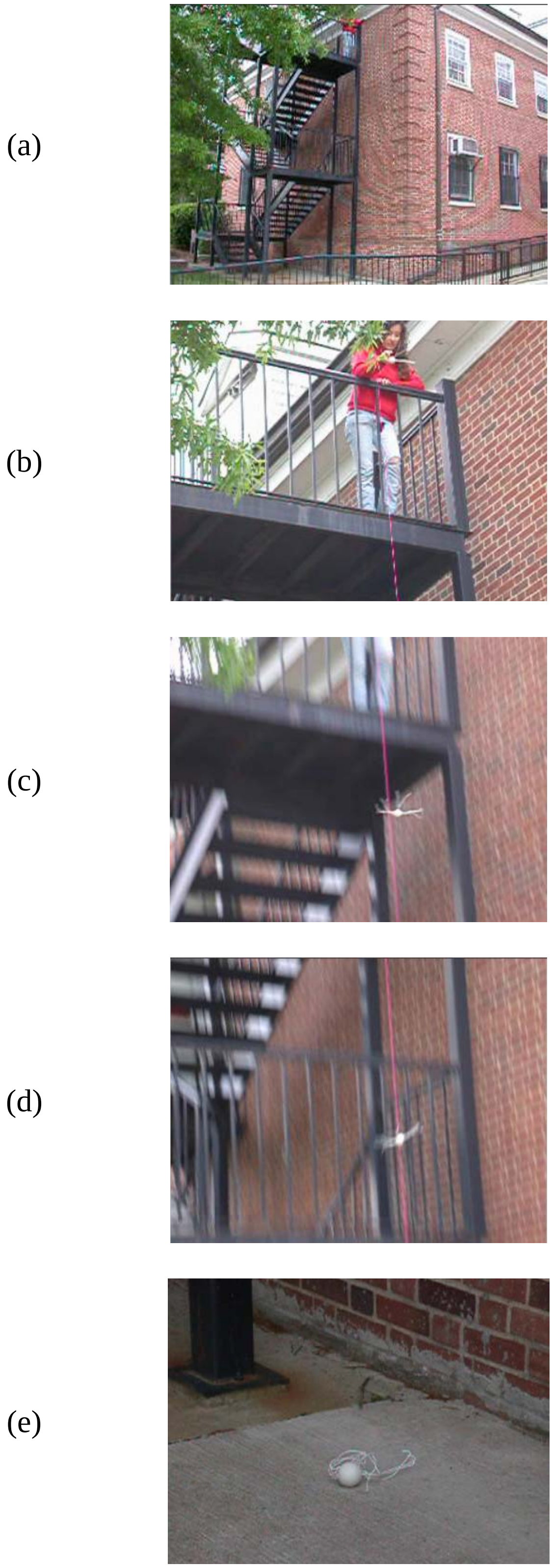

Figure 80 - Still shots of embedded circuit board drop test

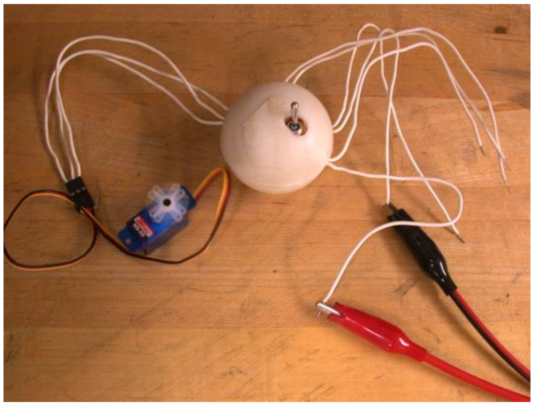

Figure 81 - Spherical multi-material structure after drop tests

Although the module did appear to function after the impact test, it should be noted that this does necessarily mean that no damage was sustained to the electronic circuit or components. The impact shock of a drop test can cause the brittle interfaces of a circuit to crack or come loose. This may go unnoticed as the components are still making contact and the device still functions at first, however if it runs for a long time or experiences a thermal load, the device could stop functioning because the crack between circuit interfaces opened enough to cause an open circuit. Since it does not happen immediately, it often is not realized that the impact is the cause of failure.

The final test was a compression test where the spherical module was placed in one of the mold halves to prevent slippage and then subjected to a load of approximately 0.5 metric tons (1100 pounds) using a hydraulic press as shown in Figure 82. At this pressure, the module experienced a very large deformation at the point of load application. This deformation can be seen in Figure 83(a), which resulted in permanent deformation, shown in Figure 83(b), which is also a long exposure image to shows that the embedded electronic components still work properly.

Figure 82 - Spherical multi-material structure during compression test

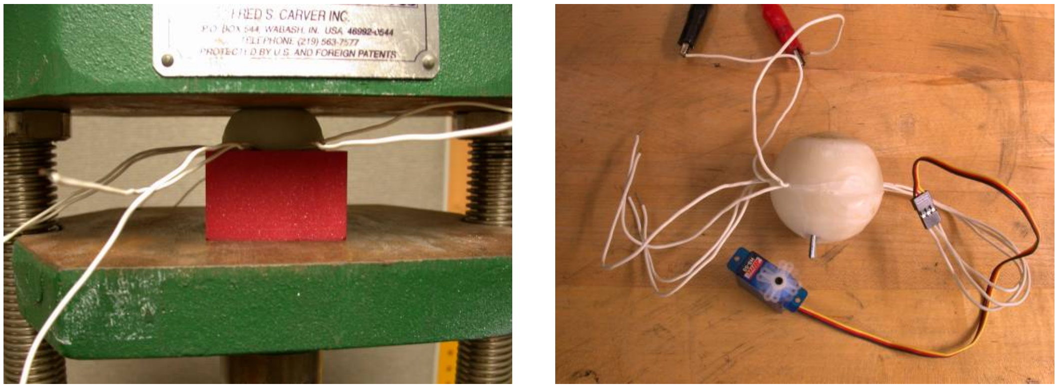

(a) (b)

Figure 83 - Spherical multi-material structure: (a) large deformation during testing, (b) functioning properly after testing, permanently deformed

5.4 Conclusions and Contributions

The main concepts addressed in this chapter were to show that it is possible to develop affordable, mass producible multi-functional modules with embedded electronic components fabricated by a MMIM process. First, the design and fabrication of a serpentine robot prototype using a MSM process were discussed and some design guidelines for actuation, and power supply were developed. The fabrication of a multi-material spherical module with embedded electronic components was also discussed, and it was shown that this prototype module can withstand several different types of loading including thermal and mechanical loads that would most likely destroy unprotected electronic components.

Chapter 6: Conclusions and Future Work

This work characterizes and models many thermal and thermomechanical effects caused by using MMM processes and embedded electronic components which had not previously been done. The main contributions of the work are as follows:

1. For the first time, the thermal conductivities of MMIM interfaces were characterized, resulting in the addition of a correction term to the standard ROM model to account for the decrease in thermal conductivity observed.

2. It has been shown that using the thermal conductivity results in homogenized analytical models will result in accurate predictions of the transient thermal response of MMIM modules in elevated ambient temperatures below the melting point of the polymers. Alternatively, simpler exponential formulas can be fitted to experimental data to describe the transient thermal response.

3. It has been shown that a finite element model is necessary and sufficient to accurately predict the transient thermal response of MMIM modules in elevated temperatures above the melting point of the polymers.

4. For the first time, an open mold experiment based on the DIC technique has been developed for characterizing the thermomechanical strains associated with polymer shrinkage during molding processes.

5. For the first time, a thermomechanical expansion has been observed for a polymer during the change from a liquid to a solid, which affects the way that the polymer behavior will be modeled in the future.

6. It has been shown that the altering mold friction, embedding components, as well using multiple materials will cause anisotropic thermomechanical behavior during polymer shrinkage.

7. It has been shown that a thermomechanical finite element model can be used to accurately predict the thermomechanical displacements during processing of MMIM modules as well as when embedded electronic components dissipate heat.

8. It has been shown that a prototype multi-functional MMIM module for a serpentine robot can be designed and fabricated to withstand high temperatures, impact, and high compressive loads.

The following sections discuss the conclusions and contributions in the areas of thermal and thermomechanical behavior for MMM modules in more detail, as well as the application of this knowledge to the development of multi-material serpentine robots with embedded electronics along with suggestions for future work in these areas.

6.1 Thermal Characterization and Modeling of Multi-Material Molded Modules

Experiments were designed to measure the effect of the MMIM process on the steady-state thermal conductivity of different polymer systems. In addition, a contribution was made from the measurements in the form of a correction term that can be applied to the standard ROM model for thermal conductivity to account for the multi-material interface. The characterization effort determined that the effect of adhesion plays the largest role in predicting the performance of a MMIM module. It was concluded that using a MSIM process results in interfaces with better heat conduction than the ROM values that are achieved when the interface is created by placing discrete layers together.

A set of transient thermal experiments was conducted and the effects of increased ambient temperatures were characterized for the core of homogeneous and heterogeneous injection molded spherical modules. Using the results of these experiments along with the thermal conductivity measurements performed in the steady-state aided in the development of modeling contributions in the form of homogenized analytical models, an exponential fit formula, and a finite element model. The analytical model and exponential fit, calibrated with homogeneous specimens, are capable of predicting the heterogeneous modules with an extremely high degree of accuracy for ambient temperatures under the melting temperatures of the polymers. Above and below the melting temperatures, a finite element model modified to include the change in thermal properties associated with the phase change from a solid to a liquid has been shown to provide extremely accurate predictions of the thermal response. The high correlation values achieved in the modeling effort provide a basis for more complex models to be developed in the future in the area of MMIM modules for biologically-inspired and multi-functional structures.

6.2 Thermomechanical Characterization and Modeling of Multi-Material Molded Modules with Embedded Electronic Components

For the first time, experiments based on the DIC technique were developed for characterizing the thermomechanical strains associated with polymer shrinkage during molding processes. In-mold cooling experiments were conducted to analyze the thermomechanical behavior of homogeneous and heterogeneous material modules. While viscoelastic effects were neglected, it was observed that there is a 35 percent decrease in strain magnitude upon a cooling polymer changing phase in-mold. The effects of friction were characterized, and it was concluded that the overall strain is reduced by approximately 60 percent when a mold release agent is not applied to the mold prior to processing. The change in the strain fields associated with the addition of a stiff, cylindrical electronic component were analyzed and increased positive strains in the transverse direction and decreased shrinkage in the axial direction were observed. Upon changing the material distribution from homogenous to heterogeneous, the effects of friction and embedding components are dominated by the large strains at the interface between the materials.

In addition to the described characterization contribution, another contribution was made in the form of a thermomechanical finite element model. Utilizing the results of the DIC characterization, an apparent CTE was defined and calculated by a MATLAB code that aided in the development of a finite element model to represent the in-mold cooling experiments. Correlation of the results from the thermomechanical finite element model with experimental measurements showed that the thermomechanical response of homogenous and heterogeneous modules with and without embedded electronic components can be predicted with a reasonable amount of accuracy both during processing and operation of the embedded components.

Another characterization effort was performed concerning the heat generation caused by the operation of embedded electronic components utilizing a surrogate heating element. Again the DIC technique was used to measure the strain fields associated with the thermomechanical response of the homogeneous and heterogeneous material distributions when the embedded heating elements are dissipating heat. The results of the analysis indicate that for the homogeneous cases the strains exist only in the regions near the heating element. The effect of a heterogeneous distribution of material is quite pronounced, the strains are no longer only in the regions near the heating element, but also are significant in the interface region between the materials.

Finalizing the thermomechanical contributions, a finite element model was developed to represent the embedded heating element experiments. This model includes two parts. The first part consists of a transient thermal analysis which makes use of the data from the steady-state thermal conductivity measurements to calculate a temperature profile at a certain time of interest. The second part of the model is a static analysis that uses the apparent CTE from the in-mold cooling characterization in addition to the temperature profile from the first part of the model to calculate the thermomechanical response. This model shows that the thermomechanical response of homogeneous and heterogeneous modules with embedded heating elements can be reliably predicted provided the correct material parameters are used as inputs.

6.3 Multi-Stage Molded Modules for a Serpentine Robot

The main concepts addressed in Chapter 5 show that an affordable, autonomous serpentine robot with modular architecture can be developed using MSM. Contributions of the form of design guidelines for future serpentine robots were established. The fabrication of a prototype MMIM spherical module with embedded electronic components was also discussed, and the robustness of such a structure to thermal, impact, and compressive loading was presented. Combining the contributions into an actual MMIM serpentine robot with fully embedded electronic components is left for future work.

6.4 Recommendations for Future Work

Since the work presented in this thesis is somewhat groundbreaking, as there has been no previously published work that deals with the effects of the MMM process on the thermal and thermomechanical properties of the resultant material system nor has any work been published regarding the robustness of fully embedded electronics for use in biologically-inspired and multi-functional designs, there is a considerable amount of future research that can be conducted. Some primary scientific and technical issues that should be addressed in the near future include the following:

1. Development of steady-state and transient thermal and thermomechanical principles from the model in Chapters 3 and 4 to govern the control of heat conduction across MMM interfaces and the design of MMM modules with embedded electronic components.
2. Designing a new version of the prototype multi-functional MMM modules presented in Chapter 5 with optimal thermal and thermomechanical performance using these principles.
3. The development of serpentine robots from the optimized multi-functional MMM modules.

These issues will now be discussed in more detail.

6.4.1 Future Work – Thermal Principles

The steady-state thermal conductivity measurement work that was completed in Chapter 3 only addressed three materials, LDPE, PS, and ABS. Obviously, there are many more material systems that are left to be characterized. In addition, if the experiments were completed on an injection molder that was set up specifically for MMM, then the material systems would be more closely matched with what would be achieved if they were mass produced. Also, there are different levels of adhesion to be explored other than what was analyzed in this work, which could further validate the results presented here.

The transient thermal modeling work discussed in Chapter 3 resulted in very good correlation with the experimental data, hence there is not much room for improvement for the case of the multi-material spherical module, but research could be further extended to include different, possibly more complex geometries. The finite element model developed that incorporates the temperature dependent behavior could be improved upon provided all of the appropriate data is available, such as temperature dependence of the thermal conductivities, densities, and specific heats of the materials.

6.4.2 Future Work – Thermomechanical Principles

In the area of the thermomechanical analysis there is much work to do in order to have a complete understanding of the nature of how the strains develop. The drastic change in strain magnitude that was apparent in all of the explored in-mold cooling cases could definitely use further explanation requiring more experiments. There are several ways upon which the heterogeneous thermomechanical experiments can be expanded. Recall that the ABS had to be melted prior to the LDPE, which is actually opposite of how the materials would be applied for embedded electronics applications. In addition, although the ABS was taken to temperatures above its melting point and became compliant, it requires pressure in order to flow in the same manner as the LDPE. An experiment that enables the measurement of the displacements in-mold during the MMIM process would be ideal for further validating the characterization presented in this work, because the appropriate pressure could be applied as well as the correct order of polymer processing.

Future work could also be completed to better understand the how embedded electronics are affected by the multi-material system cooling around them. The work in Chapter 4 was mainly concerned with how the material moves with respect to the embedded component, which was stiff and fixed in the mold. When actually embedding circuits that include a board and many components, the effect of the molding process on the circuit can play a major role in the life expectancy of the electronic components if there is much deformation of the board or component leads.

The thermomechanical finite element modeling in general could be further explored to obtain results that correlate better with the experimental data, especially in the case of the heterogeneous material distributions and the high friction distributions. If the frictional forces are known, then it may be possible to develop a model to account for the friction coefficient rather than using the apparent CTE as was completed in this work. Also, the heterogeneous material distribution results could be improved upon if a method for modeling the interface is developed that does not result in singularities when solving the model.

6.4.3 Future Work – Multi-Material Structures and Embedded Electronics

The main area of future work involves the work completed in Chapter 5. Although a cost effective, autonomous serpentine robot was fabricated by a MSM process, secondary operations were used to fasten the circuit boards, batteries, and servos to the structure. It was shown that it is possible to embed the delicate circuitry using a MMIM process, subject the structure to harsh loading conditions and still have functioning electronics, however the two concepts have not yet been combined to fabricate a serpentine robot from a multi-functional MMIM module. The design of such a robot could be further augmented by using the thermomechanical models developed in Chapters 3 and 4 to optimize the modules for the best thermal and thermomechanical performance based on the design requirements.

Another area of future work involves the reliability and survivability of MMIM modules with embedded components. It has been suggested that MMIM modules will be able to withstand environments and conditions that are much more severe than traditionally designed robotic modules. This claim can be further proven by experiments similar to those used for product testing. Accelerated life testing should be completed on MMIM modules with embedded components to determine how thermal and mechanical loading influences the functionality of the modules. In addition, the reliability of the electronic circuits alone should be tested under these same conditions to show that the using MMIM does increase the survivability without affecting the reliability or functionality of the electronic circuits.

References

[ASTM99] ASTM, Designation E1530 – 99. “Standard Test Method for Evaluating the Resistance to Thermal Transmission of Materials by the Guarded Heat Flow Meter Technique.” *Annual Book of ASTM Standards*. Vol. 04.06.

[Beck92] Beck, J.E. *et al.* 1992. “Manufacturing Mechatronics Using Thermal Spray Shape Deposition.” *Solid Freeform Fabrication* Symposium. The University of Texas at Austin.

[Binn95] Binnard, M. 1995. “Design of a Small Pneumatic Walking Robot.” MS Thesis, Massachusetts Institute of Technology.

[Bord91] Borden, T. 1991. "Shape-Memory Alloys: Forming a Tight Fit." *Mechanical Engineering*. Vol. 113, iss. 10, pp. 67-72.

[Bran99] Branch, M.A., Coleman, T.F, and Li, Y. 1999. "A Subspace, Interior, and Conjugate Gradient Method for Large-Scale Bound-Constrained Minimization Problems," SIAM Journal on Scientific Computing, Vol. 21, Number 1, pp. 1-23.

[Bruc89] Bruck, H.A. *et al*. 1989.“Digital image correlation using Newton-Raphson method of partial differential correction.” *Experimental Mechanics*. Vol 29, pp. 261-267.

[Bruc02] Bruck, H.A., Moore, C.L., and Valentine, T. 2002. “Repeatable Bending Actuation in Polyurethanes Using Opposing Embedded One-way Shape Memory Alloy Wires Exhibiting Large Strain Recovery.” *Smart Materials and Structures*. Vol. 11, pp. 509-518.

[Bruc04] Bruck, H.A., Fowler, G. Gupta, S.K., and Valentine, T. 2004. “Using geometric complexity to enhance the interfacial strength of heterogeneous structures fabricated in a multi-stage, multi-piece molding process.” *Experimental Mechanics*. Vol 44, iss. 3, pp. 261-271.

[Bush96] Bushko, W.C. and Stokes V.K. 1996. “Solidification of Thermoviscoelastic Melts. Part 4: Effects of Boundary Conditions on Shrinkage and Residual Stresses.” *Polymer Engineering and Science*. Vol 36, iss. 5.

[Cham99] Cham, J.G. *et al*. 1999. “Layered Manufacturing with Embedded Components: Process Planning Considerations.” *Proc. DETC99: 1999 ASME Design Engineering Technical Conference.* Las Vegas, NV.

[Chen05] Chen, J.L. *et al.* 2005. “Two-step digital image correlation for micro-measurement.” *Optics and Lasers in Engineering*. Vol. 43, iss. 8, pp. 836-846.

[Cresp05] Crespi, A., *et al.* 2005. “AmphiBot I: an amphibious snake-like robot.” *Robotics and Autonomous Systems.* Vol. 50, iss. 4, pp. 163-175.

[Daws05] Dawson, A. *et al*. 2005. “Thermal conductivity of polymer melts and implications of uncertainties in data for process simulation.”

[deBl98] de Blonk, B.J. and Lagoudas, D.C. 1998. “Actuation of Elastomeric Rods with Embedded Two-way Shape Memory Alloy Actuators.” *Smart Materials and Structures*. Vol. **7**, pp. 771-783.

[Dela00] Delaunay, D. and Le Bot, P. 2000. “Nature of Contact Between Polymer and Mold in Injection Molding. Part II: Influence of Mold Deflection on Pressure History and Shrinkage.” *Polymer Engineering and Science*, Vol 40, iss. 7.

[Dowl97] Dowling, K. 1997. “Limbless locomotion: learning to crawl with a snake robot. Ph.D. thesis, Robotics Institute, Carnegie Mellon University, Pittsburgh, PA.

[Egan96] Egan, E. and Amon, C.H. 1996. “Cooling Strategies for Embedded Electronic Components of Wearable Computers Fabricated by Shape Deposition Manufacturing.” *I-Therm ’96, IEEE InterSociety Conference on Thermal Phenomena*, Orlando, FL, pp. 13-20.

[Egan00] Egan, E. and Amon, C.H. 2000. “Thermal Management Strategies for Embedded Electronic Components of Wearable Computers.” *Journal of Electronic Packaging*. Vol. 122, iss. 2, pp. 98-106.

[Good02] Goodship, V. and Love, J.C. 2002. Multi-Material Injection Molding. ChemTec Publishing.

[Gran05] Granosik, G., Hansen, and Borenstein, J. 2005 “The OmniTread Serpentine Robot for Industrial Inspection and Surveillance.” *International Journal on Industrial Robots, Special Issue on Mobile* Robots. Vol. IR32-2, pp. 139-148.

[Gray50] Gray, J. and Lissmann, H. 1950. “The kinetics of locomotion of the grass-snake.” *Journal of Experimental Biology*. Vol. 26, iss. 4, pp. 354-367.

[Han97] Han, S. and Wang, K.K. 1997. “Shrinkage prediction for slowly crystallizing thermoplastic polymers in injection molding.” *International Polymer Processing*. Vol. XII.

[Heis04] Heiser, J.A. and King, J.A. 2004. “Thermally conductive carbon filled nylon 6,6.” *Polymer Composites*. Vol. 25, iss. 2, pp. 186-193.

[Helm96] Helm, J.D., McNeill, S.R., and Sutton, M.A. 1996. “Improved three-dimensional image correlation for surface displacement measurement and strain analysis.” *Optical Engineering*. Vol. 35, pp. 1911-1920.

[Hiro93] Hirose, S. 1993. Biologically Inspired Robots: Snake-Like Locomotors and Manipulators. Oxford University Press.

[Incr02] Incropera, F.P. and DeWitt, D.P. 2002. Fundamentals of Heat and Mass Transfer. Fifth Ed. John Wiley & Sons, Inc.

[Jans96] Jansen, K.M.B. and Titomanlio, G. 1996. “Effect of Pressure History on Shrinkage and Residual Stresses-Injection Molding With Constrained Shrinkage.” *Polymer Engineering and Science*. Vol 36, iss. 15.

[Jans98] Jansen, K.M.B, Van Dijk, D.J., and Husselman, M.H. 1998. “Effect of Processing Conditions on Shrinkage in Injection Molding.” *Polymer Engineering and Science*. Vol 38, iss. 5.

[Klaa99] Klaassen, B. and K.L. Paap. 1999 “GMD-SNAKE2: A Snake-Like Robot Driven by Wheels and a Method for Motion Control.” *IEEE International Conference on Robotics and Automation*. Vol. 4, pp. 3014-3019.

[Kram05] Kramschuster, A. *et al.* 2005. “Quantitative Study of Shrinkage and Warpage Behavior for Microcellular and Conventional Injection Molding.” *Polymer Engineering and Science*.

[Kwon05] Kwon, Isayev, K.A.I., and Kim, K.H. 2005. “Toward a Viscoelastic Modeling of Anisotropic Shrinkage in Injection Molding of Amorphous Polymers.” *Journal of Applied Polymer Science*. Vol. 98, pp. 2300–2313.

[Kuma02] Kumar, M. and Gupta, S.K. 2002. “Automated design of multi-stage molds for manufacturing multi-material objects.” *Journal of Mechanical Design*. Vol. 124, iss. 3, pp. 399-407.

[Lago93] Lagoudas, D.C. and Tadjbakhsh, I.G. 1993. "Deformations of Active Flexible Rods With Line Actuators." *Smart Materials and Structures*. Vol. 2, pp. 71-81.

[Li03] Li, X. and Gupta, S.K. 2003. “Manufacturability analysis of multi-material objects molded by rotary platen multi-shot molding process.” In *ASME International Mechanical Engineering Congress and Exposition*, Washington, DC.

[Li04a] Li, X. and Gupta, S.K. 2004. “A step towards automated design of index-plate multi-shot molds.” In *Tools and Methods of Competitive Engineering Conference*, Lausanne, Switzerland.

[Li04b] Li, X. and Gupta, S.K. 2004. “Geometric Algorithms for automated design of rotary-platen multi-shot molds.” *Computer Aided Design*. Vol. 36, iss. 12, pp. 1171-1187.

[Liao04] Liao, S.J. *et al.* 2004. “Optimal Process Conditions of Shrinkage and Warpage of Thin-Wall Parts.” *Polymer Engineering and Science*. Vol 44, iss. 5.

[Liss50] Lissmann, H. 1950. “Rectilinear locomotion in a snake (Boa occidentalis).” *Journal of Experimental Biology*. Vol. 26, iss. 4, pp. 368-379.

[Luo93] Luo, P.F. *et al.* 1993 “Accurate measurement of three-dimenisonal deformations in deformable and rigid bodies using computer vision.: *Experimental Mechanics*. Vol. 33, pp. 123-132.

[Ma01] Ma, S. Li, J., and Wang, Y. 2001. “A simulator to analyze creeping of a snake-like robot.” *Proc. IEEE International Conference on Robotics and Automation*. pp. 3656-3661.

[Meri04] Merino, C. and Tosunoglu, S. 2004. “Design of a crawling gait for a modular robot.” *Proceedings of the 17th Florida Conference on Recent Advances in Robotics*, May 6-7, Orlando, FL.

[Moon01] Moon, B. 2001. “Snake Locomotion.” University of Louisiana at Lafayette. http://www.ucs.lousiana.edu/~brm2286/locomotn.htm

[Mori01] Mori, M. and S. Hirose. 2001. “Development of active cord mechanism ACM-R3 with agile 3D mobility.” *Proc. of the IEEE/RSJ*

International Conference on Intelligent Robots and Systems. Maui, HI, pp. 1552-1557.

[Nils98] Nilsson, M. 1998. "Snake Robot Free Climbing." *IEEE Control Systems*. Vol. 18, iss. 1, pp. 21-26.

[NRC04] National Research Council. 2004. "Review of NASA's Aerospace Technology Enterprise: An Assessment of NASA's Aeronautics Technology Programs." *National Academies Press*. Washington, DC.

[Pont04] Pontes, A.J. and Pouzada, A.S. 2004. "Ejection Force in Tubular Injection Moldings. Part I: Effect of Processing Conditions." *Polymer Engineering and Science*. Vol 44, iss. 5.

[Reck06] Recktenwald, G. 2006. "Transient, One-Dimensional Heat Conduction in a Convectively Cooled Sphere." http://web.cecs.pdx.edu/~gerry/epub/

[Ryhä99] Ryhänen, J. 1999. "Biocompatibility evaluation of nickel-titanium shape memory metal alloy" Academic dissertation presented at University Hospital, University of Oulu, Finland. http://herkules.oulu.fi/isbn9514252217/html/x317.html

[Sait02] Saito, M., Fukaya, M., and Iwasaki, T. 2002. "Serpentine Locomotion with Robotic Snakes." *IEEE Control Systems*. Vol. 22, iss. 1, pp. 64-81.

[Sarv04] Sarvar, F. *et al.* 2004. "Thermo-mechanical modelling of polymer encapsulated electronics." *IEEE Intersociety Conference on Thermal Phenomena*. Las Vegas, NV, pp. 465-472.

[Schn55] Schneider, P.J. 1955. Conduction Heat Transfer. Addison-Wesley, Reading, MA.

[Spra06] Spranklin, B.W. 2006. "Design, Analysis, and Fabrication of a Snake-inspired Robot with a Rectilinear Gait." MS Thesis, University of Maryland.

[Taki01] Takita, Y., Hasegawa, M., and Nunobiki, M. 2001. "An investigation of climbing up stairs for an inchworm robot." *Advanced Robotics*. Vol. 15, iss. 2, pp. 245-253.

[Tane05] Tanev, I., Ray, T. and Buller, A. 2005. "Automated evolutionary design, robustness, and adaptation of sidewinding locomotion of a simulation snake-like robot." *IEEE Transactions on Robotic*. Vol. 21, iss. 4, pp. 632-645.

[Teh00a] Teh, N.J. *et al.* 2000. "Embedding of Electronics within Thermoplastic Polymers using Injection Moulding Technique." *Proceedings from the 26th IEMT Symposium*. Santa Clara, CA, pp. 10-18.

[Teh00b] Teh, N.J. *et al*. 2000. "Statistical Optimisation of Thermoplastic Injection Moulding Process for the Encapsulation of Electronic Subassembly." *Journal of Electronics Manufacturing*. Vol. 10, iss. 3, pp. 171-179.

[Thom02] Thomas, J. *et al.* 2006 "Multifunctional structure-plus-power concepts." *43rd AIAA/ASME/ASCE/AHS/ASC Structures, Structural Dynamics, and Materials Conference*, April 22-25, Denver, CO.

[Thom04] Thomas, J. and Qidwai, M. 2004. "Mechanical design and performance of composite multifunctional materials." *Acta Materialia*. Vol. 52, pp. 2155-2164.

[Tito96] Titomanlio, G. and Jansen, K.M.B. "In-Mold Shrinkage and Stress Prediction in Injection Molding." *Polymer Engineering and Science*. Vol 38, iss. 15.

[Udd95] Udd, E. 1995. Fiber Optic Smart Structures, Wiley-Interscience, New York, NY 1995.

[Vale02] Valentín, A. 2002. "An Application of Classical Continuum Theory to Image Analysis." MS Thesis, University of South Carolina.

[Weis97] Weiss, L.E. *et al.* 1997. "Shape Deposition Manufacturing of Heterogeneous Structures." *Journal of Manufacturing Systems*. Vol. 16, iss. 4, pp. 239-248.

[Wors96] Worst, R. and Linnemann, R. 1996. "Construction and Operation of a Snake-like Robot." *IEEE International Joint Symposia on Intelligence and Systems*. Nov. 4-5, Rockville, MD.